INFORMATION TO USERS

This manuscript has been reproduced from the microfilm master. UMI films the text directly from the original or copy submitted. Thus, some thesis and dissertation copies are in typewriter face, while others may be from any type of computer printer.

The quality of this reproduction is dependent upon the quality of the copy submitted. Broken or indistinct print, colored or poor quality illustrations and photographs, print bleedthrough, substandard margins, and improper alignment can adversely affect reproduction.

In the unlikely event that the author did not send UMI a complete manuscript and there are missing pages, these will be noted. Also, if unauthorized copyright material had to be removed, a note will indicate the deletion.

Oversize materials (e.g., maps, drawings, charts) are reproduced by sectioning the original, beginning at the upper left-hand corner and continuing from left to right in equal sections with small overlaps. Each original is also photographed in one exposure and is included in reduced form at the back of the book.

Photographs included in the original manuscript have been reproduced xerographically in this copy. Higher quality 6" x 9" black and white photographic prints are available for any photographs or illustrations appearing in this copy for an additional charge. Contact UMI directly to order.

UMI®

Bell & Howell Information and Learning
300 North Zeeb Road, Ann Arbor, MI 48106-1346 USA
800-521-0600

Particle Motion in a Brinkman Medium with Applications to Biological Transport

Jianjun Feng

A dissertation submitted to the Faculty in Engineering in partial fulfillment of the requirements for the degree of Doctor of Philosophy, The City University of New York

1999

This manuscript has been read and accepted for the Graduate Faculty in Engineering in satisfaction of the dissertation requirement for the degree of Doctor of Philosophy.

9/30/99

Date

Sheldon Weinbaum

Professor Sheldon Weinbaum

Chair of Examining Committee

9/30/99

Date

Mumtaz K. Kassir GGL

Professor Mumtaz K. Kassir

Executive Officer

Professor Andreas Acrivos

Professor Stephen C. Cowin

Professor Peter Ganatos

Professor Gerard A. Ateshian

Supervisory Committee

The City University of New York

Abstract

PARTICLE MOTION IN A BRINKMAN MEDIUM WITH APPLICATION TO BIOLOGICAL TRANSPORT

Jianjun Feng

Mentor: Professor Sheldon Weinbaum, Co-mentor: Professor Peter Ganatos

A thin polyelectrolyte layer of loose fibers which coats the surface of endothelial cells, known as a surface glycocalyx, appears to be ubiquitous throughout the vascular system. This fiber matrix, which is composed of various proteins and other extracellular components, forms a highly compressible structure, that performs at least two vital functions at the cellular level. This fiber matrix layer both determines the Starling (oncotic) forces that act across vascular the endothelium and modulates the interaction of red and white cells with the endothelial surface. In this research we attempt to provide a framework for understanding the hydrodynamics of this fiber layer and the motion of solutes in a fiber matrix more generally. We shall develop methods and models for analyzing a range of problems arising in molecular mechanics, transport through capillaries and blood rheology. The general approach is based on effective medium theory (Brinkman equation) as applied to porous materials.

Analytic and numerical solutions to the Brinkman equation which describe the fluid or particle motion in a fiber-filled medium exhibit some unusual hydrodynamic features that are absent for a pure fluid medium. We first show by examining the arbitrary translation and rotation of a disk that the resistance and the torque on the disk depend significantly on the particle orientation. We then consider the inverse problem of flow through an orifice or pore in a Brinkman medium as a model for the flow through fenestrated pores in capillary endothelium. This problem is of fundamental fluid mechanical interest because it bridges the transition from a slow viscous flow characterized by Sampson's classic solution to the Stokes equation to a Darcy flow which is described by a potential equation for the pressure as

the Darcy permeability decreases. The effect of confining boundaries on particle motion in a Brinkman medium is then examined for the first time. Here we examine the shielding effect of the fibers on the boundary interaction near a planar boundary when the clearance between the particle and the boundary decreases to distances of the order of the fiber spacing. The theory is applied to the motion of tagged lipid molecules in membrane bilayers in single particle tracking experiments and the penetration of leukocyte microvilli in the endothelial glycocalyx. Finally, a new type of lubrication theory is developed for highly compressible porous media which shows that there is an unexpected striking similarity between the gliding motion of a red cell moving over the endothelial glycocalyx that lines our microvessels and a human skier or snow boarder skiing on fresh powder. In both cases one finds that the pressure and lift force generated within the compressed matrix are four orders of magnitude greater than heretofore realized. These huge repulsive forces may explain why red cells do not experience constant molecular interactions with the endothelial plasmalemma.

Acknowledgements

I would like to express my sincere gratitude to my advisors, Professor Sheldon Weinbaum and Professor Peter Ganatos for their continuous support, suggestion and encouragement in addition to their incisive, scientific insight throughout this work.

I especially thank Professor Weinbaum during my studies at the Center for Biomedical Engineering, for his time, patience and tolerance in addition to his physical and biological insight and guidance. In short, Professor Weinbaum enhanced the value and experience of my graduate research immeasurably, and for this I thank him.

I am indebted to a large number of people for their assistance in the preparation of this dissertation. I am especially grateful to my wife Ying Xu, now in Procter & Gamble Company, for always loving me and sharing my joys and pains throughout the course of this work. Although we have been living in separate cities for five years, we have kept in remarkably close contact throughout the time. I have to mention my parents in China for supporting me unconditionally, my colleagues in the Department of Mechanical Engineering and the Center for Biomedical Engineering for providing me a good environment which allows me to do research efficiently. Without this love and encouragement the present work would be impossible.

Financial support from the National Institutes of Health is also gratefully acknowledged.

I dedicate this research to my wife Ying and my parents.

Contents

List of Tables

List of Figures

Chapter 1 Introduction

1.1 Biological Background

Particle motion in a fibrous medium is encountered in a wide variety of chemical and biomedical engineering applications, most notably in transport phenomena through fixed fiber beds (Spielman & Goren 1968; Howells 1974, 1998), transendothelial transport of solutes across the endothelial surface glycocalyx and the entrance region of the interendothelial cleft (Fu *et al.* 1994), the transport of low density lipoproteins (LDL) in the arterial intima and the growth of cellular level subendothelial leakage spots (Yuan *et al.* 1991; Huang *et al.* 1994), the penetration of the endothelial surface glycocalyx by microvilli on rolling leukocytes (Bruehl *et al.* 1996; Alon *et al.* 1997; Schmidt *et al.* 1997), the motion of red cells in tightly fitting capillary and the effect of matrix compression on the rheological properties of blood flow (Vink & Duling 1996; Damiano 1998; Secomb *et al.* 1998), and single particle tracking experiments where either 40nm gold or 210nm latex particles are attached to lipid molecules and membrane proteins and observed in nanovid (video enhanced) microscopy (Zhang *et al.* 1991; Lee *et al.* 1993; Sako & Kusumi 1994, 1995, 1998) to mention only a few of the studies in this rapid expanding research area. This research will explore the hydrodynamic interactions in these problems using an effective medium approach. Special emphasis will be placed on the hydrodynamic interaction between the particle moving through the surface glycocalyx and the adjacent boundary or boundaries. Figure 1.1 shows the surface glycocalyx coating the interior surface of a capillary in which the functional diameter of the capillary is significantly reduced by this surface matrix. I shall first provide a brief biological background for this research.

1.1.1 Diffusion of Lipid Molecules in Membranes by Single Particle Tracking Techniques

Recent developments in single particle tracking by nanovid microscopy and optical tweezers techniques have made it possible to study quantitatively the lateral diffusion of a variety of lipid molecules and transmembrane proteins in the plasmalemma membranes of many cell types (Lee *et al.* 1993; Sako *et al.* 1994, 1995, 1998). By tagging transmembrane receptor proteins with 40nm colloidal gold particles or latex particles of 210nm diameter, Sako *et al.* (1994, 1995) found that the plasma membrane of cultured rat kidney fibroblastic cells, is compartmentalized into discrete regions by the underlying F-actin cytoskeleton. The long-term diffusion of the tagged receptor molecules is the result of successive inter-compartment jumps. This diffusion is one or two order of magnitude lower than the Brownian diffusion of the proteins within a given compartment.

The interpretation of the movements of the gold-tagged receptor proteins is complicated, not only because of the complex structure of the cytoskeleton itself, but also due to the associated matrix layer on the exterior surface of the plasma membrane. This pericellular matrix, also known as the surface glycocalyx, is composed of ectodomains of integral membrane glycoproteins, proteoglycans, glycolipids, hyaluronan and a variety of extracellular matrix (ECM) glycoproteins. The gold or latex particle in combination with its transmembrane receptor or lipid molecule combination must move through this surface glycocalyx and, therefore, the interaction between the gold or latex particle and this layer will contribute to both the short and long-term diffusivity.

Lee *et al.* (1993) measured the average diffusivity of a variety of colloidal gold-tagged lipid molecules using a nanovid microscopy technique. These lipid molecules differ from the transmembrane receptor proteins in that they do not have cytoplasmic tails that interact with the F-actin cytoskeleton. They found that the average diffusion coefficients range from 1.1 to $1.7 \times 10^{-9}\text{cm}^2/\text{sec}$, which are fivefold lower than the average diffusion coefficients (5.4 to $9.5 \times 10^{-9}\text{cm}^2/\text{sec}$) obtained by fluorescence recovery after photobleaching (FRAP), a

technique which removes the extracellular matrix but has little influence on the cytoplasmic membrane. The increase in drag exerted on the gold-tagged lipid molecule can be partly accounted for by the additional resistance of the gold particle moving through the matrix. However, as will be illustrated later in chapter 4 using a model based on the effective medium theory, only about 30 percent of the additional resistance comes from the hydrodynamic interaction, implying that an even larger contribution arises from the elastic and binding energy associated with the surface glycocalyx. Therefore, a realistic model should also take these effects into consideration.

Sako *et al.* (1995, 1998) conducted related experiments using a single particle tracking technique that combines optical gradient traps with nanovid microscopy. Both 40nm colloidal gold and 210nm latex particles are first attached to the transferrin-receptor (TR). By dragging the particle-TR complexes laterally along the plasma membrane using laser-tweezers and measuring the forces required to keep the complexes in the trap, they were able to differentiate and characterize two different mechanisms, namely corralling within an F-actin compartment and tethering by the membrane skeleton. Reported diffusion coefficients for a 40nm gold-tagged molecule within a compartment are similar to those measured in Lee *et al.*. Surprisingly, the diffusion coefficient for a 210nm latex-tagged molecule is about 50 percent less than the 40nm gold-tagged molecule.

These recent experiments have greatly expanded our knowledge of the structures on both sides of the plasma membrane. Earlier theoretical studies initiated by Saffman and other investigators (Saffman 1975; Saffman & Delbruck 1976; Hughes *et al.* 1981; Evans & Sackmann 1988; Bussel *et al.* 1992, 1994; Stone & Ajdari 1998) have focused attention on the hydrodynamics of a single or multiple mobile lipid particle inside the membrane embedded in a less viscous aqueous fluid of either infinite or finite depth. Other investigators have numerically modeled short and long-term diffusion coefficients using Monte-Carlo methods to account for the corralling mechanism of the membrane cytoskeleton. The study by Lee *et al.* (1993) is the only one to examine the effect of the extracellular matrix on membrane particle diffusion. This problem will be modeled by the motion of a sphere in a Brinkman

medium near a planar surface.

1.1.2 Motion of a Microvilli-Covered Leukocyte Near a Membrane

The rolling of a leukocyte in venular capillaries has attracted considerable attention in the past decade. The adhesive interaction between the leukocytes and the endothelial lining of blood vessels is a critical physiological response in tissue injury and inflammation. Recent experiments have revealed that this process is mediated by cell surface adhesion molecules called selectins. The rolling motion of individual cells has been observed to fluctuate randomly both *in vivo* and *in vitro*. The micro-mechanics of rolling is modulated by receptor-ligand bonds which are clustered at the tips of microvilli covering the leukocyte surface (Bruehl *et al.* 1996). The solution for the Stokes resistance tensor of a rigid sphere in shear flow in the presence of a planar wall is utilized to calculate the force and moment exerted on the cell (Dembo *et al.* 1988; Tozeren & Ley 1992).

There has been no prior study of the effect of the glycocalyx layer in these rolling leukocyte interactions. The surface glycocalyx is important in regulating the penetration of the endothelial glycocalyx by the protruding microvilli and the swivel motion of the leukocyte once the tethering interaction is initiated. The surface matrix modifies the hydrodynamic functions which describes the motion of the cell body in proximity to the substratum. Figure 1.2 sketches a simple model in which a spherical cell of 4μm radius decorated with a rigid spike (model for microvillus) undergoes a tethering swing in an ambient shear flow. The effect of the surface glycocalyx is twofold. First, it changes the velocity profile at the interface between the fluid and ECM. A rough estimate using a fiber-filled medium model indicates that the hydraulic permeability of this layer is quite small. Within the glycocalyx, the velocity is almost uniform except for a thin transition region near the interface, leading to a so called Beaver-Joseph slip boundary condition at the interface. This has not previously been considered in calculating the hydrodynamic force and moment (Tozeren 1984). Secondly, the interaction between the microvilli and the fiber matrix plays an important role

in the tethering process. Figure 1.2b sketches typical dimensions of the parameters from which one can estimate roughly the magnitude of the forces exerted on the cell body and on the microvilli. Using a cylinder with a hemisphere at one end to represent the microvilli and adding the drag exerted by the external medium separately, one can calculate the total drag on the microvilli. One finds that this is of the same order of magnitude as the drag on the cell body, since the drag correction factor due to the fibrous medium is large compared to the external fluid and this balances the much larger relative size of the cell body. Of special interest is the penetration velocity of the microvillus since this velocity together with the rolling speed determines whether the microvillus will penetrate sufficiently for a tethering interaction to be initiated.

1.1.3 Transendothelial Transport of Solute Molecules

Recent ultrastructural experiments have revealed that the principal transendothelial pathway where water and small solute molecules cross the endothelial layer are the breaks in the junction strands in the interendothelial cleft. The entrance layer of this cleft is filled with a matrix that is a continuation of the surface glycocalyx shown in Fig. 1.1 and 1.2. This fibrous medium, together with other mechanisms, regulates the hydraulic conductivity and diffusive permeability of capillary endothelium. A series of models has been proposed to elucidate some long-standing issues concerning the relative importance of these mechanisms. In particular, a simple multiplicative formula

$$D_{im} = D_{iw}\left[1 + \frac{r_s}{\sqrt{K_p}} + \frac{r_s^2}{9K_p}\right]^{-1} \tag{1.1.1}$$

is suggested to estimate the diffusion coefficient of a spherical molecule in a fiber-filled channel representing the cleft (Weinbaum *et al.* 1992), where D_{iw} is the average diffusion coefficient integrated across the channel height in the absence of fibers obtained from the solutions in Ganatos *et al.* (1980a), and the term in brackets describes the effect of the matrix in the absence of confining boundaries.

One can expect that due to the shielding effect of the fibers surrounding the particle, the confining boundary becomes less important as the hydraulic permeability of the fiber matrix increases and, thus, the expression for D_{iw} does not properly treat the wall effect. It is of interest to assess the accuracy of this formula by solving for the motion of a sphere in a fiber-filled channel. In chapter 4, this solution is obtained using effective medium theory. One concludes that equation (1.1.1) underestimates the diffusion coefficient by as much as 25 percent for $\alpha = 1.0$ when the height of the channel is twice the sphere diameter. Here α is defined by $r_s/\sqrt{K_p}$ in which r_s is the characteristic length of the particle (radius for a sphere or disk) and K_p is the Darcy permeability. Equation (1.1.1) is a good approximation only when $\alpha \ll 1$. More accurate diffusion coefficients for a spherical solute molecule in a channel are calculated as functions of solute size and channel height for a representative range of fiber spacing. Steric effects are also incorporated using a procedure proposed by Weinbaum *et al.* (1992) and Brady (1994).

1.1.4 Motion of Red Cells in Capillaries

The initial motivation for chapter 5 is the outgrowth of several fundamental questions raised in Weinbaum (1998) concerning the role of the endothelial glycocalyx in microvessels. Recent experiments reported in Vink & Duling (1996) have shown that the glycocalyx is a negatively charged polysaccharide rich layer that uniformly coats the luminal surface of microvascular endothelium. This layer has been estimated to vary from 0.1μm in *in vitro* studies of frog mesentery capillaries (Adamson *et al.* 1991), to 0.4μm in *in vivo* studies of hamster cremaster microvessels (Vink & Duling 1996). Hydrodynamically, this layer can be thought of as a hydrated gel, 99 percent of whose volume is water (Weinbaum 1998). This extracellular layer has recently been proposed to be the primary molecular filter or osmotic barrier that determines the Starling forces that act across microvessel endothelium (Michel 1997; Hu & Weinbaum 1999; Weinbaum 1998). To serve this function the barrier must exclude albumin (7nm in diameter) and, thus, the nominal fiber spacing of the undeformed matrix must be close to 7nm.

One of the long standing mysteries in the microcirculation is how the red cells are able to traverse the microvessels without undergoing constant molecular interaction with the plasmalemma membranes of the endothelial cells at the luminal surface. The highly deformable 8μm diameter red cells are easily able to squeeze through 5-6 μm true capillaries with a separation distance near the wall that is typically a few tenths of a micron (Vink & Duling). Furthermore, this separation distance appears to vanish when the motion of the red cells is arrested indicating that the matrix layer is highly deformable. In larger microvessels, where the red cells do not travel in single file and there is a shear induced migration of the red cells towards the vessel axis, a similar separation distance is also observed near the microvessel wall.

1.2 Motion of a Particle in Porous Media: Theoretical and Numerical Studies

Although there have been many experimental investigations on the effect of the surface glycocalyx in several biological systems, its structure and mechanical properties have not been characterized due to the limitations of the experimental techniques. For example, it is difficult to preserve the matrix with conventional fixation. The advantage of the effective medium approach is that this unknown fibrous structure can be characterized by only one additional parameter, the Darcy permeability K_p. Thus, a detailed knowledge of the fiber matrix is not required.

As will be discussed in detail later in chapters 2 through 4, various methods developed for Stokes flow can be extended to the Brinkman equation. Previous investigations which examine the theoretical basis for this heuristic equation indicate that the Brinkman model is a good approximation for the hydrodynamic interaction of particles and the embedding medium provided that the solid volume fraction is less than 5 percent, which is true for most biological problems of interest. Both theoretical and experimental studies (Durlofsky

& Brady 1987; Phillips *et al.* 1989, 1990; Brady 1994; Johnson *et al.* 1996, Kosar & Phillips 1995) indicate that the application of the Brinkman model may be limited more by an inadequate knowledge of the actual microstructure than by any inherent limitations in the effective medium approach when the fiber fraction is small.

While simulation methods successfully demonstrate the applicability and accuracy of the effective medium theory, a number of researchers have developed iterative solutions based on ensemble average and renormalization techniques in which the Stokes equation is solved for both fixed beds and free suspensions (Childress 1972; Tam 1969; Howells 1974, 1998). The most important conclusion drawn from these studies is that the Brinkman medium is a first order approximation in the dilute fiber limit and, thus, provides a rigorous mathematical basis for the effective medium approach. For bounded flows Tsay & Weinbaum (1991) have shown that the solution of the Stokes equations for flow through a doubly periodic array of cylindrical fiber posts in a parallel-walled channel is accurately described by the Brinkman approximation for fiber volume fractions that can far exceed the dilute limit.

Although a number of techniques have been developed for the particulate motions in Stokes flow, solutions for the Brinkman equation are much more limited partially because the presence of the Darcy resistance term does not permit this equation to be simply separable except for elementary coordinate systems. In chapter 4, the boundary integral equation method will be formulated using the Green's function (point force) for the Brinkman equation. A more extensive discussion of the applicability of this equation is also included in this chapter.

The dual purposes of the present research are:

i To develop new solutions to the Brinkman equation for non-spherical particles and formulate a general boundary integral equation technique for treating the motion of a particle in a bounded Brinkman medium, which can be solved numerically. Special attention is focused on flows in an axisymmetric domain in which the boundary integral equation is considerably simplified. An accurate and efficient numerical quadrature is

developed in order to treat the low-permeability situation.

ii To apply this effective medium theory to the several biological problems that have been outlined in this introduction.

In an effort to develop new solution procedures for the Brinkman equation, the motion of a circular disk in an unbounded Brinkman medium is first investigated in chapter 2 using a general solution presented in Kim & Russel (1985). The boundary value problem is decomposed into four elementary motions which are formulated by a set of dual integral equations. Asymptotic solutions are obtained for the limiting cases where the permeability of the medium is small or large, and numerical solutions obtained for the intermediate permeability. In an analogy to Stokes flow, the general motion can be studied by introducing the translation, rotation and coupling tensors obtained from four elementary motions, i.e., broadside and edgewise translation and in-plane and out-of-plane rotation. The results reveal strong dependence of the drag and torque on orientation of the disk in sharp contrast to Stokes flow in which the difference is small. The new solutions are used to test the more general numerical method developed in chapter 4. Since the motion of the disk depends only on the permeability of the medium, the calculated drag and torque corresponding to various orientations is a useful probe of the microstructure of porous media. These new solutions thus provide a way to test the validity of the effective medium approach.

The Brinkman equation is mathematically equivalent to the harmonic oscillation of a particle in an otherwise quiescent Stokes flow. Starting from the reciprocal theorem, a boundary integral equation is derived in chapter 4. Following a procedure similar to that of Pozridkidis (1992, 1994), the boundary integral equation is reduced to a set of one-dimensional Fredholm integral equations of the first kind defined on the contour of an axisymmetric domain. Further simplification is achieved if either the ambient flow or the velocity of the particle has a first order harmonic dependence on the azimuthal angle. In this case only the first term of the Fourier series decomposition needs to be retained. In particular, the double layer contribution can be evaluated analytically for translational

motion. Thus, the computational effort is dramatically reduced when the boundary integral equation is discretized and solved by collocation techniques.

The proposed boundary integral equation method is first tested by comparing the calculated results with available solutions or with solutions obtained using the multipole collocation method. It has been shown that the agreement is excellent and the method is both accurate and efficient for all values of the dimensionless permeability parameter α. The simplest bounded motion is a spherical particle moving in proximity to a planar boundary. This problem is an idealized model for the penetration of a microvilli into the surface glycocalyx in figure 1.2 and a model for lateral diffusion of a gold-tagged lipid molecule in a membrane. The conclusion drawn from these computations is that the hydrodynamic interaction can not adequately account for the hindered diffusion, suggesting that the elastic and binding energy of the matrix fibers is of comparable importance.

The motion of a spherical particle in a fiber filled channel is studied with application to transendothelial transport of solute molecules in the interendothelial cleft. The drag and torque are calculated for representative cleft geometries and matrix permeability. The diffusion coefficient is obtained using the Stokes-Einstein relation. Comparison with previous results, which are based on the simple multiplicative formula (1.1.1) combining the unbounded Brinkman result and a channel contribution for the Stokes flow, indicates that the interaction of the particle with the fibers and the channel walls leads to a larger diffusivity due to the shielding effect of the fibers surrounding the particle. The significant effect of the steric exclusion is also taken into account in the present model. The maximum value of α for which the particle is not trapped by the fibers for typical values of fiber spacing and diameter is of $O(1)$, indicating that the wall effect is of significance. In general, the effect of the confining boundaries diminishes as α increases. A local analysis of the Brinkman equation when the sphere is close to the boundary is also conducted using stretched variables. In the limit when the gap height is smaller than the fiber spacing solutions for Stokes like lubrication theory are obtained.

In general, the effect of the surface glycocalyx can be both microscopic and macroscopic. Problems in the microscopic category are represented by the rolling of a leukocyte adjacent to the endothelial surface with emphasis on the penetration of the glycocalyx and adhesion of its microvilli. On the macroscopic length scale, the glycocalyx can alter fluid velocity, the mass transport rate and induce streaming currents and electric potentials because of electrical effects (Mokady *et al.* 1998).

Presently, studies on the microscopic length-scale are difficult to evaluate due to a lack of knowledge of the fine structures and physical properties of the glycocalyx and a paucity of available experimental results. The surface glycocalyx can also differ with the type of cell and may vary with species. For example, the measured thickness of the glycocalyx varies from 100nm (Adamson & Clough 1992) in frog mesentery capillaries to 400nm (Vink & Duling 1996) for mammalian capillaries. However, the effective medium approach, as described above, does not depend on the detailed structure of the fibrous medium and introduces only one additional parameter, K_p, which can be determined by either theoretical prediction or experimental measurement. Therefore, this approach is particularly useful in studying transport processes in a medium such as the endothelial glycocalyx whose structure is not clearly defined.

Recently, biphasic mixture theory has been applied to examine the effect of the endothelial-cell glycocalyx on the motion of red blood cells through capillaries. (Damiano *et al.* 1996; Damiano 1998; Secomb *et al.* 1998). In these studies, the red blood cell is modeled by either a solid spherical particle or a deformable thin shell enclosing incompressible cytoplasm. The gap between the cell surface and the capillary wall is so small that lubrication theory can be used to describe the fluid motion in this region. The surface glycocalyx is represented as interacting fluid and solid constituents which resist penetration by the red blood cells. Making use of the analytic solution of the Reynolds equation which governs the pressure in the lubrication layer and the shear stress distribution on the cell surface, one can determine the pressure profile, membrane tension and cell shape by numerically solving a reduced system of coupled, nonlinear, ordinary differential equations. The model in Damiano (1998)

predicts that the presence of a 0.5 μm thick glycocalyx in a 5 μm capillary leads to a threefold increase in resistance and a reduction in capillary hemotocrit of more than 30% compared with corresponding values in a smooth-walled glass tube. These predictions for the hydraulic resistance are still a factor of four lower than the *in vivo* viscosity law in Pries *et al.* (1994).

Although several new features have been revealed using biphasic theory, there are still some important issues that need to be clarified. First, the value of the resistivity used in this theory corresponds to a fiber spacing (60-180nm), which is an order of magnitude higher than that generally estimated by fiber-matrix theory ($\sim$ 7nm) (Fu *et al.* 1994), and the value of the Darcy resistivity three order of magnitude too low. The discrepancy indicates that either the surface glycocalyx is highly inhomogeneous or compressible, leading to large variations of the fiber structure. Second, the radial deformation of the glycocalyx is not considered. Experimental evidence shows that this layer can be compressed nearly entirely by either the highly deformable RBC or a more rigid WBC (Vink & Duling 1996). Although the bending resistance of the cell membrane is not taken into account in the present study, the general method for treating highly compressible porous layer is readily extended to deformable membranes with bending resistance using the approach in Secomb *et al.* (1986).

In chapter 5, a new type of lubrication theory is developed to describe flow in thin porous layers where there are order of magnitude variations in K_p due to large amplitude compressions. The model for K_p involves a local solution of the Stokes equations for the local flow through the compressed fiber array. The solutions to the generalized Reynolds equation for this new theory are able to explain the popout phenomenon in which the red cell first rises off the compressed glycocalyx as its velocity increases. In addition, there is an unexpected striking similarity between the gliding motion of a red cell moving over the endothelial glycocalyx that lines our microvessels and a human skier or snow boarder skiing on fresh powder. In both cases one finds that the pressure and lift force generated within the compressed matrix are four orders of magnitude greater than, heretofore, realized. These huge repulsive forces may explain why red cells do not experience constant molecular

interactions with the endothelial plasmalemma.

The thesis is organized as follows. Chapter 2 presents a new solution to the Brinkman for the general motion of a circular disk. The strong dependence of the flow properties on the particle orientation is discussed. A geometrically complementary model problem, namely pressure driven flow through a pore of either infinitesimal or finite length in a Brinkman medium, is presented in chapter 3 as a simplified model for estimating the hydraulic conductivity of fenestral pores in capillaries. In chapter 4, a general boundary integral equation method is proposed for the Brinkman equation in an axisymmetric domain. The results for the hydrodynamic resistance functions for a sphere moving either perpendicular or parallel to a planar surface are applied to the biological problems described earlier. This is followed by chapter 5 where a new type of lubrication theory is developed for a highly compressible Brinkman medium. Idealized models based on this theory are proposed to study the mechanics of skiing or snowboarding on fresh snow powder and the motion of a red cell in a microvessel lined with an endothelial glycocalyx. Finally, chapter 6 summarizes the important contributions of this dissertation.

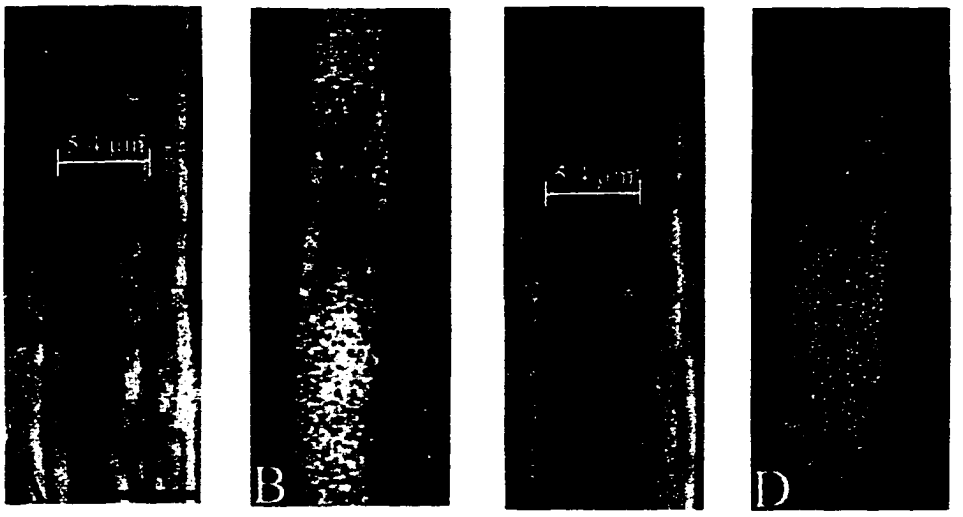

Figure 1.1: Digitized images of a capillary segment showing the significant surface glycocalyx. RBC width (A) and the width of the FITC-dextran column (B) are significantly smaller than the anatomic capillary diameter. Treatment of the capillary with epi-illumination increases the width of RBC (C) and FITC-dextran column (D), without a significant effect on the anatomic capillary diameter. (from Vink & Duling 1996)

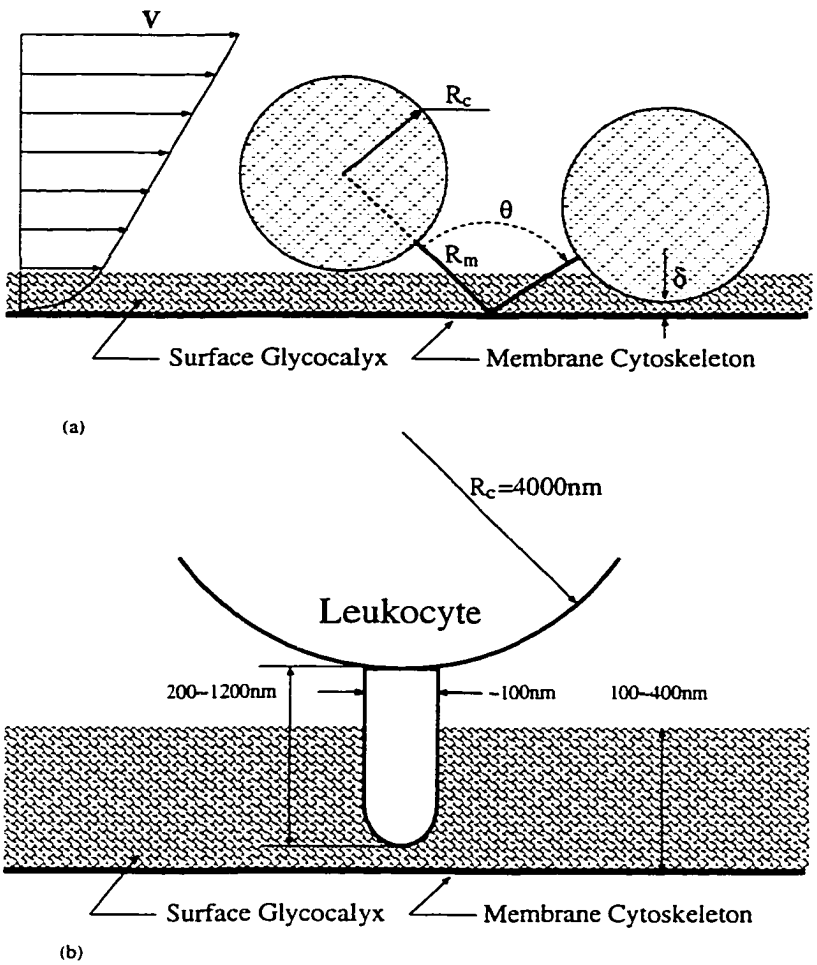

Figure 1.2: Schematic illustration of the rolling of a leukocyte tethered to a substratum coated by a surface glycocalyx (a). Also shown in (b) the penetration of a microvilli tip into the glycocalyx.

Chapter 2 The General Motion of a Circular Disk in a Brinkman Medium

2.1 Introduction

Particle motions in a fiber-filled medium are encountered in a wide variety of biological and chemical engineering applications (Tsay & Weinbaum 1991; Weinbaum *et al.* 1992; Fu *et al.* 1994; Huang *et al.* 1996). The Brinkman equation (Brinkman 1947) has often been used as a model for a fiber-filled medium. More recent analysis has shown that it is a good approximation in the low fiber fraction limit (Durlofsky & Brady 1987). This is usually true in biological applications where the fiber volume fraction is 5 percent or less. Since the Brinkman equation has only one additional parameter, K_p, which characterizes the permeability of the porous media, one does not have to have a knowledge of the detailed structure of the porous media once the permeability has been determined either by theoretical prediction or experimental measurement. In this paper, analytic solutions of the Brinkman equation will be obtained for disk-like particles oriented arbitrarily in an unbounded Brinkman medium. Four elementary flow problems, namely the broadside and edgewise translation, in-plane and out-of-plane rotation, as depicted in figure 2.1, will be analyzed separately.

The combination of viscous transport of momentum in the Stokes equation with the frictional drag governed by Darcy's law leads to the Brinkman equation. Numerous investigations have been performed since the initial work by Brinkman, who derived this equation heuristically and calculated the drag on a translating sphere. However, the known solutions for the Brinkman equation for flow geometries other than a single sphere are very limited. Due to the added resistance of the Darcy term in the Brinkman equation, the general representation of the solution for the velocity field involves scalar functions obtained by

solving the Helmholtz equation. These solutions are analogous to the harmonic functions for creeping flow. However, solutions involving either prolate or oblate spheroids moving in a Brinkman medium are not as simple as in steady creeping motion because the separation of the governing equation in the corresponding orthogonal coordinate system leads to complicated spheroidal wave functions. In contrast to Stokes flow, Lawrence and Weinbaum (Lawrence & Weinbaum 1988) have shown that the disk cannot be treated as a limiting case when the spheroidal wave functions have a vanishing aspect ratio. Furthermore, the Helmholtz equation is not simply separable in bispherical coordinates, which makes analytic approaches even more difficult for many applications of interest.

In contrast to Stokes flows, where the drag on a particle is the same whether the particle is moving in a stationary fluid at infinity or where there is a uniform flow past a stationary particle, in a Brinkman medium these two solutions are not interchangeable since for a uniform flow there is a finite pressure gradient at infinity described by the Darcy resistance. This pressure gradient gives rise to a term which is proportional to the volume of the particle. This phenomenon does not affect the solutions presented herein since the disk has a vanishing volume.

In the study of the microstructure of the porous materials, the difference between the translational and rotational motions can be useful in probing the structure of the medium. Suppose we have derived expressions for the drag F/F_s and torque T/T_s normalized by the corresponding Stokesian results for a specific particle, then by comparing the measured data for the same particle, one can test the validity of the Brinkman model on the length scale a since these two expressions depend only upon one parameter α.

Due to the linearity of the governing equations, the velocity and pressure fields corresponding to an arbitrary motion of a rigid particle in a Brinkman medium can be obtained by superposition of the solutions for three mutually orthogonal translations $\mathbf{U}_p$ and three

mutually orthogonal rotations $\mathbf{\Omega}_p$. The general velocity on the particle surface is

$$\mathbf{u}(\mathbf{x}_s) = \mathbf{U}_p + \mathbf{\Omega}_p \times \mathbf{x}_s \tag{2.1.1}$$

in which $\mathbf{x}_s \in S_p$ and S_p denotes the surface of the particle. For a circular disk, four basic motions are necessary to determine the arbitrary motion, as described in figure 2.1. In the following sections, solutions for these four basic motions are derived from a general solution of the Brinkman equation. Asymptotic solutions for both large and small values of the permeability parameter α are obtained. These results together with numerical results valid for intermediate α, indicate large differences in particle drag or torque depending upon particle orientation, in sharp contrast to the solution for Stokes flow where the drag varies only by a factor of 1.5 and the torque is isotropic. The growth of the drag on a disk translating broadside increases faster than on a sphere of the same radius as the solid fraction increases, whereas the effects of the porous material on a disk translating edgewise is of lower order in the dimensionless permeability parameter α than in broadside motion. For rotational motion, the torque growth is $O(\alpha^2)$ for out-of-plane rotation and $O(\alpha)$ for in-plane rotation, compared with $O(\alpha)$ for a rotating sphere. It is also shown that the effect of the porous medium on the torque for a rotating particle is weaker than on the drag for a translating particle when the medium is dilute.

Mathematically, the Brinkman equation is eqivalent to the unsteady Stokes equation describing harmonic oscillatory motion. Recently, Zhang and Stone (1998) studied the oscillation of a circular disk in an unbounded Stokes flow, in which the governing equations are solved using direct Hankel transforms, an approach which these authors had used previously for disk motions in steady Stokes flow (Tanzosh & Stone 1996). The dual integral equations obtained by these authors are similar to those presented in the present paper. In Zhang and Stone (1998), the dual integral equations are reduced to a linear system of algebraic equations. In the following sections, we will present an alternative way to derive these dual integrals using a general solution to the Brinkman equation, in which the boundary

conditions can be easily satisfied. We will also use a reduction method based on the Abel transform to solve these equations. The advantage of the present method is that both the asymptotic results valid for large and small values of the parameter α and numerical results for intermediate values of α can be obtained in the same framework. Moreover, the present method can be extended to investigate more complicated motions involving an annulus, a disk confined in a circular tube or in the presence of a planar wall.

2.2 Translation of a Circular Disk in a Brinkman Medium

The Brinkman equation,

$$\nabla p = \mu \nabla^2 \mathbf{v} - \frac{\mu}{K_p} \mathbf{v} \tag{2.2.1}$$

together with the continuity equation for an incompressible viscous fluid,

$$\nabla \cdot \mathbf{v} = 0. \tag{2.2.2}$$

are often used to describe flows in porous media in which the pressure gradient, velocity gradient and Darcy resistance are of comparable importance. As previously noted by Kim and Russel (1985), the velocity representation of the solution to equation (2.2.1) can be expressed using three scalar functions which satisfy a Laplace equation and two Helmholtz equations

$$\nabla^2 p = 0, \qquad (\nabla^2 - \frac{1}{K_p})\Phi = 0, \qquad (\nabla^2 - \frac{1}{K_p})\chi = 0. \tag{2.2.3}$$

The pressure field p, poloidal field Φ and toroidal field χ can be used to construct a general solution for the velocity field satisfying equations (2.2.1) and (2.2.2). This general solution can be expressed as (Stratton 1941)

$$\mathbf{v} = -\frac{K_p}{\mu} \nabla p + \nabla \times \nabla \times (\mathbf{x}\Phi) + \nabla \times (\mathbf{x}\chi). \tag{2.2.4}$$

Equation (2.2.4) can be succinctly derived as follows. Equations (2.2.1) and (2.2.2)

imply that $\nabla^2 p = 0$ and $\mathbf{v} = \nabla \times (\mathbf{A}_1 + \mathbf{A}_2)$, where $\nabla^2 \mathbf{A}_1 = 0$, $\nabla^2 \mathbf{A}_2 = K_p^{-1} \mathbf{A}_2$. Thus $\nabla p = -\mu/K_p \nabla \times \mathbf{A}_1$, i.e. $\mathbf{v} = -\mu/K_p \nabla p + \mathbf{v}_h$, where $\mathbf{v}_h$ is a homogeneous solution of (2.2.1). This general solution will be applied to specific motions of the disk in the subsections which follow.

2.2.1 Broadside Translation of a Disk in a Brinkman Medium

The solutions of equations (2.2.3) in spheroidal coordinates involve complicated spheroidal wave functions that are the same as the general solutions presented in Lawrence and Weinbaum (1988) for the axisymmetric oscillatory motion of a spheroid in Stokes flow since the two problems are mathematically equivalent. However, due to the singularities on the edge of the disk, these general solutions preclude the disk. Here we apply a dual integral equation method widely used in creeping flow problems to obtain the drag on a disk translating broadside in a Brinkman medium. Cylindrical coordinates (ρ, ϕ, z) are chosen so that the disk is instantaneously at $z = 0\,(0 \leq \rho \leq a)$ and moving along the z direction. The disturbed flow is axisymmetric and if we introduce the stream function ψ in spherical coordinates (r, θ, ϕ),

$$\mathbf{v} = \nabla \times \left[-\frac{\psi}{r \sin\theta} \mathbf{e}_\phi \right], \tag{2.2.5}$$

and normalize all lengths by the radius of the disk a, the governing equations (2.2.1) and (2.2.2) reduce to

$$L_{-1}(L_{-1} - \alpha^2)\psi = 0, \tag{2.2.6}$$

where $\alpha = a/\sqrt{K_p}$. The Stokesian operator L_{-1} is defined by

$$L_{-1} = \frac{\partial^2}{\partial \rho^2} - \frac{1}{\rho}\frac{\partial}{\partial \rho} + \frac{\partial^2}{\partial z^2}, \tag{2.2.7}$$

and the corresponding pressure field is obtained from the solution of

$$\frac{\partial p}{\partial z} = \frac{1}{\rho}\frac{\partial}{\partial \rho}[L_{-1} - \alpha^2]\psi \tag{2.2.8}$$

and

$$\frac{\partial p}{\partial \rho} = -\frac{1}{\rho}\frac{\partial}{\partial z}[L_{-1} - \alpha^2]\psi. \tag{2.2.9}$$

The general solution for the stream function ψ can be expressed as

$$\psi = \psi_1 + \psi_2, \tag{2.2.10}$$

where ψ_1 and ψ_2 satisfy,

$$L_{-1}\psi_1 = 0 \qquad (L_{-1} - \alpha^2)\psi_2 = 0. \tag{2.2.11}$$

These equations permit solutions by separation of variables and are given by

$$\psi_1 = \int_0^\infty \rho J_1(k\rho)A(k)e^{-k|z|}dk \tag{2.2.12}$$

$$\psi_2 = \int_0^\infty \rho J_1(k\rho)B(k)e^{-\sqrt{k^2+\alpha^2}|z|}dk. \tag{2.2.13}$$

Velocity conditions on the disk and pressure continuity on the fluid interface $z = 0,\ \rho > 1$ lead to the following set of dual integral equations

$$\int_0^\infty kJ_0(k\rho)A(k)\left[1 - \frac{k}{\sqrt{k^2+\alpha^2}}\right]dk = 1, \qquad (0 \le \rho \le 1), \tag{2.2.14}$$

$$\int_0^\infty J_0(k\rho)A(k)dk = 0, \qquad (\rho \ge 1), \tag{2.2.15}$$

where

$$B(k) = -\frac{k}{\sqrt{k^2+\alpha^2}}A(k). \tag{2.2.16}$$

Once we find $A(k)$, the drag on the disk is given by the total pressure difference across the disk

$$D = 2\pi\mu U_0 \int_0^1 \rho[p]_{0^-}^{0^+}d\rho$$

$$= 4\pi\alpha^2\mu U_0 \int_0^1 \rho d\rho \int_0^\infty J_0(k\rho)A(k)dk. \tag{2.2.17}$$

In the Stokes limit, where $\alpha \to 0$, the term in brackets in (2.2.14) reduces to

$$1 - \frac{k}{\sqrt{k^2+\alpha^2}} \to \frac{\alpha^2}{2k^2}, \tag{2.2.18}$$

and the dual integral equations (2.2.14) and (2.2.15) become,

$$\int_0^\infty k^{-1}J_0(k\rho)A(k)dk = \tfrac{2}{\alpha^2}, \qquad (0 \le \rho \le 1), \tag{2.2.19}$$

$$\int_0^\infty J_0(k\rho)A(k)dk = 0, \qquad (\rho \ge 1). \tag{2.2.20}$$

Tranter (1951) gives the solution of these dual integral equations as

$$A(k) = \frac{4}{\pi\alpha^2}\sin k. \tag{2.2.21}$$

The drag calculated by equation (2.2.17) is

$$D = 16\mu U_0 \int_0^1 \rho d\rho \int_0^\infty \sin k J_0(k\rho)dk = 16\mu U_0, \tag{2.2.22}$$

which is a well known result for Stokes flow.

In order to obtain $A(k)$ efficiently for other α, we can reduce the dual integral equations (2.2.14) and (2.2.15) to a integral equation of the second kind. Suppose

$$A(k) = k\int_0^1 h(t)\cos(tk)dt. \tag{2.2.23}$$

Then (2.2.15) will be satisfied automatically. Rewrite (2.2.14) as

$$\int_0^\infty k^{-1}J_0(\rho)A(k)(1-f(k))dk = \frac{2}{\alpha^2}, \qquad (0 < \rho < 1), \tag{2.2.24}$$

in which

$$f(k) = 1 - \frac{2k^2}{\sqrt{k^2+\alpha^2}(\sqrt{k^2+\alpha^2}+k)}. \tag{2.2.25}$$

Substituting (2.2.23) in (2.2.24), one notes that $h(t)$ satisfies the integral equation of the second kind,

$$h(t) = \frac{4}{\pi\alpha^2} + \int_0^1 h(u)K(t,u)du, \tag{2.2.26}$$

in which

$$K(x,u) = \frac{2}{\pi}\int_0^\infty f(v)\cos(xv)\cos(uv)dv. \tag{2.2.27}$$

The drag on the disk can be evaluated by substituting (2.2.23) into (2.2.17). This leads to

$$D = 4\pi\alpha^2\mu U_0 \int_0^1 h(t)dt. \tag{2.2.28}$$

When $\alpha << 1$, the kernel function $K(x,u)$ can be evaluated analytically by expanding the integrand in a Taylor series with respect to α. This leads to

$$K(x,u) = \frac{8}{3\pi}\alpha + o(\alpha^2). \tag{2.2.29}$$

In this case, equation (2.2.26) has a regular perturbation solution for $h(t)$ given by

$$h(t) = \frac{4}{\pi\alpha^2}\left(1 + \frac{8}{3\pi}\alpha + O(\alpha^2)\right). \tag{2.2.30}$$

Substituting $h(t)$ into (2.2.28), we obtain the drag

$$D = 16\mu U_0(1 + \frac{8\alpha}{3\pi} + O(\alpha^2)). \tag{2.2.31}$$

As $\alpha \to \infty$, $K(x,u) \to \delta(x-u)$ and therefore the present method breaks down. However, as $\alpha \to \infty$, the dual integral equations (2.2.14) and (2.2.15) become,

$$\int_0^\infty kJ_0(k\rho)A(k)dk = 1, \qquad (0 \le \rho < 1), \tag{2.2.32}$$

$$\int_0^\infty J_0(k\rho)A(k)dk = 0, \qquad (\rho > 1), \tag{2.2.33}$$

whose solution for $A(k)$ is given by

$$A(k) = \frac{2}{\pi}\left(\frac{\sin k - k\cos k}{k^2}\right). \tag{2.2.34}$$

The evaluation of (2.2.17), using (2.2.34), leads to

$$D = \frac{8\alpha^2}{3}\mu U_0. \tag{2.2.35}$$

For intermediate values of α, equation (2.2.28) must be evaluated numerically after numerically solving (2.2.26) for $h(t)$.

2.2.2 Edgewise Translation of a Disk in a Brinkman Medium

The boundary conditions on the disk for edgewise motion are

$$v_x = U_0, \quad v_y = v_z = 0 \quad \text{at } z = 0, \quad (0 \le \rho < 1). \tag{2.2.36}$$

Following the procedure proposed by Davis (1991, 1993) for Stokes flow, we introduce two scalar functions ψ and χ and write the solution of equation (2.2.1) in cylindrical coordinates (ρ, θ, z) as

$$\mathbf{v} = \nabla \times \nabla \times \left(\frac{\psi}{\rho}\cos\theta \mathbf{e_z}\right) + \nabla \times \left(\frac{\chi}{\rho}\sin\theta \mathbf{e_z}\right). \tag{2.2.37}$$

Here ψ satisfies the same equation as (2.2.6) and χ is governed by

$$(L_{-1} - \alpha^2)\chi = 0. \tag{2.2.38}$$

The pressure and Cartisian components of velocity are given by

$$p = \mu\frac{\cos\theta}{\rho}\frac{\partial}{\partial z}L_{-1}\psi, \tag{2.2.39}$$

$$v_x = \frac{1}{2}\rho\frac{\partial}{\partial\rho}\left[\frac{1}{\rho^2}\left(\frac{\partial\psi}{\partial z} - \chi\right)\right]\cos 2\theta + \frac{1}{2\rho}\frac{\partial}{\partial\rho}\left(\frac{\partial\psi}{\partial z} + \chi\right), \tag{2.2.40}$$

$$v_y = \frac{1}{2}\rho\frac{\partial}{\partial\rho}\left[\frac{1}{\rho^2}\left(\frac{\partial\psi}{\partial z} - \chi\right)\right]\sin 2\theta, \tag{2.2.41}$$

$$v_z = -\frac{\partial}{\partial\rho}\frac{1}{\rho}\frac{\partial\psi}{\partial\rho}\cos\theta. \tag{2.2.42}$$

Davis (1993) presents solutions to a problem mathematically equivalent to (2.2.36)-(2.2.42), i.e. edgewise oscillation of a disk in its own plane in creeping flow. He introduces the auxiliary functions $S(s)$ and $Y(s)$ and the unknown constant Γ which satisfy

$$[S(s) + Y(s)] - \tfrac{2}{\pi}\textstyle\int_0^1 [S(u) + Y(u)K_1(s,u)du = \tfrac{1}{2}(1-\Gamma), \tag{2.2.43}$$

$$[S(s) - Y(s)] - \tfrac{2}{\pi}\textstyle\int_0^1 [S(u) - Y(u)K_2(s,u)du = (1+\Gamma), \tag{2.2.44}$$

$$\textstyle\int_0^1 Y(u)du = 0, \tag{2.2.45}$$

where the kernels are given by

$$K_1(s,u) = \alpha^2\int_0^\infty \frac{\cos(ks)\cos(ku)}{\sqrt{k^2+\alpha^2}[\sqrt{k^2+\alpha^2}+k]}dk, \tag{2.2.46}$$

$$K_2(s,u) = \alpha^2\int_0^\infty \frac{\cos(ks)\cos(ku)}{[\sqrt{k^2+\alpha^2}+k]^2}dk. \tag{2.2.47}$$

Once these auxiliary functions are obtained, the drag on the disk is given by

$$\begin{aligned} D &= -\mu\int_{-\pi}^{\pi}\int_0^1 \left[\frac{\partial v_x}{\partial z}\right]_{0-}^{0+}\rho d\rho d\theta \\ &= 16\mu U_0\int_0^1 S(u)du. \end{aligned} \tag{2.2.48}$$

In the limit $\alpha \to 0$, the kernel functions $K_1(s,u)$ and $K_2(s,u)$ can be evaluated asymptotically as

$$K_1(x,u) = \alpha + O(\alpha^2), \tag{2.2.49}$$

$$K_2(x,u) = \frac{2}{3}\alpha + O(\alpha^2). \tag{2.2.50}$$

The integral equations (2.2.43)-(2.2.45) have a regular perturbation solution for $S(s)$, $Y(s)$ and Γ. Evaluation of (2.2.48) in the limit $\alpha \to 0$ leads to the following asymptotic solution for the drag,

$$D = \frac{32}{3}\mu U_0(1 + \frac{16}{9\pi}\alpha + O(\alpha^2)). \tag{2.2.51}$$

An asymptotic solution for large α cannot be obtained directly from the integral equations (2.2.43)-(2.2.45) because the kernels approach Dirac-delta functions. However, from a physical viewpoint, as shown in Tsay and Weinbaum (1991), the fiber boundary layer thickness around the disk is of $O(\alpha^{-1})$ for large α; therefore, the shear stress exerted on the disk is essentially identical to a disk of infinite extent. One integrates the shear stress for a simple one dimensional translation of an infinite plate in its own plane in a Brinkman medium. This leads to the following expression for the drag,

$$D \to 2\pi\mu U_0\alpha \qquad \text{as} \quad \alpha \to \infty. \tag{2.2.52}$$

For intermediate values of α one must solve (2.2.43)-(2.2.45) numerically for $S(s)$ and then determine the drag from equation (2.2.48). While one can mathematically determine a solution for all values of α for both broadside and edgewise motion, there are physical constraints on the maximum value of α that is compatible with the fiber spacing and the disk diameter. For the uniform flow past a stationary disk, this constraint is not present since the disk does not have to move between the fibers. Mathematically, in contrast to Brinkman's solution for a sphere, there is no difference in the solution for the uniform flow past a stationary disk and the translation of a disk in a quiescent medium since this difference vanishes for a particle with zero volume.

2.2.3 Results for the Drag on a Disk Translating in a Brinkman Medium

Consider first the disk translating broadside in an unbounded Brinkman medium. The integral equation (2.2.26) is solved numerically in order to determine the unknown function

$h(u)$. An ordinary Gauss-Chebyshev quadrature scheme is employed to discretize (2.2.26). The kernel function $K(x,u)$ is calculated by an adaptive Romberg quadrature with a maximum error tolerance of 10^{-8}. Once the function $h(u)$ is determined numerically, the drag exerted on the disk is evaluated from (2.2.28) using a Gauss-Chebyshev quadrature scheme.

The variation of the drag with respect to the dimensionless permeability parameter α is presented in figure 2.2, in which all values are normalized by the drag $16\mu U_0$ for a disk translating broadside in Stokes flow. The agreement between the numerical solution and the asymptotic results for small or large values of α confirms the rapid convergence of our numerical scheme outlined above. The same method is applied to solve the system of integral equations (2.2.43)-(2.2.45) for the unknown auxiliary functions $S(s)$ and $Y(s)$. The drag on a disk translating edgewise is calculated in a similar manner to that for broadside motion. This solution is plotted in figure 2.3 together with the asymptotic solutions (2.2.51) and (2.2.52) for small and large α, respectively. These results are normalized now by $32/3\mu U_0$, the drag on a disk of unit radius translating edgewise in Stokes flow. One notes that the asymptotic solution (2.2.51) for $\alpha << 1$ provides a remarkably good approximation for $\alpha < 10$.

In figure 2.4 the new solutions for the disk are compared with Brinkman's solution for the sphere. All results are normalized with respect to the Stokes drag on a sphere of unit radius $6\pi\mu U_0$. These results show some interesting new characteristics of the behavior of particles translating in an unbounded Brinkman medium. First, the drag on a disk translating broadside grows as $O(\alpha^2)$ as the permeability parameter α increases, whereas the drag on a disk translating edgewise grows as $O(\alpha)$. This is in sharp contrast to the drag on a disk in these two orientations for creeping flow, where the drag in broadside motion is just 1.5 times that for edgewise motion. Furthermore, in contrast to Stokes flow, we found that for sufficiently large values of α, the drag on a disk translating broadside can even exceed the drag on the sphere in a Brinkman medium. This crossover occurs at $\alpha = 6.246$.

The normalized drag on a sphere translating in a Brinkman medium is given by

$$D = 1 + \alpha + \frac{1}{9}\alpha^2, \tag{2.2.53}$$

which asymptotically approaches $\alpha^2/9$ for large α, whereas the normalized drag for a disk translating edgewise is $\alpha^2/6$ for large α. However, not all values of α are physically possible. For large α, which corresponds to small permeability or high solid fraction, the gap between two adjacent fibers may be too small and the disk will be trapped by the fibers. An approximate estimation of this critical value of α for a periodic fiber array can be derived using an empirical formula from the numerical results of Sangani and Acrivos (1982). In contrast to a translating particle in a quiescent medium, uniform pressure driven flow past a stationary particle can occur for all values of α. The uniform pressure driven flow contributes an additional drag on the particle which is proportional to its volume. It can be shown that this contribution is of the form of VU_0/K_p, where V is the volume of the particle in the medium. Thus, the drag on a stationary disk in any orientation in a uniform flow is identical to the drag experienced by the same disk undergoing translation. For the sphere in uniform flow, this additional drag is $\frac{4}{3}\pi a^3 \mu U_0$ and the net force normalized by the value for Stokes flow is

$$D = 1 + \alpha + \frac{1}{3}\alpha^2. \tag{2.2.54}$$

The strong dependence of the drag on the orientation of the particle can be interpreted both physically and mathematically. As shown in the previous subsection, expression (2.2.28) for the drag on a disk translating broadside is proportional to α^2 as $\alpha \to \infty$. This arises from the asymptotic behavior of the kernel function $K(x,u)$ for large α. The drag is produced by the pressure difference on the two sides of the disk surface as opposed to the viscous shear stress, whereas the opposite is true for the disk translating edgewise. The fiber boundary layer on the surface of the disk is confined to a thin layer for large α whose thickness is proportional to α^{-1}. For the pressure driven flow past a stationary particle of non-vanishing volume, the pressure contribution to the drag is of $O(\alpha^2)$ and thus much

larger than the viscous shear stress contribution at large α. In contrast, for the translating particle, these large values of α may never be achieved. As α approaches the critical value that allows the disk to move broadside, the drag on the disk will become infinitely large. In this limit, individual particle-fiber interactions dominate and the effective medium approach of the Brinkman equation cannot be used for any particle orientation.

2.3 Rotation of a Circular Disk in a Brinkman Medium

Rotational motion of a sphere in a Brinkman medium was studied by Solomentosov and Anderson (1996) using separation of variables of the governing equations in spherical coordinates. For rotational motion of a disk about its axis, a similar procedure to that for the broadside translation can be applied to obtain the solution, whereas for rotation of a disk about its diameter, the resulting motion is three dimensional and the general solution can be expressed in the form of equations (2.2.40)-(2.2.42) using cylindrical coordinates.

2.3.1 Rotation of a Disk about its Axis of Symmetry

When a circular disk is rotating about its axis of symmetry with angular velocity Ω, the only non-vanishing component of velocity $\mathbf{u} = V\mathbf{e}_\theta$ is governed by

$$\nabla^2 V - \frac{V}{\rho^2} = \alpha^2 V \tag{2.3.1}$$

in a cylindrical coordinate system (ρ, θ, z) in which z-axis is the axis of symmetry. The general solution of (2.3.1) can be expressed as

$$V = \int_0^\infty A(k) \frac{k}{\sqrt{k^2+\alpha^2}} e^{-\sqrt{k^2+\alpha^2}|z|} J_1(k\rho) dk, \tag{2.3.2}$$

where J_1 is the Bessel function of order 1 and $A(k)$ is an arbitrary unknown function to be determined by satisfying the mixed boundary condition at $z = 0$. The velocity condition on

the surface of the disk and the continuity of shear stress at the fluid interface $z = 0$ ($\rho > 1$) yield the following dual integral equations

$$\int_0^\infty A(k)\frac{k}{\sqrt{k^2+\alpha^2}}J_1(k\rho)dk = \rho\Omega \qquad (0 \le \rho \le 1), \tag{2.3.3}$$

$$\int_0^\infty kA(k)J_1(k\rho)dk = 0 \qquad (\rho > 1). \tag{2.3.4}$$

The set of dual integral equations can be reduced to a Fredholm integral equation of the second kind (Sneddon 1966), which is amenable to numerical solution. Assume

$$A(k) = \int_0^1 h(t)\sin ktdt. \tag{2.3.5}$$

Then equation (2.3.4) is satisfied automatically, whereas equation (2.3.3) becomes

$$\int_0^\infty [1 - f(k)]A(k)J_1(k\rho)dk = \rho\Omega \qquad (0 \le \rho \le 1), \tag{2.3.6}$$

in which

$$f(k) = 1 - \frac{k}{\sqrt{k^2+\alpha^2}} \tag{2.3.7}$$

Substituting (2.3.5) into (2.3.6) and making use of the following integral

$$\int_0^\infty \sin ktJ_1(k\rho)dk = \begin{cases} 0 & \text{for } \rho < t, \\ \frac{t}{\rho\sqrt{\rho^2-t^2}}H(\rho - t) & \text{for } \rho \ge t, \end{cases} \tag{2.3.8}$$

one obtains

$$\int_0^\rho \frac{th(t)dt}{\sqrt{\rho^2-t^2}} - \rho\int_0^\infty f(k)\int_0^1 h(t)\sin ktdtJ_1(k\rho)dk = \rho^2\Omega. \tag{2.3.9}$$

Performing an Abel inversion on both sides of (2.3.9) yields

$$h(t)t = \frac{2}{\pi}\frac{d}{dt}\left[\int_0^\rho \frac{\Omega u^3}{\sqrt{t^2-u^2}}du + \int_0^\rho \frac{u^2}{\sqrt{t^2-u^2}}\int_0^\infty f(k)\int_0^1 h(x)\sin(kx)dxJ_1(ku)dkdu\right]. \tag{2.3.10}$$

Interchanging the order of integration and utilizing the following integral,

$$\int_0^\rho \frac{u^2 J_1(ku)}{\sqrt{t^2-u^2}}du = \frac{t}{k}\left[\frac{\sin kt}{kt} - \cos kt\right], \tag{2.3.11}$$

one can rewrite (2.3.10) as

$$h(t) = \frac{4}{\pi}t\Omega + \int_0^1 K(x,t)h(x)dx, \tag{2.3.12}$$

in which the kernel function $K(x,t)$ is given by

$$K(x,t) = \frac{2}{\pi}\int_0^\infty f(k)\sin kx \sin kt dk \tag{2.3.13}$$

Once equation (2.3.12) is solved for $h(t)$, the torque exerted by the fluid on the disk can be evaluated from

$$T = 8\pi\mu\int_0^1 h(t)tdt \tag{2.3.14}$$

Equation (2.3.12) permits a regular perturbation solution for small values of α. This can be done by expanding both the unknown function $h(t)$ and kernel function (2.3.13) in (2.3.12) in a Taylor series in α. After some algebraic manipulation, the following asymptotic expression for the torque T exerted on the disk can be obtained

$$T = \frac{32}{3}\mu\Omega\left(1 + \frac{1}{5}\alpha^2 + O(\alpha^2)\right). \tag{2.3.15}$$

It should be noted that the correction term for the torque is of order $O(\alpha^2)$ compared with $O(\alpha)$ for the drag on a disk translating edgewise in the same medium. These qualitative properties also apply to the motion of a sphere in a Brinkman medium (Solomentsov & Anderson 1996).

As $\alpha \to \infty$, $K(x,t) \to \delta(x-t)$ and the present approach breaks down. The torque on the disk for large values of α can be estimated by integrating the solution for the local one-dimensional motion of an infinite plate over the surface of the disk. Physically, as α

becomes large, the viscous layer around the surface of the disk is confined within a small distance $O(\alpha^{-1})$. Therefore, the velocity distribution on the disk can be approximated by the solution of an infinite plate translating with velocity $\Omega\rho$. This leads to the following expression for the torque

$$T \sim \alpha\pi\mu\Omega \tag{2.3.16}$$

This result can also be obtained by retaining the first term for the expansion of $k/\sqrt{k^2+\alpha^2}$ in equation (2.3.3).

For intermediate values of α, equation (2.3.12) must be solved by numerical quadrature. In our calculation, Gauss-Chebyshev quadrature was adopted again to discretize this Fredholm integral equation of the second kind, whereas the kernel was calculated by an adaptive Romberg quadrature scheme. The torque exerted on the disk was numerically evaluated from (2.3.14) once $h(t)$ was determined.

2.3.2 Rotation of a Disk about its Diameter

When the disk rotates about one of its diameters, the induced flow is three dimensional. The disk is assumed to be instantaneously at $z = 0$ and rotating about the y-axis with angular velocity Ω. This motion satisfies the following boundary conditions

$$v_\rho = v_\theta = 0, \qquad v_z = -\Omega\rho\sin\theta, \qquad 0 \le \rho \le 1, \quad z = 0, \tag{2.3.17}$$

$$v_\rho = v_\theta = 0, \qquad \frac{\partial v_z}{\partial z} = 0, \qquad \rho > 1, \quad z = 0. \tag{2.3.18}$$

where (v_ρ, v_θ, v_z) are the fluid velocity components in cylindrical coordinates.

From the boundary conditions and the symmetry of the flow field, we find that the dependence of velocity components on the azimuthal angle is a first order harmonic, i.e.

$$\mathbf{v} = (u_\rho(r,z)\cos\theta, u_\theta(r,z)\sin\theta, u_z(r,z)\cos\theta) \tag{2.3.19}$$

The general solution (2.2.4) can be used to construct the present solution. It is convenient to rewrite the velocity components in a cylindrical coordinate system so that the boundary conditions can easily be satisfied. Instead of equations (2.2.40)-(2.2.42), we now have

$$\mathbf{v} = \nabla \times \nabla \times \left(\frac{\psi}{\rho}\cos\theta \mathbf{e_z}\right) + \nabla \times \left(\frac{\chi}{\rho}\sin\theta \mathbf{e_z}\right). \tag{2.3.20}$$

Here ψ and χ are governed by

$$L_{-1}(L_{-1} - \alpha^2)\psi = 0 = (L_{-1} - \alpha^2)\chi. \tag{2.3.21}$$

The pressure and cylindrical components of velocity are given by

$$p = \mu \frac{\cos\theta}{\rho}\frac{\partial}{\partial z}L_{-1}\psi, \tag{2.3.22}$$

$$v_\rho = \left[\frac{\partial}{\partial \rho}\left(\frac{1}{\rho}\frac{\partial \psi}{\partial z}\right) + \frac{\chi}{\rho^2}\right]\cos\theta, \tag{2.3.23}$$

$$v_\theta = -\left[\frac{1}{\rho^2}\frac{\partial \psi}{\partial z} + \frac{\partial}{\partial \rho}\left(\frac{\chi}{\rho}\right)\right]\sin\theta, \tag{2.3.24}$$

$$v_z = -\frac{\partial}{\partial \rho}\left(\frac{1}{\rho}\frac{\partial \psi}{\partial \rho}\right)\cos\theta. \tag{2.3.25}$$

The solution for ψ can be expressed as

$$\psi = \psi_1 + \psi_2 \tag{2.3.26}$$

where ψ_1 and ψ_2 satisfy

$$(L_{-1} - \alpha^2)\psi_1 = 0 = L_{-1}\psi_2 \tag{2.3.27}$$

It can be shown that the boundary conditions $(v_\rho, v_\theta) = 0$ are satisfied by choosing $\chi = 0$ and

$$\psi = \int_o^\infty k^{-1}A(k)\rho J_1(k\rho)e^{-kz}dk - \int_0^\infty \frac{1}{\sqrt{k^2+\alpha^2}}A(k)\rho J_1(k\rho)e^{-\sqrt{k^2+\alpha^2}z}dk. \tag{2.3.28}$$

The unknown kernel function $A(k)$ is determined by satisfying the mixed boundary condition (2.3.18), which yields the following set of dual integral equations

$$\int_0^\infty kA(k)\left(1-\frac{k}{\sqrt{k^2+\alpha^2}}\right)J_1(k\rho)dk=\rho\Omega, \qquad 0\le\rho\le 1, \tag{2.3.29}$$

$$\int_0^\infty A(k)J_1(k\rho)dk=0, \qquad \rho>1. \tag{2.3.30}$$

By introducing

$$A(k)=\frac{2k}{\sqrt{\pi}\alpha^2}\int_0^1 th(t)\sin ktdt, \tag{2.3.31}$$

equations (2.3.29) and (2.3.30) can be reduced to an Fredholm integral equation of the second type

$$h(t)=\frac{4\Omega}{\sqrt{\pi}}+\int_0^1 h(u)K(t,u)du, \tag{2.3.32}$$

where the kernel function is given by

$$K(t,u)=\frac{2u}{\pi t}\int_0^\infty\left[1-\frac{2x^2}{\sqrt{x^2+\alpha^2}(\sqrt{x^2+\alpha^2}+x)}\right]\sin xt\sin uxdx. \tag{2.3.33}$$

The torque exerted on the disk can be expressed as

$$T=2\pi\alpha^2\int_0^\infty k^{-1}A(k)J_2(k)dk=8\sqrt{\pi}\int_0^1 t^2h(t)dt. \tag{2.3.34}$$

Following a similar procedure to that in section (2.2), we expand both $h(t)$ and the kernel function (2.3.33) in (2.3.32) in a series for small values of α. Equation (2.3.34) yields the following asymptotic solution for T

$$T=\frac{32}{3}\left(1+\frac{3\alpha^2}{10}+O(\alpha^3)\right). \tag{2.3.35}$$

Equation (2.3.32) exhibits a singularity as $\alpha\to\infty$ and the solution is no longer applica-

ble. However, in this limit, the original dual integral equation (2.3.29) reduces to

$$\int_0^\infty kA(k)J_1(k\rho)dk = \rho\Omega, \qquad 0 \leq \rho \leq 1. \tag{2.3.36}$$

Tranter (1951) gives the solution for (2.3.36) and (2.3.30) as

$$A(k) = \frac{2}{3}\sqrt{\frac{2}{\pi k}}J_{5/2}(k). \tag{2.3.37}$$

The torque in this limit is given by

$$T = \frac{16}{45}\alpha^2 + O(\alpha) \tag{2.3.38}$$

The integral equation (2.3.32) is solved numerically by the same procedure as described in section 2.2. The dimensionless torque is again calculated from (2.3.34) once $h(t)$ is determined.

2.3.3 Results for the Torque on a Disk Rotating in a Brinkman Medium

Consider first the rotation of a disk about its axis. The dimensionless torque normalized by the Stokes torque, $\frac{32}{3}\mu\Omega$ is plotted in figure 2.5, together with the two asymptotic solutions for small and large values of α. For out-of-plane rotation, a similar procedure to that described for in-plane rotation about its axis is employed to solve the integral equation numerically. The variation of the torque normalized by the Stokes torque is plotted as a function of α in fig 2.6. One notes that the effect of the dimensionless permeability parameter α on the torque of the particle is weaker than for the drag at small values of α. Comparing the results for the torque exerted on a rotating sphere of the same diameter in the same medium, one finds that the torque on the disk can never exceed that for the sphere.

It is of interest to verify if there are any other differences between the torque on a rotating

disk and a stationary disk in which the medium is undergoing a rigid-body rotation other than the sign of the solution. If we choose a local velocity of the reference frame as $\mathbf{U}$ and rewrite the Brinkman equation as

$$\nabla p = \mu \nabla^2 \mathbf{v} - \frac{\mu}{K_p} (\mathbf{v} - \mathbf{U}) , \tag{2.3.39}$$

it can be proven that the rigid-body rotation, $\omega \times \mathbf{r}$, is not a solution unless the reference velocity $\mathbf{U}$ is appropriately specified. If a particle that is held stationary in a Brinkman medium undergoes rigid rotation, one can define $\mathbf{U} = -\omega \times \mathbf{r}$, corresponding to a coordinate system rotating with the ambient medium. The disturbed velocity in this frame is $\mathbf{v}_1$ so that the physical velocity is $\mathbf{v} = \mathbf{U} + \mathbf{v}_1$. Then $\mathbf{v}_1$ will satisfy the equation (2.3.39) with reference velocity $\mathbf{U} = 0$ and the resulting torque is just the negative of the results for rotation of the particle in the quiescent medium. This conclusion differs from the translational motion of the particle with non-vanishing volume, in which the difference is proportional to the volume of the particle.

2.4 Concluding Remarks

In this paper, solutions to the Brinkman equation are obtained for a disk moving arbitrarily in an unbounded Brinkman medium. The drag and torque exerted by the medium are found via asymptotic methods for both small and large values of the permeability parameter α and by numerical quadrature for intermediate values of α. The most important result obtained is that the drag and torque are strongly dependent upon the orientation of the disk, which is in sharp contrast to creeping flow. It is apparent that in the broadside translation and out-of-plane rotation, the medium around the disk is displaced and has to move around the disk, whereas in the edgewise translation and in-plane rotation, the medium is just sheared and little fluid has to move through the medium. This suggests that the drag on a disk translating broadside and the torque on a disk rotating about its diameter will be much

larger at high values of α than those for a disk translating edgewise and rotating about its axis, respectively. Numerical results for the drag and torque on a disk either translating or rotating at an arbitrary orientation angle are plotted in figure 2.7 for α up to 10 by combining the four fundamental motions in figure 2.1. It can be seen that dependence of the drag and torque on the orientation is quite strong.

Finally, we can combine the results presented in the previous sections to describe the flow field generated by a disk in arbitrary motion in a manner that is analogous to creeping flow. When a disk translates with velocity $\mathbf{U}_0$ and rotates with angular velocity $\mathbf{\Omega}_0$ in a Brinkman medium, the resulting drag and torque exerted by the medium will satisfy relationships (Tanzosh & Stone 1996; Happel & Brenner 1983)

$$\mathbf{F} = -\mathbf{A} \cdot \mathbf{U}_0 - \mathbf{C}^t \cdot \mathbf{\Omega}_0, \qquad \mathbf{T} = -\mathbf{C} \cdot \mathbf{U}_0 - \mathbf{B}^t \cdot \mathbf{\Omega}_0 \tag{2.4.1}$$

in which the second order tensors $\mathbf{A}$, $\mathbf{B}$ and $\mathbf{C}$ are the resistance, rotation and coupling tensors, respectively. These tensors depend only upon the geometry of the particle and the properties of the medium. For the disk motion, we have

$$\mathbf{A} = \begin{bmatrix} F_b & 0 & 0 \\ 0 & F_b & 0 \\ 0 & 0 & F_e \end{bmatrix}, \qquad \mathbf{B} = \begin{bmatrix} T_i & 0 & 0 \\ 0 & T_o & 0 \\ 0 & 0 & T_o \end{bmatrix}, \qquad \mathbf{C} = \mathbf{0} \tag{2.4.2}$$

where the subscripts b and e represent broadside and edgewise translations and i and o represent in-plane and out-of-plane rotations, respectively.

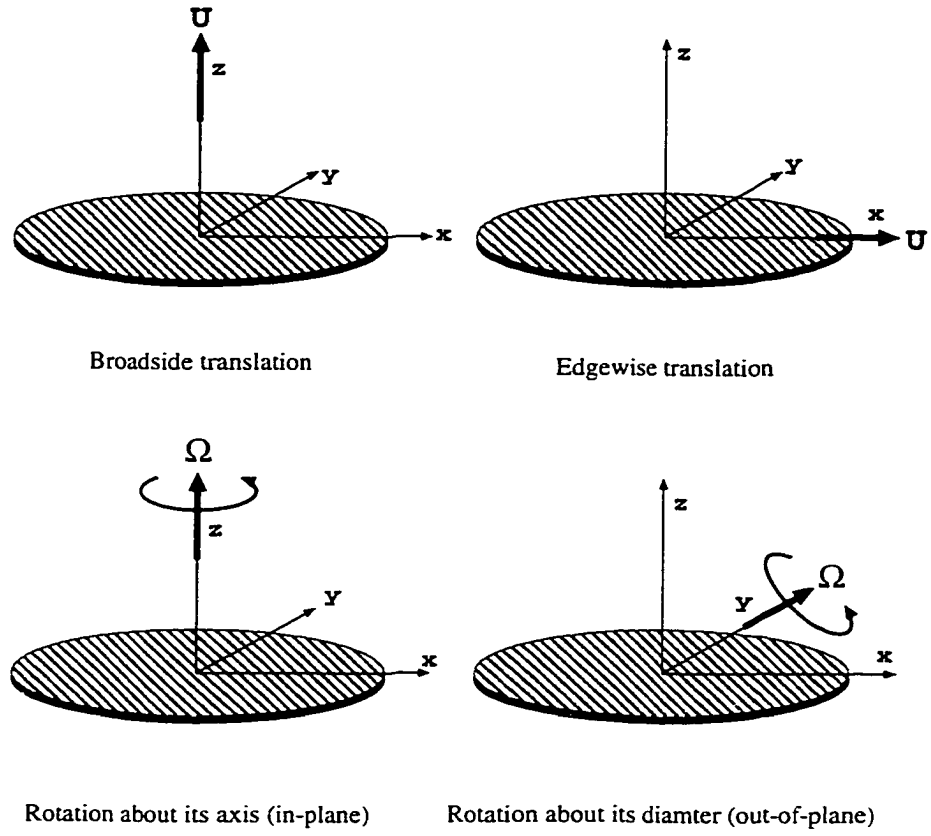

Figure 2.1: Four elementary motions studied in the present paper.

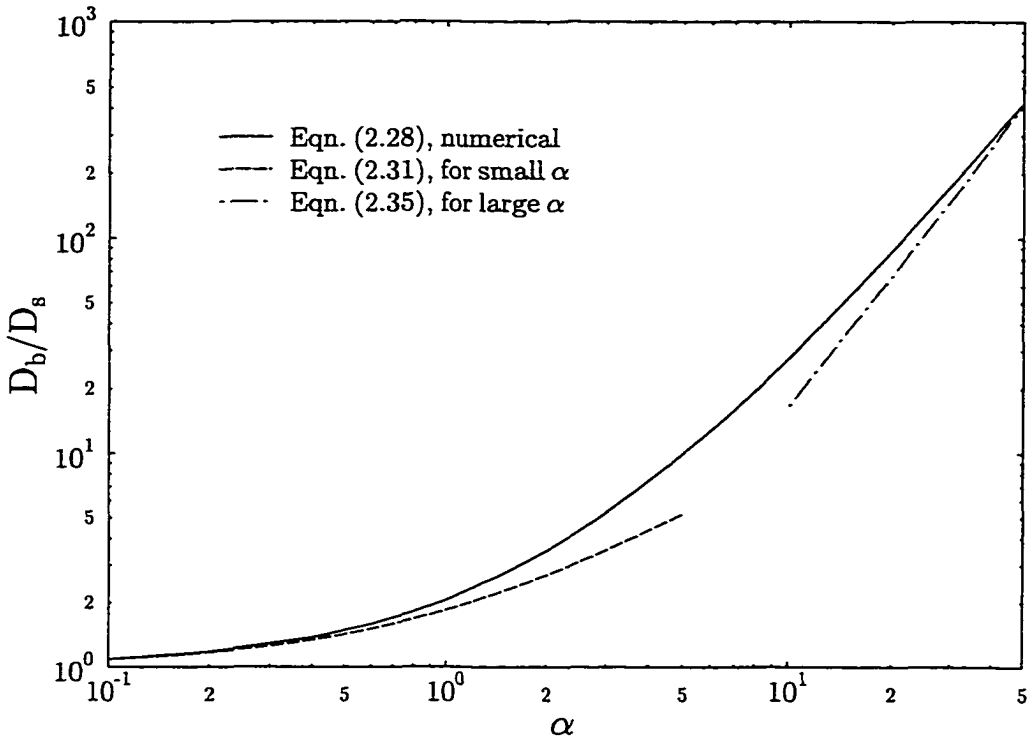

Figure 2.2: Drag on a disk translating broadside in a Brinkman medium normalized by the Stokesian drag $D_s = 16\mu U_0$ for same motion.

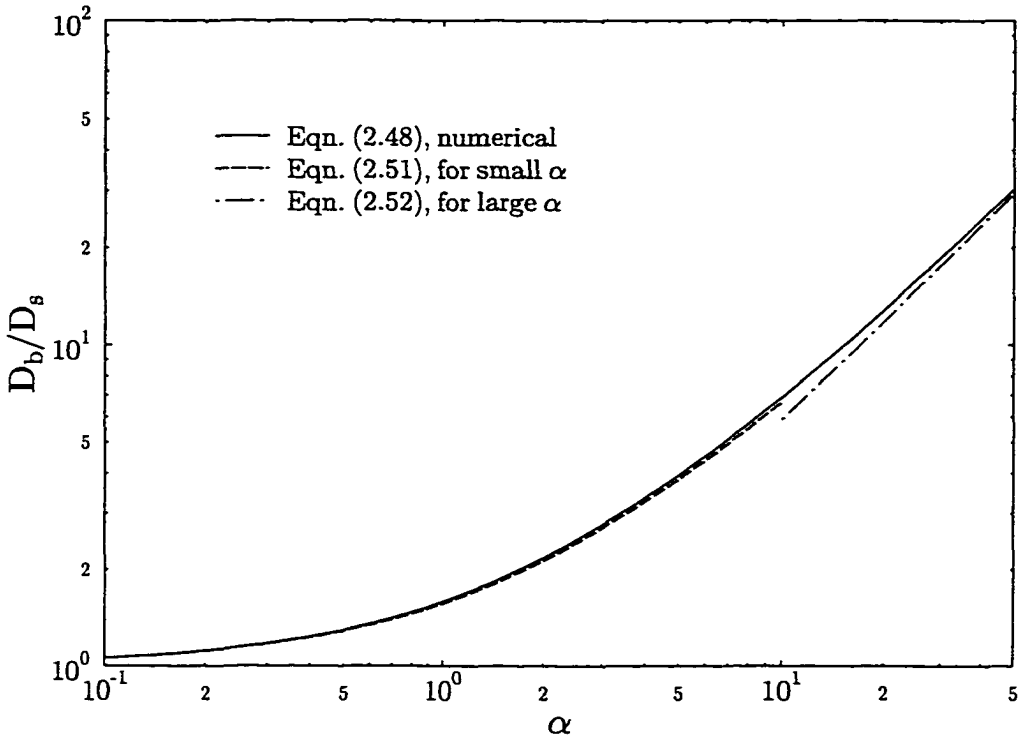

Figure 2.3: Drag on a disk translating edgewise in a Brinkman medium normalized by the Stokesian drag $D_s = \frac{32}{3}\mu U_0$ for same motion.

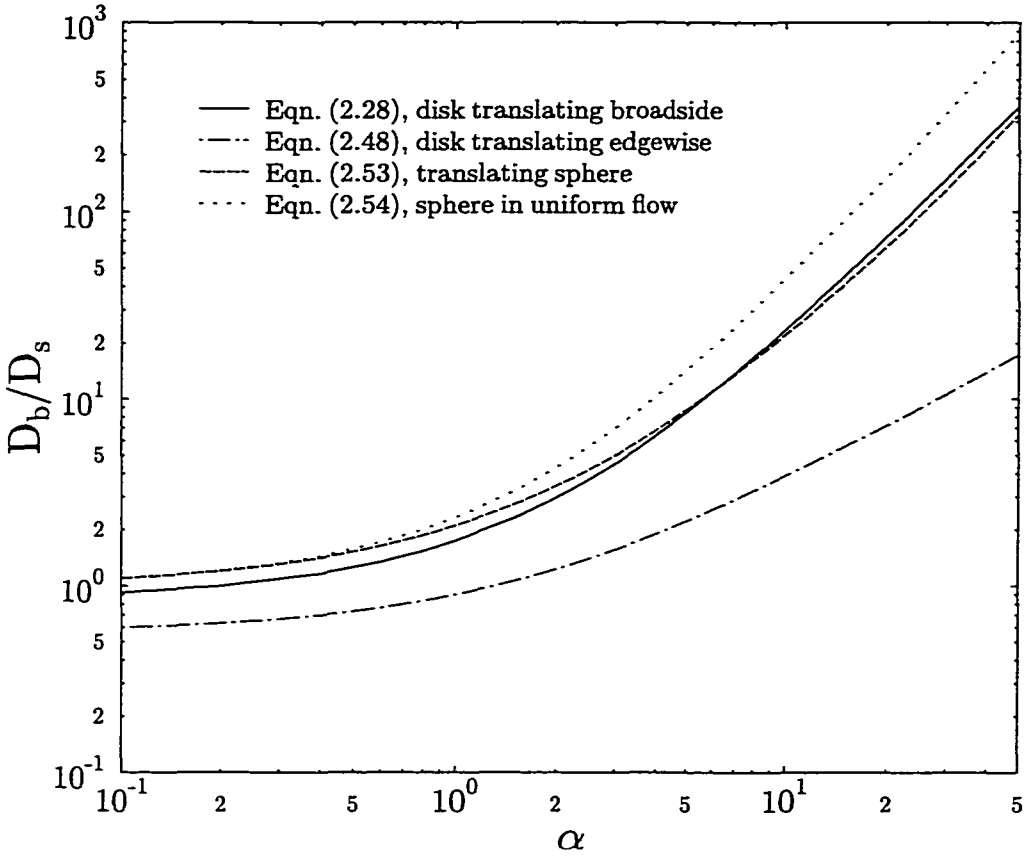

Figure 2.4: Comparison of dimensionless drag on a disk translating either broadside or edgewise with the drag on a translating sphere of the same diameter in a Brinkman medium. Results are normalized by the value of the drag on a sphere translating with the same velocity in Stokes flow, $D_s = 6\pi\mu U_0$

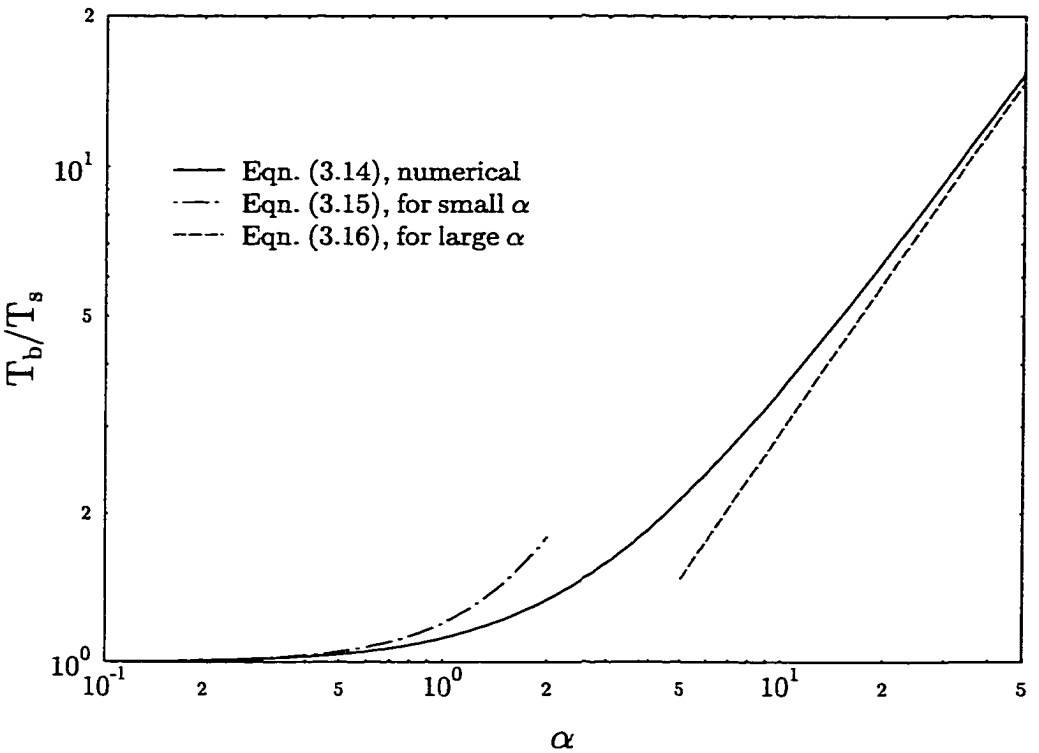

Figure 2.5: Torque on a disk rotating about its axis in a Brinkman medium normalized by the Stokesian torque $T_0 = \frac{32}{3}\mu\Omega$.

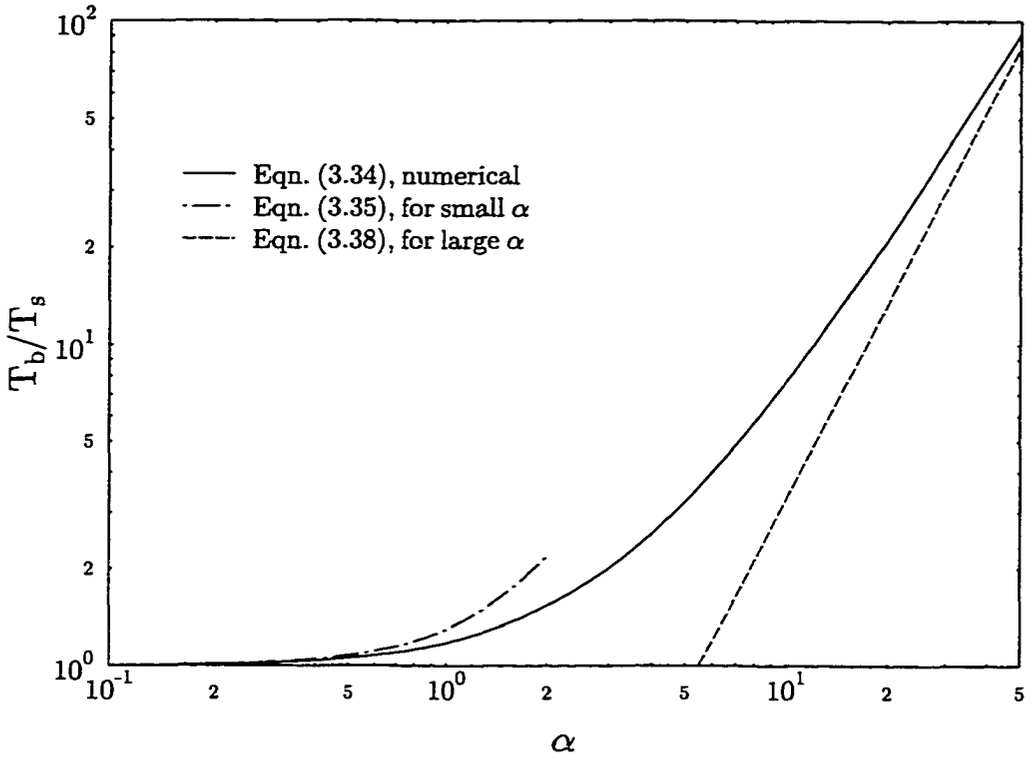

Figure 2.6: Torque on a disk rotating about one of its diameters in a Brinkman medium normalized by the Stokesian torque $T_0 = \frac{32}{3}\mu\Omega$.

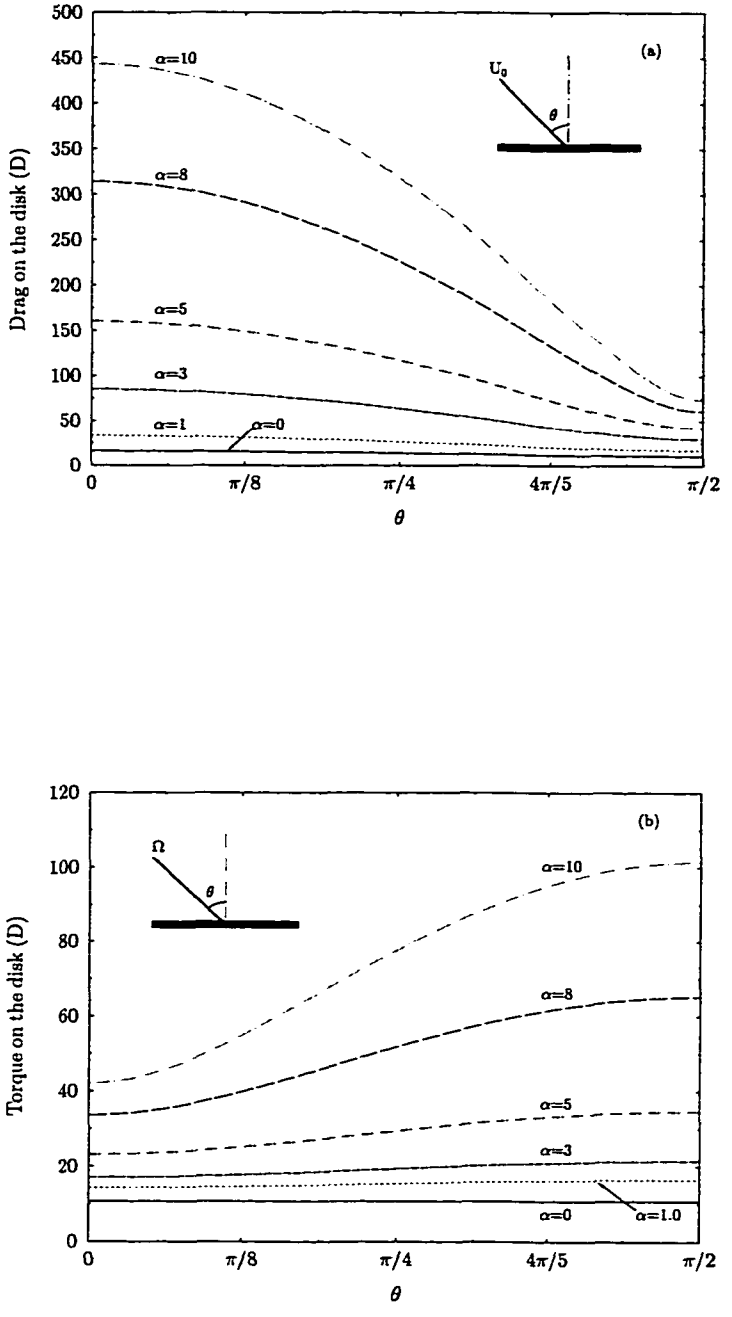

Figure 2.7: Variation of the normalized drag and torque on a disk translating (a) or rotating (b) in a Brinkman medium with its orientation angle.

Chapter 3 Flow Through an Orifice in a Fibrous Medium with Application to Fenestral Pores in Biological Tissue

3.1 Introduction

One of the well known solutions in Stokes flow is the classical solution of Sampson (see Happel & Brenner 1983) for the slow viscous flow of a fluid through a circular orifice in a plane wall. This classical solution was extended to flow through a finite length circular pore in Dagan *et al.* (1982). In this paper, we shall consider both of these problems for a planar wall that is bounded by a fiber-filled medium, see Fig. 3.1. This problem has arisen in several important biological applications where there are impermeable cellular or elastic tissue boundaries which have orifice-like openings that control the flux of water and solutes. Two problems of long standing interest are the circular orifice-like openings in the endothelium of fenestrated capillaries and the fenestrated pores in the internal elastic lamina (IEL) that separates the intima from the media of the artery wall. In both cases the tissue that surrounds the orifice or pore is a fibrous medium composed of collagen and proteoglycan fibers. The dominant resistance usually derives from the proteoglycan fibers because of their far greater density and nearly uniform distribution on the length scale of the orifice diameter. A crude schematic of the fibrous matrix surrounding the opening of a fenestral pore in a capillary membrane is shown in Fig. 3.2. In this study we shall be interested in examining both the velocity profile and pressure drop across the orifice where the permeability parameter α describing the fiber spacing spans the entire range from $\alpha = 0$, Sampson flow, to $\alpha >> 1$, Darcy flow.

In this paper, we develop a theoretical model based on an effective medium theory, i.e. the Brinkman equation, to describe these flows. This research is motivated not only

by its biological applications but also by a mathematical analogy to the complementary flow problem, the broadside translation of a circular disk in either Stokes or Darcy flow. Recently, Feng *et al.* (1998) studied the general motion of a circular disk in an unbounded Brinkman medium using a dual integral equation method. The authors found that the pair of dual integral equations governing the boundary conditions for the broadside translation of a circular disk in Darcy flow also arises for Sampson flow through an orifice in a plane wall. The drag experienced by the disk is calculated in a similar way to the total flux of fluid through the orifice. In the next section, this analogy will be explored further.

The effective medium theory based on the Brinkman equation has often been used to describe the flow in a fiber-filled medium. The validity and accuracy of this theory is elucidated by subsequent theoretical analyses in which one either averages the solution for Stokes flow past a cloud of spherical particles (Tam, 1967) or renormalizes the Stokes equation for fluid motion past a random assemblage of particles or cylindrical fibers (Howells, 1974; 1998). It is found that the Brinkman equation is the leading order approximation in the low solid fraction limit. More recent numerical investigation using a Stokesian dynamics simulation has shown that the fundamental solution for the Brinkman medium accurately describes the Stokes flow in the near field and the dipole flow in the far field of a moving particle provided the solid fraction c is less than 5 percent. As the solid fraction increases, the Brinkman equation loses its accuracy but still gives the qualitative variation of the fundamental solution for c as high as 20 percent (Durlofsky & Brady, 1987). Mathematically, the Brinkman equation, together with Darcy's law, has also been derived by a homogenization technique based on matched asymptotic analysis for flow in periodic structures (Hornung 1996). These studies have provided a more rigorous basis for effective medium theory.

The validity of the Brinkman equation in the limit where the fiber spacing is large compared to the pore size is subtle. Although the Brinkman equation in this limit does predict accurate results for the hydraulic resistance, the velocity field does not approach the Stokes approximation in all of space. The fundamental solution to the Brinkman equation for the velocity field behaves as a dipole which decays as r^{-2} compared to the Stokeslet

which decays as r^{-1}. Mathematically, the Darcy term can be neglected when $\alpha << 1$ provided $O(\alpha^2 \boldsymbol{u}) < O(\nabla^2 \boldsymbol{u})$. Since the viscous dissipation term decays faster than the Darcy term in the far field, analogous to the Whitehead paradox for flow past a sphere, the Brinkman solution is only valid in a region bounded by $r = O(\alpha^{-1})$. Small particles diffusing in a sparse ordered matrix have been studied by Phillips *et al.* (1989, 1990) using a Stokesian dynamic simulation technique. They demonstrated that the Brinkman equation is a good approximation for the far field interaction between the mobile particle and the fibers, and that in the small α limit this far field interaction dominates the contribution arising from the local inhomogeneity of the medium due to the existence of the particle.

The advantage of the Brinkman equation lies in its simplicity in application. Only one additional parameter, K_p, is needed to characterize the permeability of the porous media. Once K_p has been determined by either experimental measurement or theoretical model, knowledge of the detailed structure of the porous media is not necessary provided the entire medium is homogeneous and macroscopically isotropic, i.e., on the length scale of the orifice diameter in our problem. This is particularly useful since in many complicated biological or chemical engineering systems, a thorough knowledge of the microstructure is usually not clear *a prior*. However, the hydraulic permeability of a uniform porous medium is easy to measure or theoretically estimate. For example, Tsay & Weinbaum (1991) have shown that the simple relation

$$K_p = 0.0572 r_f^2 \left(\frac{\Delta}{r_f}\right)^{2.377}, \tag{3.1.1}$$

for slow viscous flow through a doubly periodic square array of cylindrical fibers provides a good approximation to the numerical solution of Sangani & Acrivos (1982) for fiber volume fractions of less than 70 percent. Here r_f is the fiber radius and Δ is the fiber spacing between two adjacent fibers. In the present paper, we will use equation (3.1.1) to estimate the bulk permeability of the tissue in the subendothelial region of capillaries.

Mathematically, the Brinkman equation is equivalent to the governing equation for the oscillatory motion of a particle in an otherwise quiescent Stokes flow. The general solution

involves a Helmoholtz equation. Unfortunately, the Helmoholtz equation is not separable in a toroidal coordinate system; therefore, the conventional method used in deriving Sampson's solution does not work in the present problem (Happel & Brenner 1983).

In section 3.2, we present the problem formulation and apply the Abel transformation technique to reduce the resulting dual integral equations to a Fredholm integral equation of the second kind. Asymptotic solutions for small and large values of the permeability parameter

$$\alpha = \frac{a}{\sqrt{K_p}} \tag{3.1.2}$$

are derived and numerical calculations for intermediate values of α are performed in section 3.3. This is followed by an extension of the model accounting for the effect of a circular pore of finite length in a plane wall. In section 3.5 we discuss the corresponding two-dimensional problem. Finally, we conclude the paper with a brief analysis of the two biological problems that motivated this study in section 3.6.

3.2 Mathematical Formulation

The Brinkman equation together with the continuity equation

$$\nabla p = \mu \nabla^2 \boldsymbol{v} - \frac{\mu}{K_p} \boldsymbol{v} \tag{3.2.1}$$

$$\nabla \cdot \boldsymbol{v} = 0 \tag{3.2.2}$$

are used in this section to study the pressure driven flow through a circular orifice in a wall embedded in a fibrous material. The momentum equation (3.2.1) combines both the effect of viscous stresses and the effect of a distributed Darcy force which is characterized by the Darcy permeability K_p. K_p depends on the structure of the media, which in this study is approximated by equation (3.1.1).

It is convenient to formulate the problem in terms of dimensionless cylindrical coordinates

(unprimed) which relate to dimensional coordinates (primed) by

$$R = \frac{R'}{a}, \qquad Z = \frac{Z'}{a}$$

Here we choose the orifice radius as the characteristic length scale a. The characteristic pressure and velocity are

$$P_0 = \Delta p' = p'_{-\infty} - p'_{+\infty}, \qquad V_0 = \frac{aP_0}{\mu},$$

where $\Delta p'$ is the pressure difference across the orifice at plus and minus infinity which drives the flow and μ is the viscosity. If we introduce the dimensionless permeability parameter α and write the governing equations in dimensionless cylindrical coordinates (R, ϕ, Z) (prime omitted hereafter) originating at the orifice center, with the Z-axis as the axis of symmetry, see Fig. 3.1(a).,

$$\nabla p = (\nabla^2 - \alpha^2)\boldsymbol{v}, \tag{3.2.3}$$

$$\nabla \cdot \boldsymbol{v} = 0. \tag{3.2.4}$$

The velocity and pressure are subject to the following boundary conditions

$$\boldsymbol{v} = 0, \qquad Z = 0, R > 1 \tag{3.2.5}$$

$$[p]_{-0}^{+0} = 0, \quad Z = 0, 0 < R < 1 \tag{3.2.6}$$

$$[p]_{-\infty}^{+\infty} = -1. \tag{3.2.7}$$

Following Feng *et al.* (1998), we introduce a dimensionless axisymmetric stream function

$$\boldsymbol{v} = \nabla \times \left[-\frac{\psi}{R}\boldsymbol{e}_\phi\right], \tag{3.2.8}$$

which satisfies

$$L_{-1}(L_{-1} - \alpha^2)\psi = 0. \tag{3.2.9}$$

Here the characteristic value for ψ is defined by

$$\psi_0 = a^2 V_0.$$

The Stokesian operator is defined by

$$L_{-1} = \frac{\partial^2}{\partial R^2} - \frac{1}{R}\frac{\partial}{\partial R} + \frac{\partial^2}{\partial Z^2} \tag{3.2.10}$$

and the corresponding pressure field is obtained from the solution of

$$\frac{\partial p}{\partial Z} = \frac{1}{R}\frac{\partial}{\partial R}[L_{-1} - \alpha^2]\psi, \tag{3.2.11}$$

$$\frac{\partial p}{\partial R} = -\frac{1}{R}\frac{\partial}{\partial Z}[L_{-1} - \alpha^2]\psi. \tag{3.2.12}$$

The suitable solution to (3.2.9) can be expressed as

$$\psi = \psi_1 + \psi_2, \tag{3.2.13}$$

where

$$\psi_1 = \int_0^\infty R J_1(kR) A(k) e^{-k|Z|} dk \tag{3.2.14}$$

$$\psi_2 = -\int_0^\infty R J_1(kR) \frac{k}{\sqrt{k^2+\alpha^2}} A(k) e^{-\sqrt{k^2+\alpha^2}|Z|} dk. \tag{3.2.15}$$

Solution (3.2.13) satisfies the radial no-slip condition (3.2.5) on the wall. The corresponding pressure which satisfies condition (3.2.7) is given by

$$p_\pm = p_{\pm\infty} \pm \alpha^2 \int_0^\infty J_0(kR) A(k) e^{-k|Z|} dk. \tag{3.2.16}$$

The other two conditions on the orifice plane lead to the following dual integral equations

$$\int_0^\infty J_0(kR) A(k) dk = \frac{1}{2\alpha^2}, \quad 0 < R < 1 \tag{3.2.17}$$

$$\int_0^\infty kf(k)J_0(kR)A(k)dk = 0, \qquad R > 1, \tag{3.2.18}$$

where

$$f(k) = 1 - \frac{k}{\sqrt{k^2+\alpha^2}}. \tag{3.2.19}$$

By introducing $g(k)$ and $B(k)$ as

$$(kf(k))^{-1} = \frac{2k}{\alpha^2}(1+g(k)), \qquad 4kf(k)A(k) = B(k), \tag{3.2.20}$$

where

$$g(k) = \frac{\sqrt{k^2+\alpha^2}(\sqrt{k^2+\alpha^2}+k)}{2k^2} - 1, \tag{3.2.21}$$

the dual integral equations (3.2.17) and (3.2.18) can be transformed to standard form as follows

$$\int_0^\infty k(1+g(k))J_0(kR)B(k)dk = 1 \quad 0 < R < 1 \tag{3.2.22}$$

$$\int_0^\infty J_0(kR)B(k)dk = 0 \qquad R > 1. \tag{3.2.23}$$

The dual integrals equations (3.2.22) and (3.2.23) can be reduced to a Fredholm integral equation of the second kind, which is amenable to numerical solution. We introduce an unknown function

$$B(k) = \frac{2}{\sqrt{\pi}}\int_0^1 h(t)\sin ktdt, \quad h(0) = 0 \tag{3.2.24}$$

which enables equation (3.2.23) to be satisfied identically. Equation (3.2.22) is rewritten as

$$\int_0^\infty kJ_0(kR)\frac{2}{\sqrt{\pi}}\int_0^1 h(t)\sin ktdtdk = 1 - \int_0^\infty kg(k)J_0(kR)\frac{2}{\sqrt{\pi}}\int_0^1 h(t)\sin ktdtdk \tag{3.2.25}$$

If we exchange the order of integration and perform an integration by parts, we find that

the first integral in (3.2.25) can be evaluated as

$$\frac{2}{\sqrt{\pi}}\int_0^R \frac{h'(t)}{\sqrt{R^2-t^2}}dt$$

where we have used the discontinuity integral of the Bessel function

$$\int_0^\infty J_0(kR)\cos ktdt = \begin{cases} 0, & 0<R<t \\ \frac{1}{\sqrt{R^2-t^2}}, & R>t \end{cases} \tag{3.2.26}$$

Making use of the Abel transform in (3.2.25), we obtain the following integral equation

$$h(t) + \int_0^1 h(u)K(u,t)du = H(t) \tag{3.2.27}$$

in which

$$H(t) = \frac{1}{\sqrt{\pi}}\int_0^t \frac{u}{\sqrt{t^2-u^2}}du = \frac{t}{\sqrt{\pi}} \tag{3.2.28}$$

$$K(u,t) = \frac{2}{\pi}\int_0^\infty g(x)\sin xt \sin xudx. \tag{3.2.29}$$

Once the solution for h(t) is determined, the dimensionless flux Q through the orifice, normalized by ψ_0, is calculated by

$$Q = 2\pi\int_0^1 RdR\int_0^\infty kJ_0(kR)A(k)dk = \sqrt{\pi}\int_0^1 h(t)tdt. \tag{3.2.30}$$

Cast in this new form, on can easily obtain the asymptotic solutions for small and large values of α. In the Stokes limit, i.e. $\alpha \to 0$,

$$f(k) \to \frac{\alpha^2}{2k^2}, \qquad g(k) \to 0$$

and the dual integral equations (3.2.22) and (3.2.23) reduce to

$$\int_0^\infty kJ_0(kR)B(k)dk = 1 \quad 0<R<1 \tag{3.2.31}$$

$$\int_0^\infty J_0(kR)B(k)dk = 0 \qquad R > 1. \tag{3.2.32}$$

We notice that these dual integral equations are exactly the same as those that arise in the broadside translation of a circular disk in a Darcy medium (Feng *et al.* 1998). On the other hand, in the Darcy limit where $\alpha \to \infty$, $f(k) \to 1$ and equations (3.2.17) and (3.2.18) reduce to

$$\int_0^\infty J_0(kR)A(k)dk = \frac{1}{2\alpha^2} \quad 0 < R < 1, \tag{3.2.33}$$

$$\int_0^\infty kJ_0(kR)A(k)dk = 0 \qquad R > 1, \tag{3.2.34}$$

which also appear for broadside translation of a circular disk in Stokes flow (Davis 1991). The corresponding drag exerted on the translating disk is calculated in a manner similar to equation (3.2.30). This curious interchange of roles arises because the part of ψ that satisfies $L_{-1}\psi = 0$ produces no pressure distribution in Stokes flow, but determines the pressure in the Brinkman medium.

Solutions to these simplified dual integral equations are well known (Sneddon 1966). For (3.2.31-3.2.32), one finds, in terms of $A(k)$,

$$A(k) = \frac{1}{\pi\alpha^2}\frac{\sin k - k\cos k}{k}, \tag{3.2.35}$$

which leads to the total flux

$$Q = \frac{1}{3}, \tag{3.2.36}$$

a well-known result for Sampson flow. The solution to (3.2.33-3.2.34) for large α is

$$A(k) = \frac{1}{\pi\alpha^2}\frac{\sin k}{k}, \tag{3.2.37}$$

and consequently, the flux is given by

$$Q = \frac{2}{\alpha^2}. \tag{3.2.38}$$

The first order correction to the Sampson flow can be obtained by evaluating the kernel function $K(u,t)$ for small values of α and expanding the integral equation (3.2.27) in a regular series in α

$$h(t) = h_0(t) + \alpha h_1(t) + \alpha^2 h_2(t) + \cdots, \tag{3.2.39}$$

whose first few terms are

$$h_0(t) = \frac{t}{\sqrt{\pi}}, \quad h_1(t) = 0, \quad h_2(t) = \frac{t^3 - 3t}{8\sqrt{\pi}}. \tag{3.2.40}$$

The correction to the flux is

$$Q = \frac{1}{3}\left(1 - \frac{3}{10}\alpha^2 + O(\alpha^4)\right). \tag{3.2.41}$$

Note that the correction to the Sampson flux is $O(\alpha^2)$, in comparison with $O(\alpha)$ for the correction to the drag on a translating disk in the same medium.

The hydraulic conductance per unit area is normalized by the dimensionless Sampson result,

$$L_p = \frac{L_p'}{a/3\pi\mu} = \frac{3Q'\mu}{\Delta p' a^3} = 3Q = 3\sqrt{\pi}\int_0^1 h(t)t\,dt \tag{3.2.42}$$

The integral equation (3.2.27) is solved for intermediate values of α by a numerical method described in Feng *et al.* (1998). The normalized conductance is calculated numerically from (3.2.42) once $h(t)$ is determined. These numerical results together with the asymptotic solutions valid for small and large α are presented in the next section.

3.3 Results and Discussion

The calculated conductance for a circular orifice in a plane wall embedded in a fiber filled medium obtained using equation (3.2.42) is shown by the solid curve in Fig. (3.3). This result is compared with the two asymptotic approximations for small and large values of α. It can be seen that the conductance of the orifice is considerably reduced due to the presence of the fibrous medium as α increases. When $\alpha = 1$, there is about 20% reduction in conductance. This value of α corresponds to the situation where the fiber spacing is roughly comparable to the orifice diameter. In some biological applications involving fenestral pores, $\alpha = O(10)$ or larger and expression (3.2.38) is a good approximation.

Once the unknown function $h(t)$ has been determined, we are able to the calculate velocity and pressure fields using (3.2.8) and (3.2.16), respectively. We are particularly interested in the velocity profile at the opening of the orifice, which can be expressed as

$$\begin{aligned} v_z &= \frac{1}{2\sqrt{2}} \int_R^1 \frac{h(t)}{\sqrt{t^2 - R^2}} dt \\ &= \int_0^{\cosh^{-1}\frac{1}{R}} h(R\cosh x) dx \end{aligned} \tag{3.3.1}$$

in which we have changed the variable of integral to eliminate singularity near the rim $R = 1$.

Numerical calculations of the profiles for various values of the parameter α are shown in Fig. 3.4(a, b). We note that as α increases, the profile becomes flatter and flatter and eventually exhibits a transition in behavior from Sampson flow to inviscid Darcy flow. For $\alpha >> 1$, the velocity profile at the opening has a minimum at the orifice center, rises sharply near the edge of the orifice and then experiences a boundary-layer-like correction of thickness $O(1/\alpha)$ to satisfy the no-slip boundary condition at the orifice edge, as shown in Fig. 3.4(b). The flow patterns for $\alpha = 0$, 2, 10 and 20 are shown in Fig. 3.5 and the corresponding pressure fields are illustrated in Fig 3.6. In the two limiting cases, the stream lines and isobars are given in closed form by applying integrals discussed in Tanzosh &

Stone (1996) by

$$\psi = \frac{1}{6\pi}(1-\zeta^3), \qquad p = \frac{1}{\pi}\left(\tan^{-1}\lambda + \frac{\lambda}{\lambda^2+\zeta^2}\right), \tag{3.3.2}$$

for Sampson flow, and

$$\psi = \frac{1}{\pi\alpha^2}\frac{R}{1+\lambda^2}\sqrt{\frac{1-\zeta}{1+\zeta}}, \qquad p - p_{+\infty} = \frac{1}{\pi}\cot^{-1}\lambda, \tag{3.3.3}$$

for Darcy flow, where the oblate spheroidal coordinates are defined by

$$R = \sqrt{1+\lambda^2}\sqrt{1-\zeta^2}, \quad 0 \le \lambda < \infty, \quad -1 \le \zeta \le 1 \tag{3.3.4}$$

$$Z = \lambda\zeta, \quad 0 \le \lambda < \infty, \quad -1 \le \zeta \le 1. \tag{3.3.5}$$

The stream lines are qualitatively similar in the four panels in Fig. 3.6, except that the flow converges at the edge of the orifice as α increases. This is expected since the Darcy flow, which has a potential flow streamline pattern, is the limiting case for large α and the no slip condition is not satisfied at the orifice edge. The pressure distribution changes dramatically as α increases. For the creeping limit, where $\alpha = 0$, the edge of the pore is a singular point and there is negative pressure near the boundary surface as previously shown in Weinbaum (1968). This negative pressure region shrinks as α increases and eventually disappears. For large values of α, the pressure distribution for the Brinkman medium reduces to the Darcy approximation, where the isobars are confocal ellipses, as shown in Fig. 3.6.

Similar behavior has been observed for Hele-Shaw flow through an orifice in a planar barrier confined between two parallel walls in a channel (Zeng & Weinbaum 1994). The variation in the velocity profile in Fig. 3.4 is also observed in the mathematically equivalent problem of oscillatory Stokes flow through an orifice. The similarity between the Hele-Shaw and Darcy orifice profiles arises because both flows satisfy a potential flow equation with

slip boundary conditions on the orifice wall.

It is interesting to try and understand why the velocity profiles obtained in this study when $\alpha >> 1$ are so similar to those for flow past a periodic array of slits in a planar barrier confined in a narrow channel of height $2h$ when the no-slip orifice edge condition is satisfied (Zeng & Weinbaum 1994). For the classical Hele-Shaw approximation, the velocity variation is of the form

$$\boldsymbol{V}(x_1, x_2, x_3) = \boldsymbol{v}(x_1, x_2) Z(x_3) \tag{3.3.6}$$

where $\boldsymbol{v} = v_1 \boldsymbol{e}_1 + v_2 \boldsymbol{e}_2$ represents the unknown two-dimensional velocity field in planes parallel to the wall and

$$Z(x_3) = \frac{6}{h^2}(x_3 h - x_3^2) \tag{3.3.7}$$

is a scalar function which describes a Poiseuille profile in the x_3 or vertical direction. An evaluation of the Stokes equation with the assumed velocity field (3.3.6) leads to the condition, $\partial p / \partial x_3 = 0$. Thus, the pressure is a function of (x_1, x_2) only when the vertical velocity vanishes.

Suppose now that the viscous stresses in the x_1 and x_2 directions are not neglected, but we still require that the velocity field be of the form of (3.3.6). If this velocity field is substituted into the x_1 and x_2 components of the Stokes equation and integrated with respect to x_3, we obtain the following equation

$$\nabla p = \mu \left(\nabla^2 - \frac{12}{h^2} \right) \boldsymbol{v}. \tag{3.3.8}$$

This is exactly the Brinkman equation if the permeability parameter is defined as

$$\alpha = \frac{2\sqrt{3}L}{h},$$

where L is the characteristic length of the barrier. Thus, equation (3.3.8) is a correction to the classical Hele-Shaw approximation in which the pressure gradient in the x_3 direction

can be neglected, but the no-slip boundary condition on the side walls of the barrier are satisfied in contrast to the classic Hele-Shaw approximation. Equation (3.3.8) will be valid if the channel height is small compared to the barrier dimensions. Physically, the second term in parentheses in (3.3.8) can be interpreted as an average or distributed friction force due to the channel walls.

Note that equation (3.3.8) resembles the governing equation describing the velocity disturbance generated by a cylinder moving in a lipid bilayer when a non-zero force is applied (Saffman 1976). This solution is used to describe the Brownian diffusion of the cylinder in the plane of the bilayer. However, the boundary conditions at the edge of the cylinder is not necessarily no slip, as is the case in Hele-Shaw flow. The additional term added to the Stokes equation accounts for the Brownian driving force.

The close relationship between pressure driven flow through a circular orifice and broadside translation of the complementary geometry, namely a circular disk, is revealed by the mathematical formulation. The pressure driven flow through an orifice using Darcy's law is equivalent to the Stokes flow of a translating disk. On the other hand, the broadside translation of a disk in Darcy flow is equivalent to Sampson flow. These conclusions are also true for the two dimensional flow geometry discussed in section 3.5. One finds that the dimensional drag D' on a disk translating broadside and the dimensional flux Q' through the complementary orifice satisfy the following relations,

$$\frac{D'_S}{16\mu a U'} : \frac{Q'_D}{a^3 \Delta p'/3\mu} = \frac{D'_D}{16\mu a U'} : \frac{Q'_S}{a^3 \Delta p'/3\mu} = \frac{\alpha^2}{6} \tag{3.3.9}$$

in which the subscripts D and S represent Darcy and Stokes, respectively.

3.4 Flow Through an Orifice of Finite Length

In this section, the effect of pore length is considered. The exact solution for the flow field can be obtained by using a procedure similar to that developed by Dagan *et al.* (1982) for

Stokes flow through a finite length circular pore in a plane wall. This procedure requires that one matches the solutions of the Brinkman equation inside and outside the pore. Since we are more interested in finding the conductance of the pore, rather than the detailed flow structure or pressure distribution, a simple approximate solution can be constructed.

In Dagan *et al.* (1982), it is shown that the hydraulic resistance for the flow through an orifice of the finite length into a semi-infinite space can be well approximated by combining the channel flow inside the circular orifice and the flow across an orifice of infinitesimal thickness. It is also shown that the actual velocity profile at the orifice opening is roughly the average of a Poiseuille and a Sampson flow. In the case of Stokes flow the transition from Poiseuille-like flow to Sampson-like flow is localized to a region of less than a pore radius in the vicinity of the pore opening. In the present case this transition is more difficult to describe since it also depends on the thickness of the fiber interaction layer at the pore wall. Nevertheless, this model should provide a fairly accurate estimate of the overall hydraulic conductance, but not the detailed flow pattern and pressure distribution, especially near the rim of the pore opening.

Assuming that the pressure at the orifice opening is p_i, then the solution inside the pore is given by the Brinkman solution for the flow inside an infinite circular cylinder

$$u(R) = \frac{p_0 - p_i}{\alpha_1^2 L}\left(1 - \frac{I_0(\alpha_1 R)}{\alpha_1 I_0(\alpha_1)}\right), \tag{3.4.1}$$

in which p_0 is the dimensionless pressure at the center plane of the pore, see Fig. 3.1(b). The corresponding flux is given by

$$Q = 2\pi \int_0^1 u(R) R dR = \frac{\pi(p_0 - p_i)}{\alpha_1^2 L}\left(1 - \frac{2I_1(\alpha_1)}{\alpha_1 I_0(\alpha_1)}\right), \tag{3.4.2}$$

where α_1 describes the Darcy permeability of the fiber matrix inside the pore.

Outside the orifice, we apply the solution (3.2.30) derived in the previous section, i.e.

$$Q = 2\sqrt{\pi}(p_i - p_\infty)\int_0^1 h(t)tdt, \tag{3.4.3}$$

where the factor 2 appears to account for the two half spaces at the entrance and exit. Note that these regions can be described by a different matrix permeability parameter α_2. Combining the above solutions and making use of the continuity of the flux at the opening to eliminate the interface pressure p_i, one obtains the following expression for the conductance of a pore of finite length

$$L_p = \frac{L'_p}{a/3\pi\mu} = 3Q = 3\Pi(\alpha_1, \alpha_2, L)^{-1}, \tag{3.4.4}$$

where the function $\Pi(\alpha_1, \alpha_2, L)$ represents the additional pressure drop required to generate the same flux as that required for a flow through the zero-thickness orifice, where $\Pi = 3$. This function is given by

$$\Pi(\alpha_1, \alpha_2, L) = \frac{1}{\sqrt{\pi}\int_0^1 h(t)tdt} + \frac{2\alpha_1^3 L I_0(\alpha_1)}{\pi(\alpha_1 I_0(\alpha_1) - 2I_1(\alpha_1)}. \tag{3.4.5}$$

The calculated permeability L_p as a function of pore length L is shown in Fig. 3.7 for various values of α. Two sets of curves are presented, one for the case where the flow in the entrance and exit half space is a Sampson flow ($\alpha_2 = 0$) and the second for the case where there is a continuous uniform matrix throughout the entire region ($\alpha_1 = \alpha_2$). The results clearly demonstrate the combined effect of the pore length and media permeability. The results for the case where there is no external matrix is of special interest in some fenestrated capillaries where a thin sieving diaphragm is believed to span the orifice opening. This will be discussed in the biological applications in section 3.6.

Of particular interest in Fig. 3.7 is the value of L'/a where the hydraulic permeability L_p is decreased by a factor of two from the results for a zero thickness orifice. Along this boundary the hydraulic resistance of the entrance and exit flow is just equal to the

pore itself. For a Sampson entrance and exit flow ($\alpha_2 = 0$, no fiber matrix), this occurs for $L_p = 3Q = 0.5$. The values of L'/a for which this occurs shifts to the left as α increases and for $\alpha_1 = 0$, reduces to the solution $L'/a = 0.589$ in Dagan *et al.* (1982). In biological applications, where a porous membrane with fiber-filled pores separates two aqueous solutions, one first needs to determine the value of α for the porous membrane region. This can be estimated using an approximate formula such as (3.1.1) if the fiber structure is known. For the case where the external half space and the pore are a continuous homogeneous media, the boundary for equal resistance shifts slightly to the right as α increases, the values of L'/a being 0.638, 0.711, 0.784 and 0.799 for $\alpha = 1$, 2, 5 and 10, respectively.

It is also convenient to plot the hydraulic resistance function Π of the pore as a function of pore length for various α_1 and α_2. The resistance is composed of two contributions, the entrance and exit regions and the pore interior as shown in (3.4.5). Results for $\alpha_1 = \alpha_2 = \alpha$ as a function of dimensionless length L'/a are shown by the heavy lines in Fig. 3.8. The thin lines are for the case where there is only matrix inside the pore, $\alpha_1 = \alpha$, and the external flow is a Sampson flow, $\alpha_2 = 0$, and $\Pi = 3$ when $L = 0$. As α_1 increases, Π becomes steeper due to the increased resistance of the internal fibers.

3.5 Two-Dimensional Flow

We can apply a procedure similar to that described in section 3.2 for two-dimensional flow to determine the pressure drop across a slit orifice in a plane wall. However, detailed inspection of the solution procedure indicates that the dual integral equations arising from the boundary condition at the slit orifice plane does not have a solution unless $\alpha = 0$. This corresponds to the well-known Stokes paradox for the two-dimensional flow past an infinitely long cylinder. At large values of α, this phenomenon is also analogous to the heat transfer from an infinite slab at uniform temperature. The steady-state temperature must be constant everywhere since the line source in two-dimensions exhibits a logarithmic

singularity[1]. Since the velocity far from the orifice behaves as $v_r \sim 1/r$ for a slit orifice, where r is the radial distance from the orifice center, one can not obtain a finite pressure drop for two-dimensional flow. This implies that there is either an infinite pressure difference or finite boundaries need to be introduced in order to maintain the flow through the external media.

3.6 Biological Applications and Conclusion

The present paper is partially motivated by numerous experimental studies on the fenestral pathway for water and solutes in fenestrated capillaries. In this section, we will apply the results obtained from previous sections to estimate the hydraulic conductance of the fenestrated capillaries, with emphasis on the effects of different pathway structures, and also for the fenetrated pores in the internal elastic lamina of the artery wall.

Recent ultrastructural experimental observations indicate that a fibrous matrix coats the surface of a variety of cell membranes. In fenestrated capillaries, the total resistance of the fluid crossing the endothelium is due to three resistances in series, an overlying surface glycocalyx of 100-400nm thickness, which is composed of glycosyminoglycans (GAG) and core proteins as sketched in Fig. 3.2, followed in some cases by a very thin diaphragm of 5nm thickness and an underlying basement membrane which we shall assume is continuous with the subendothelial space, see Levick & Smaje (1987). Table 1 in Levick & Smaje indicates that the fenestral diameters for most tissues fall within the range 50–70nm. When considering a fenestrated endothelium of fractional area A_A, we assume that the pores are sufficiently far apart for their interaction to be neglected. This is a reasonable approximation for most fenestrated capillaries. Using the definition for L_p and Π in (3.4.4) and (3.4.5) for a pore in an infinite membrane, we obtain the following expression for the dimensional hydraulic permeability

$$L_p' = \frac{a}{\pi\mu}\Pi(\alpha_1, \alpha_2, L/a)^{-1} A_A. \tag{3.6.1}$$

[1]The authors thank professor A. Acrivos who pointed out this analogy.

Equation (3.6.1) is a linear function of fractional pore area A_A if the pore diameter $2a$ is small compared to the pore spacing and the interaction between pores is neglected.

It is generally believed that the fenestrated pores exclude albumin, 7nm diameter, but allow the passage of small solutes. Thus, we assume in applying equation (3.1.1) that the fiber radius, $r_f = 0.6$nm, and the fiber spacing, $\Delta = 7$nm. The corresponding value for α would be 11.3 for a typical orifice of 60nm diameter. If the thickness of the surface glycocalyx ranges from 100nm to 400nm, the present model predicts that the hydraulic resistance of the surface glycocalyx for a zero thickness pore, $1/L'_p = 0.0217\text{mmHg} \cdot \text{sec} \cdot \mu\text{m}^{-1}$, accounts for only 0.6–3% of the experimentally measured resistance. The experimental data are summarized in Table 1 of Levick & Smaje (1987) where results are given per unit area of fenestral pathway. Note that the present model predicts a lower resistance than that estimated in Levick & Smaje (1987). These investigators use a different fiber matrix model with a fiber fraction of 5 percent, which is much higher than the 1.7 percent used in our present model. Thus, a surface glycocalyx with properties postulated in the literature (Curry & Michel 1980) can create only a minor contribution to the measured fenestral resistance. This result implies that the fiber matrix either extends much deeper into the pore, or the matrix is highly inhomogeneous, if one is to account for the high measured resistance.

The structure, which in the past was regarded as the main fenestral barrier, is the densely stained diaphragm, whose thickness is only 5nm. This structure is compatible with the fibers in the diaphragm being the core proteins in the proteoglycans sketched in Fig. 3.2. A typical diameter of these proteins is about 4nm. The value for α for a diaphragm with fibers of this diameter for a 60nm orifice is 14.2 if $\Delta = 7$nm. The diaphragm, thus, contributes an additional resistance of only 0.02 $\text{mmHg} \cdot \text{sec} \cdot \mu\text{m}^{-1}$. If the measured resistance arises primarily from this diaphragm, then the fiber matrix model predicts a fiber spacing that is much smaller than the diameter of an albumin molecule, ~7nm. This is in contradiction with the observation that tracers of 3nm penetrate the fenestral pathway (Hart & Pino, 1985).

One possible resolution of the large discrepancy between the measured and predicted hydraulic conductances is to extend the length of the fenestral pore pathway as proposed by Levick & Smaje (1987), and assume that the glycocalyx and basement membrane have a specific permeability to water that is equal to that of the diaphragm itself. In order to fit the experimental data presented in Levick & Smaje (1987), one finds that the required length of a continuous matrix filled fenestral pore would need to be between 600nm and 3μm using results in Fig. 3.7, 3.8.

In contrast to the fenestral pores in capillaries, the interaction between adjacent pores plays an important role in determining the fenestral permeability of the internal elastic laminar (IEL) in the artery wall. According to Huang *et al.* (1998), the average of pore diameter $2a'$ is typically 2μm for the rat aortic wall, and these pores comprise approximately 5 percent of the *en face* area of the wall. These pore diameter measurements are not very sensitive to the transmural pressure. In comparison, a five-fold compression of the thickness of the intima was measured when the transmural pressure was increased from 0 to 150 mm Hg. We use an intimal thickness, $L_I' = 0.62\mu$m in our calculations. This corresponds to the measured thickness of rat aortic intima at zero transmural pressure. We consider a local, periodic wall unit surrounding a fenestral pore as illustrated in Fig 3.9. The size of the periodic unit cell is based on the measured density of fenestrae per unit IEL area. The filtration flow is due to the pressure difference across the entire artery wall, which includes both the intima and the media. Here we adopt a simplified model which captures the main features of the problem. We assume that the pressure at the pore opening is a constant, i.e., the average of the pressure over the pore opening. K_p for the intima, K_{pI}, is $>>$ K_p for the media, K_{pm}, as shown in Huang et al. (1994). However, for both regions $\alpha >> 1$ and the Darcy approximation is valid, as demonstrated in section 3.3. The total flux across the fenestral pore is

$$Q' = \frac{K_{pI}}{\mu}\frac{\Delta P_I'}{L_I'} S_I \cdot \pi \xi_I'^2 \tag{3.6.2}$$

where S_I is the shape factor representing the interaction of the periodic pores in the intima.

S_I can be obtained by solving the following mixed boundary value problem,

$$\nabla^2\phi = 0, \tag{3.6.3}$$

subject to

$$\frac{\partial\phi}{\partial r} = 0 \quad \text{at } r = 0, 1, \quad 0 \le z \le L_I \tag{3.6.4}$$

$$\phi = 1 \quad \text{at } z = L_I, \quad 0 \le r \le 1 \tag{3.6.5}$$

$$\phi = 0 \quad \text{at } z = 0, \quad 0 \le r \le a \tag{3.6.6}$$

$$\frac{\partial\phi}{\partial z} = 0 \quad \text{at } z = 0, \quad a \le r \le 1 \tag{3.6.7}$$

where the unprimed dimensions are normalized by the radius ξ_I' of the periodic unit. The shape factor S_I for the intima is given by (Davis & Ethier 1993) as

$$S_I = \left[1 + \frac{\pi}{4L_I \int_0^a h(t)dt}\right]^{-1} \tag{3.6.8}$$

in which $h(t)$ is obtained by solving the following integral equation,

$$\begin{aligned} h(t) \quad - \quad & \frac{4}{\pi}\int_0^a h(u)\left\{\sum_{n=1}^{\infty}\frac{\cos\lambda_n t\cos\lambda_n u}{\lambda_n[J_0(\lambda_n)]^2}(1-\tanh\lambda_n L_I)\right. \\ + \quad & \left. 1 + \frac{1}{\pi}\int_0^{\infty} K_1(y)\left[\frac{2}{y} - \frac{\cosh ty\cosh uy}{I_1(y)}\right]dy\right\}du = 1, \end{aligned} \tag{3.6.9}$$

where λ_n are the ascending positive roots of $J_1(x) = 0$.

A similarly expression to (3.6.2) can be written for the flux across the pore opening into the media,

$$Q' = \frac{K_{pm}}{\mu}\frac{\Delta P_m'}{L_m'}S_m \cdot \pi\xi_I'^2. \tag{3.6.10}$$

Here S_m is the shape factor for the media, which is obtained by applying results (3.6.9) and (3.6.10) in the media, and L_m' is the media thickness.

The dimensional filtration coefficient is given by

$$L'_{p,j} = \frac{Q'}{\pi \xi_I^2 \Delta P'} = \frac{K_{p,j}}{\mu} \frac{S_j}{L'_j}, \quad \text{j=I, m.} \tag{3.6.11}$$

The variation of the function S_j/L_j, is presented in Fig. 3.10 with respect to either the fractional pore area A_A, or the dimensionless medium thickness $L_j = L'_j/\xi'_I$. Four sets of results are presented. $L_j = 0.14$ describes the relaxed rat intima, where $L'_I = 0.62\mu$m. $L_j = 22.4$ and 44.7 correspond to the rat and rabbit media, respectively, where $L'_m = 100$ and 200μm in that order. $L_j = 1$ shows the transition from small to large values of L_j. Also shown in Fig 3.10(a) (circles) is the asymptotic result (3.2.38) for an orifice in a semi-infinite medium obtained in section 3.2. The latter result is valid for fractional pore areas up to 40 percent when L'_j/ξ'_I is of $O(1)$. For $L'_j/\xi'_I > O(1)$ one needs to consider the resistance due to the thickness of the media and for $L'_j/\xi'_I < O(1)$ the layer thickness is not sufficient for the flow to be approximated by a semi-infinite medium.

When $L'_j/\xi'_I >> 1$, one can derive a simple expression for S_j/L_j from the integral equation (3.6.9). This leads to the following expression for S_j/L_j

$$\frac{S_j}{L_j} = \frac{1}{L_j + \gamma(A_A)} \tag{3.6.12}$$

in which γ is a function of only the fractional pore area. The numerical solution for γ is determined by solving the reduced integral equation

$$h(t) - \frac{4}{\pi} \int_0^a h(u) \left\{ 1 + \frac{1}{\pi} \int_0^\infty K_1(y) \left[\frac{2}{y} - \frac{\cosh ty \cosh uy}{I_1(y)} \right] dy \right\} dy = 1. \tag{3.6.13}$$

Based on arguments similar to those presented in section 3.4 for flow through a finite length pore, one can separate the flow across the media into two regions, a near field and a far field. In the proximity of the pore, the near field, where the resistance arises primarily from the spreading of the orifice flow for large α, the solution is given by (3.2.38). Away from the pore, the flow is basically a uniform plug flow. The total resistance is the summation of

both these contributions. When $L_j >> 1$, the transition from a flow through a semi-infinite medium to a uniform Darcy flow occurs over a region in which $L_j = O(1)$. Applying a procedure similar to that for flow through a finite length pore, one obtains

$$\gamma(A_A) = \frac{\pi}{4\sqrt{A_A}} - 1 \tag{3.6.14}$$

Comparison between the numerical solution of (3.6.13) and the simple approximate result (3.6.14) is given in table 3.1. This close agreement for $L_j \geq 1$ is shown by the results in Fig. 3.10(b).

By equating Q' in (3.6.2) and (3.6.10), one obtains a simple formula for the relationship between S_m/L_m and S_I/L_I

$$\frac{S_m}{L_m} = \frac{\alpha_m^2}{\alpha_I^2}\frac{S_I}{L_I}, \tag{3.6.15}$$

Huang *et al.* (1994,1997) provide typical values for fiber structures in the intima. They suggest a proteoglycan fiber radius r_{PG} of 2nm and a fiber spacing, Δ_{PG}, of 30-40nm, embedded in a collagen matrix where $r_{CG} = 20$nm and $\Delta_{CG} = 120$nm. We shall treat the presence of the collogen separately from that of the proteoglycans and assume, after Levick (1987), that the resistances due to these two populations of fibers simply sum, i. e.

$$\frac{1}{K_{pI}} = \frac{1}{K_{p(CG)}} + \frac{1}{K_{p(PG)}}. \tag{3.6.16}$$

Using the approximate formula (3.1.1), one estimates the hydraulic permeability parameter α_I of the intima to be about 60. This is far less than the measured value for the media, $\alpha_m = 300$. S_m/L_m is thus 25 times that of the intima and the intimal resistance can be neglected unless the intima is highly compressed and α_I increases.

In summary, the present paper presents the first solutions for the pressure-driven flow through a circular orifice in a plane wall embedded in a Brinkman medium. We have also extend the model to account for finite pore length by using a procedure similar to that employed by Dagan *et al.* (1982) for Stokes flow. The close relationship of this flow to the

broadside translation of a disk is revealed. As a result of Stokes paradox for the flow past an infinite cylinder, there is no solution for the pressure-driven flow through a two-dimensional slit for a Brinkman medium. The model is used to elucidate the relative importance of fiber-matrix, the fenestral diaphragm and pore length in flow through fenestral pores in several biological applications.

A_A	numerical	approximation
0.4%	10.66	11.41
1%	6.750	6.850
5%	2.418	2.511
10%	1.404	1.482

Table 3.1: Comparison of γ obtained by numerical solution of equation (3.6.13) and approximate formula (3.6.14).

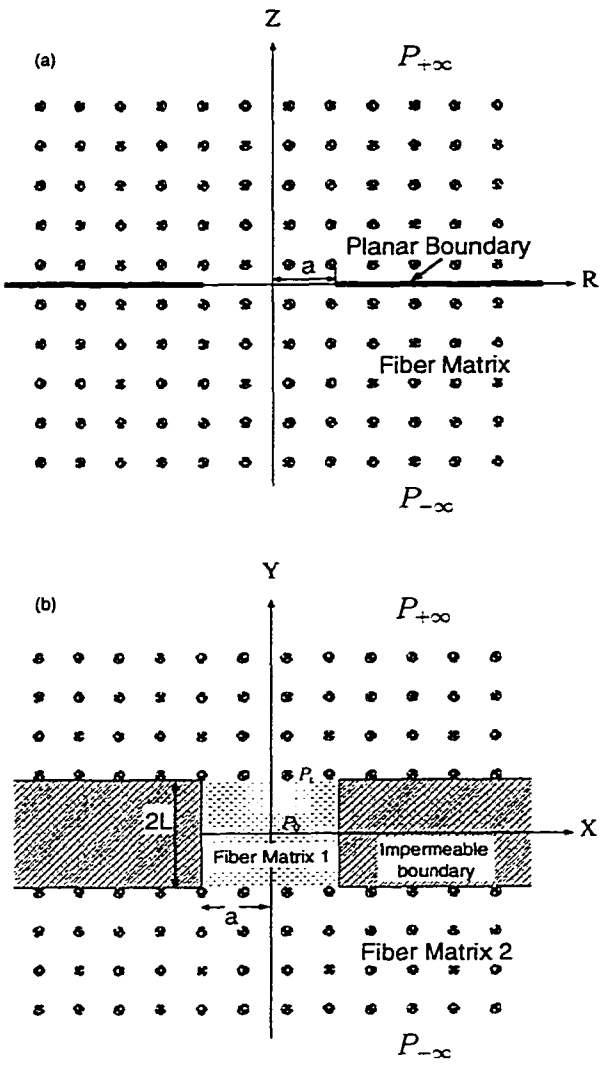

Figure 3.1: Geometries of the model (a): Flow through a circular/slit orifice of zero thickness; (b): Flow through a circular/slit pore of finite length $2L$.

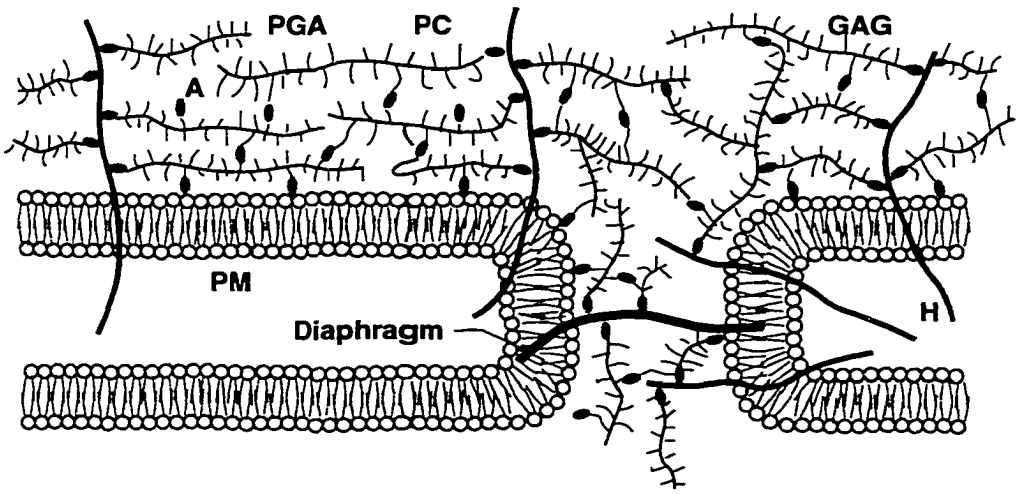

Figure 3.2: Schematic illustration of a long chain proteoglycan matrix at the opening of an orifice-like pore in a fenestrated capillary. PM, plasma membrane; PGA, proteoglycan aggregate, PC, protein core arranged along hyaluronic acid backbone H. Primary hydraulic resistance derives from GAG side chains (length not shown to scale) which are periodically spaced along protein core (PC).

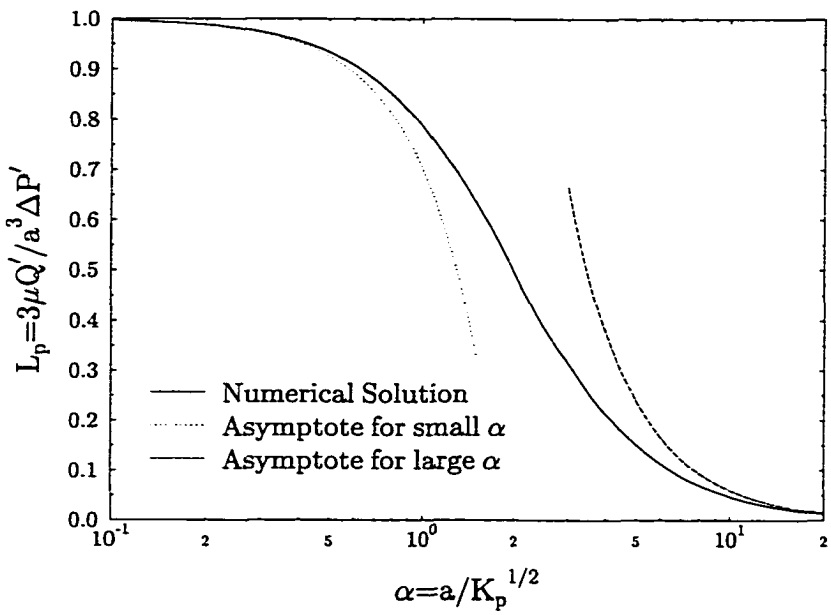

Figure 3.3: Dimensionless hydraulic permeability of pressure driven flow through a circular orifice in a plane wall in a fibrous medium.

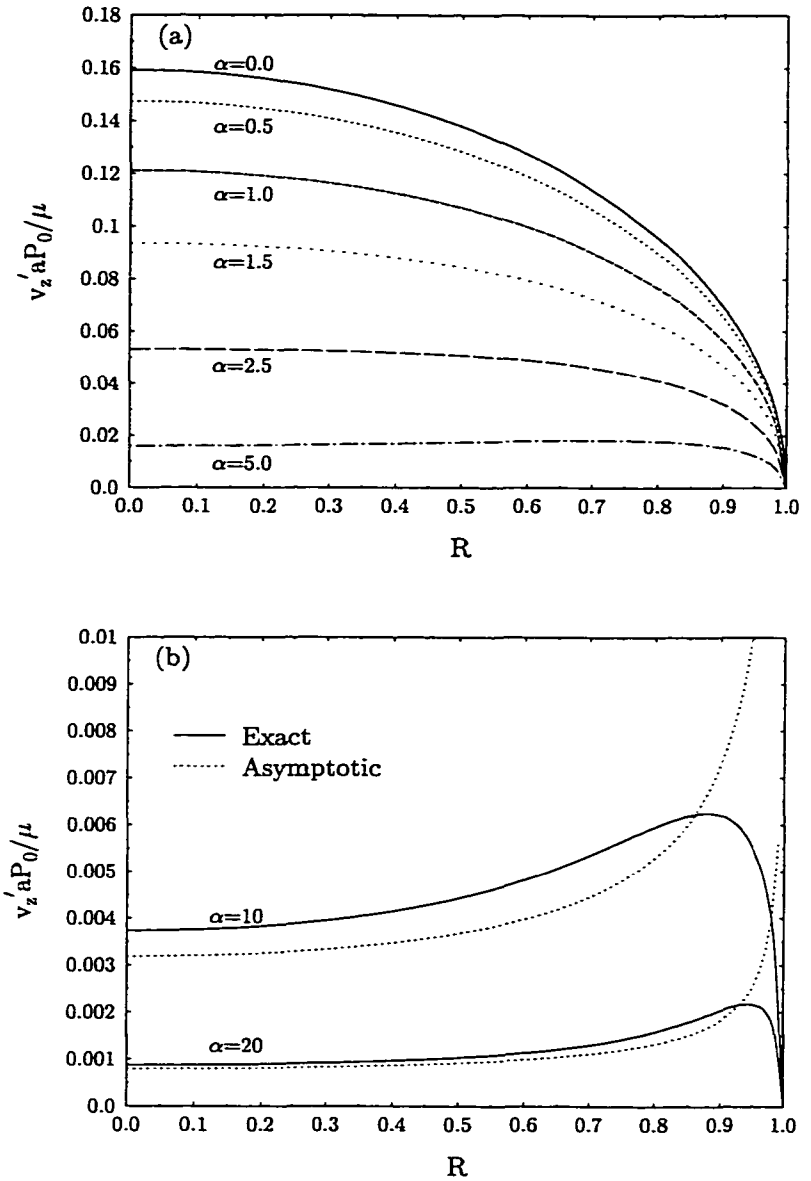

Figure 3.4: Dimensionless axial velocity profiles at the orifice opening.

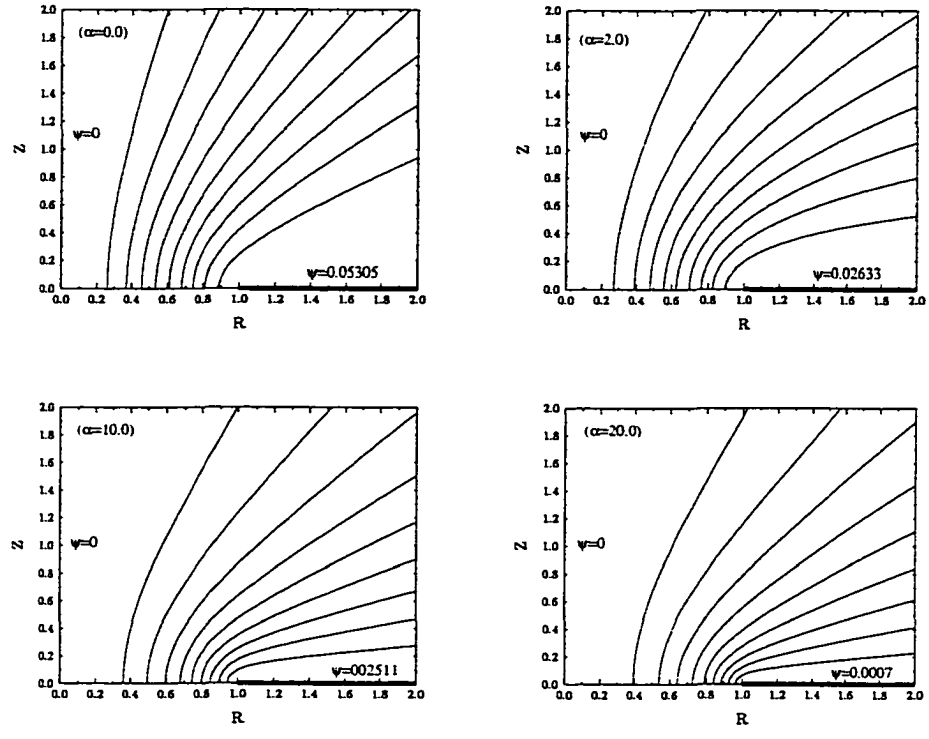

Figure 3.5: Flow patterns for $\alpha = 0$, 2, 10 and 20. The streamlines for different α are in equal increments from zero to the value on the wall.

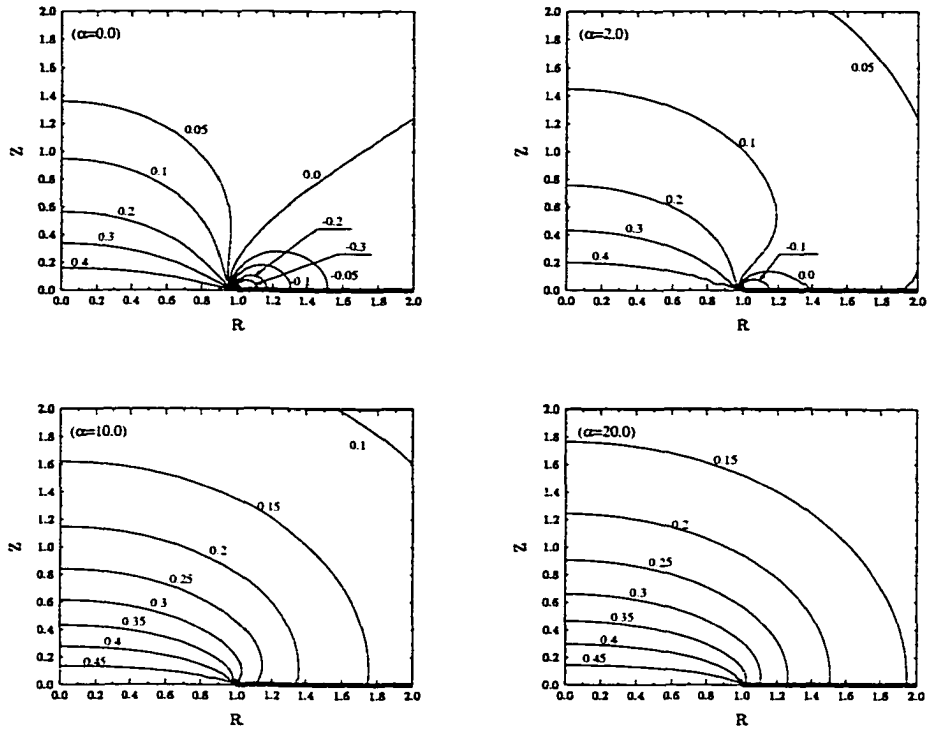

Figure 3.6: Pressure fields (isobars) for $\alpha = 0$, 2, 10 and 20.

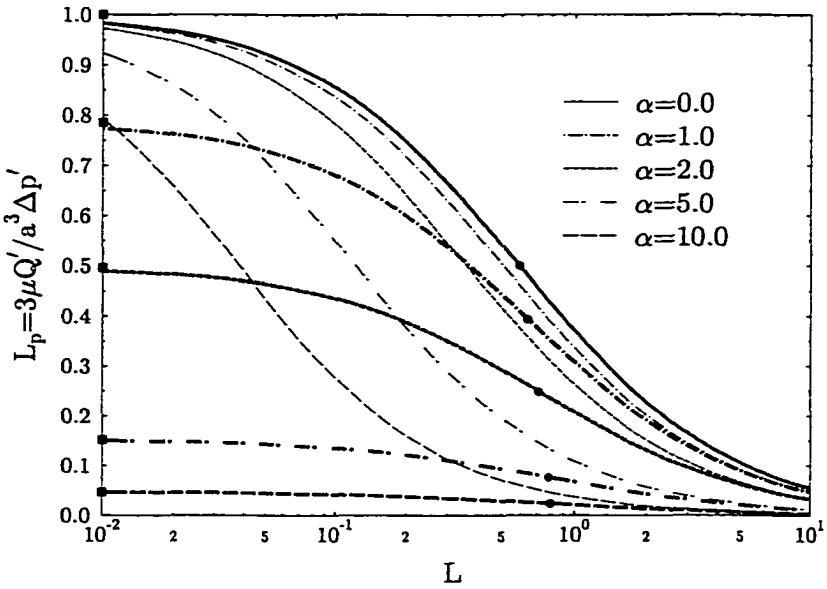

Figure 3.7: Dimensionless hydraulic permeability of pressure driven flow through a circular pore of finite length in a plane wall. Thick curves describe the case where $\alpha_1 = \alpha_2$; thin curves describe the case where $\alpha_1 = \alpha$ and $\alpha_2 = 0$, no external matrix. Square symbols value of L_p for zero thickness orifice. Circular symbols value of L for which resistance of entrance and exit flow is just equal to interior of pore.

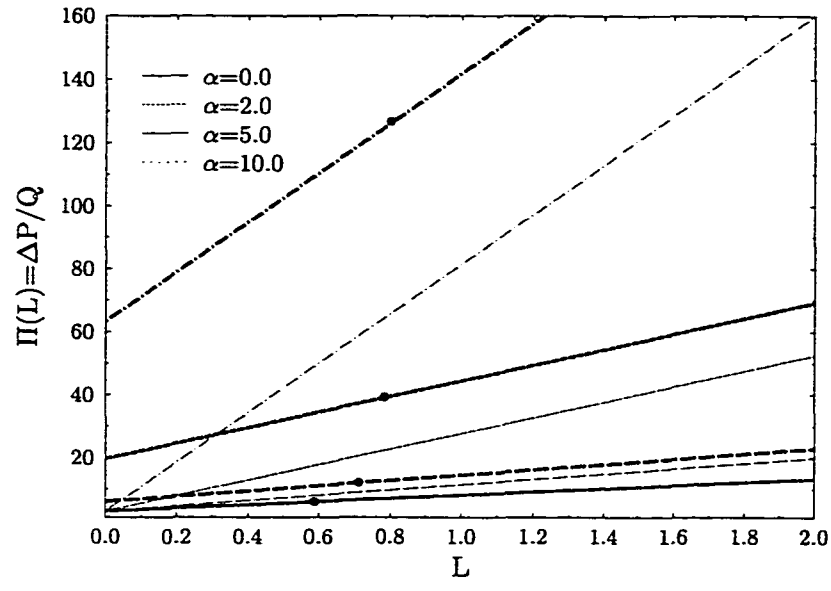

Figure 3.8: Hydraulic resistance function Π defined by equation (3.4.5) as a function of pore length. Thick curves describe a continuous matrix where $\alpha_1 = \alpha_2$, thin curves describe the case where $\alpha_1 = \alpha$ and $\alpha_2 = 0$, no external matrix. Circular symbols value of L for which the resistance of pore interior is just equal to entrance and exit.

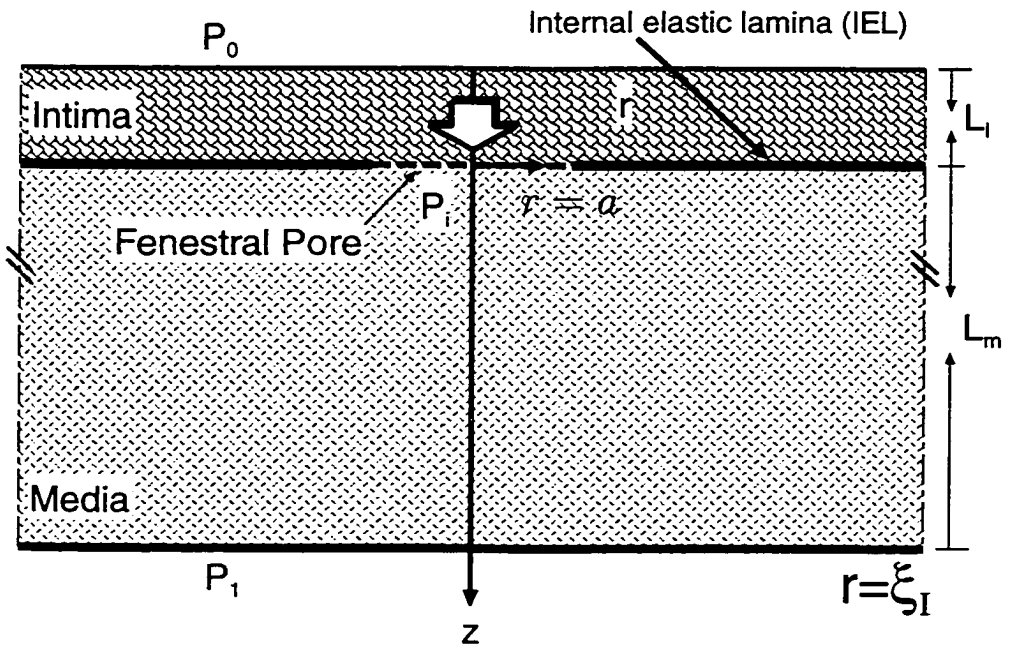

Figure 3.9: Schematic illustration of local, periodic wall unit around a fenestral pore for filtration flow through internal elastic lamina.

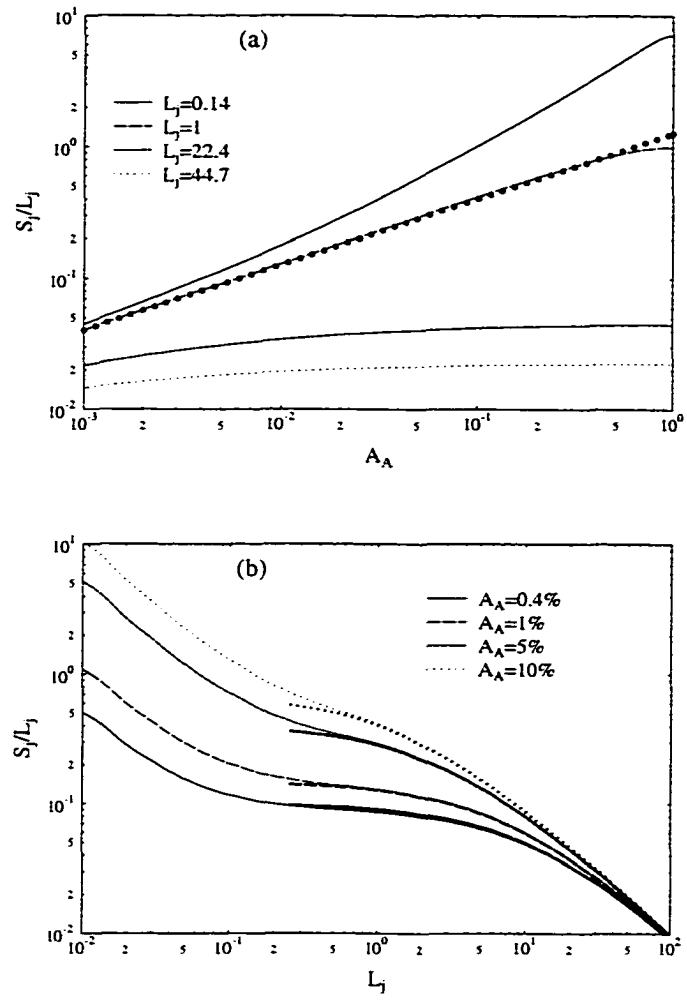

Figure 3.10: The variation of the function S_j/L_j with respect to either the pore fractional area A_A (a) or the dimensionless medium thickness L_j (b). The circles in (a) represent the solution for an orifice in a semi-infinite medium. The thick curves in (b) are obtained from the simple approximate solution (3.6.14).

Chapter 4 Motion of a Sphere Near Planar Confining Boundaries in a Brinkman Medium

4.1 Introduction

The motion of a particle in a porous material adjacent to confining boundaries is of interest most notably in the areas of chemical and biomedical engineering and the biophysics of membranes. The motivation for the present study stems from several recent developments in the study of thin surface layers of matrix that coat the membranes of living cells, Weinbaum (1998). Of particular interest is the thin polyelectrolyte layer of loose fibers that form the surface glycocalyx, literally "sugar coat", of endothelial cells and the possible extension of this matrix into the interendothelial clefts, the 20nm wide extracellular channel between endothelial cells through which water and solutes cross the capillary wall (Weinbaum *et al.* 1992; Fu *et al.* 1994). This surface glycocalyx, which has been estimated to be from 100nm (Adamson & Clough 1992) to 400nm thick (Vink & Duling 1996) using electron and fluorescence microscopy, is the principal sieving layer for plasma proteins that determines the colloidal osmotic force across the capillary wall. This surface coat is also thought to play a major role in receptor-ligand interactions between the tips of microvilli in the rolling interaction of neutrophils on the endothelial surface (Bruehl *et al.* 1996; Alon *et al.* 1997) and single particle tracking (SPT) experiments where 20 to 40nm colloidal gold and larger latex and polystyrene beads up to 200nm diameter are attached to membrane receptor molecules and observed in nanovid (video enhanced) microscopy. The latter experiments have been used to estimate pericellular matrix viscosity, Lee *et al.* (1993), to explore the surface dynamics of transmembrane integrins in migrating fibroblasts (Schmidts *et al.* 1993), to elucidate the structure of the submembrane actin cytoskeleton (Sako & Kusumi 1995) and to study the movement of cell-cell adhesion molecules (Sako *et al.* 1998) to mention just a few of the numerous studies in this rapidly growing field. In many of these studies,

picoNewton forces generated by optical gradient traps (laser tweezers) are used to drag gold and latex tagged membrane proteins laterally in the plane of the membrane against the combined resistance of the cytoskeleton, the membrane lipid and the extracellular matrix.

In this paper an effective medium theory based on the Brinkman equation will be developed to examine the motion of particles in a porous medium in the presence of one or more confining boundaries. In particular, we shall be interested in (1) the perpendicular motion of a sphere near a fiber coated planar wall as a simple idealized model for calculating the hydrodynamic interaction of a microvilli tip with the endothelial surface glycocalyx, (2) the translational motion of a sphere parallel to a fiber coated planar wall as a model for calculating the hydrodynamic resistance of the gold and latex particles in the surface glycocalyx or the lateral diffusion of a solute molecule in the layer, and (3) the motion of a sphere in a fiber-filled channel as a model for solutes diffusing through the interendothelial cleft. The latter model is also of interest in investigating the transport of lipoproteins in the thin layer of intimal matrix between the endothelial cells and the internal elastic lamina of arteries and the growth of cellular level macromolecular leakage spots (Huang *et al.* 1994). In the problems involving molecular diffusion we shall assume that the diffusing molecule is smaller than the gap between the matrix fibers, which is taken to be 7nm, the effective diameter of albumin, the most abundant plasma protein. As we shall discuss shortly, this will place a constraint on the maximum value of the permeability parameter α that appears in the Brinkman equation. For problems involving gold and latex tracer particles this estimated fiber spacing will be 3 to 30 times smaller than the test sphere that is dragged through the surface matrix. In this case one must also consider the elastic and binding energy stored in the fibers. A rough estimate of the relative magnitude of the hydrodynamic and these other effects can be obtained by calculating the hydrodynamic resistance due to the fibers and subtracting it from the total drag on the particles estimated from their diffusional mobility.

The Brinkman (1947) equation has been widely used in calculating the hydrodynamic interaction and hindered transport of solid spherical particles in ordered or disordered fibrous media. Since the Brinkman equation has only one additional parameter, K_p, which

characterizes the permeability of the porous media, one does not have to have a knowledge of the detailed structure of the porous media once the permeability has been determined either by theoretical prediction or experimental measurement. When the equation is scaled by the particle radius r_s and made dimensionless a single parameter, $\alpha = r_s/\sqrt{K_p}$, appears. α describes the ratio of the particle dimension to the fiber interaction layer thickness, $\sqrt{K_p}$. K_p in turn depends on the fiber spacing Δ and to a lesser extent on the fiber radius a. The analysis in Tsay & Weinbaum (1991) shows that $\sqrt{K_p}$ is of the same order as the fiber spacing Δ.

A central issue in using the Brinkman equation to describe the drag and torque exerted on a diffusing particle is the limitation on α for which the effective medium theory applies. This parameter describes the transition from small-scale viscous motion described by the Stokes equation to larger-scale pressure driven motions governed by Darcy's law. To address this question, Durlofsky & Brady (1987) first compared the Green's function (point force) for the Brinkman equation with the solution for a point force using a Stokesian dynamic simulation for a point force in a periodic particle array. It was found that the Green's function in effective medium theory accurately describes the Stokes flow in the near field and the dipole flow in the far field provided the solid fraction is less than 5 percent. Phillips *et al.* (1989, 1990) subsequently employed a Stokesian dynamic simulation in which they represented the fibers as either parallel strands of spherical beads or cylinders and examined the motion of a test sphere relative to an ordered strand array. They concluded that in the low fiber fraction limit, the far field interaction between the mobile particle and the fibers dominates the contribution arising from the local inhomogeneity of the medium due to the existence of the particle. The effective medium theory was most accurate in the dilute fiber limit, fiber fraction less than 5 percent, where the value of α was less than $O(1)$ and the particle was small compared to the fiber spacing. They also found that the diffusivity calculated from the Brinkman equation agrees quite well with that obtained by the more rigorous Stokesian dynamic method, provided steric effects are included. The same conclusion is reached in Fig. 4.10 of the present study, where we demonstrate using

the steric exclusion theory in Tsay & Weinbaum (1991) for a periodic fiber array, that good agreement can be obtained with Stokesian dynamic simulations when the fiber fraction is ≤ 0.1. Experimental results for the diffusivity of a macromolecule in a fibrous gel also indicate that the Brinkman equation is a good model, in particular for a medium with low fiber volume fraction (Johnson *et al.* 1996). Moreover, Kosar & Phillips (1995) have shown that the Brinkman model for describing screened hydrodynamic interactions gives results equivalent to models of the Kirkwood-Riseman type, in which the effects of the fixed fibers are modeled using a distribution of immobile point forces. All of the aforementioned work seems to support the contention that the application of the Brinkman medium model may be limited more by an inadequate knowledge of the actual microstructure than by any inherent limitations in the effective medium approach when the fiber fraction is small.

In the past, several investigators have attempted to derive the Brinkman equation using various models for Stokes flow in unbounded porous media. Tam (1969) averaged the Stokes equation governing slow viscous flow past a cloud of spherical particles. This approach led to a Brinkman equation and thus provided a more rigorous theoretical basis for its application. The uncertainty in the definition of the viscosity in the Brinkman equation in Tam's method was examined more thoroughly by Lundgren (1972), who extended Tam's method to both stationary beds and suspensions of particles. Howells (1974) developed an iterative scheme for obtaining the average drag for flow through random arrays of either spheres or parallel circular posts at small solid fraction. More recently, the Brinkman equation has also been examined for flow in a bounded medium comprised of a perpendicular periodic array of circular cylindrical fibers in a parallel walled channel (Tsay *et al.* 1991). It was shown that very good agreement with the Stokes solution for the flow through the fibers in the channel could be obtained by solving the Brinkman equation for all values of $\alpha = h/\sqrt{K_p}$, where h is here the channel height, provided that the aspect ratio of the fibers was greater than five. Furthermore, good agreement for the drag could be obtained for all fiber volume fractions when K_p was described by its expression for a two-dimensional unbounded fiber array.

Although various solution techniques have been developed for treating the motion of

a sphere in Stokes flow in the presence of boundaries, there are no prior solutions to the Brinkman equation for the motion of a sphere in a bounded medium. The general solution of the Brinkman equation involves three scalar functions obtained by solving a Laplace equation and two modified Helmholtz equations (Kim & Russel 1985a). These solutions are analogous to the harmonic functions for creeping flow. Since the Helmholtz equation admits fewer separable solutions than Laplace equation in various orthogonal coordinate systems, such as bipolar and toroidal coordinates, solutions for the hydrodynamic interaction between particles or a particle and confining boundaries in a Brinkman medium are very limited. One solution of the Brinkman equation of particular interest in evaluating the accuracy of the numerical solution technique developed herein is the interaction between two spherical particles. This problem was investigated by Kim & Russel (1985a) to determine the effect of pair interactions on the effective permeability and viscosity of an array of fixed particles (Kim & Russel 1985b). These authors used the method of reflections for weak interactions in which the particles were far removed from each other, or the boundary collocation technique of Gluckman *et al.* (1971) for strong interactions in which the clearance between the particles was comparable to their diameter.

The boundary integral equation method has been widely used in creeping flow problems since it was first introduced by Youngren & Acrivos (1975). This numerical method is computationally efficient and flexible in treating both rigid and deformable flow geometries. Great progress has been made over the past twenty years in improving its accuracy and reducing computational efforts, especially in the special treatment of the singular integral which arises in the calculation of the contribution from the element containing the collocation point and in reducing the dimensions of the problem for special flow configurations. In addition to the traditional formulation, in which one reduces the flow problem to solving a system of Fredholm integral equations of the first kind for the surface traction defined on the surfaces of all boundaries in the flow field, alternative formulations leading to integral equations of the second kind have also been developed to treat multiple particles. Green's functions that satisfy the no-slip boundary conditions on infinite boundaries, have also been

used to obtain several Stokes solutions for the motion of spheres, spheroids and slender objects moving near walls (Weinbaum *et al.* 1991). These fundamental solutions for bounded flow are available for only a few flow geometries. No such Green's functions are known for the Brinkman equation.

In contrast to Stokes flows, where the drag on a particle is the same whether the particle is moving in a stationary fluid at infinity or there is a uniform flow past a stationary particle, in a Brinkman medium these two solutions are not interchangeable since for a uniform flow there is a finite pressure gradient at infinity described by the Darcy resistance. This gives rise to a term which is proportional to the volume of the particle. The second fundamental difference is that the Darcy permeability K_p is a function of the fiber spacing and fiber radius, and not all values of K_p are permissible unless the fibers are highly flexible. A sphere of radius r_s will not be able to translate in a rigid periodic fiber array when the open spacing between fibers, Δ, is less than the sphere diameter. Thus for a rigid fiber array, the Brinkman parameter $\alpha = r_s/\sqrt{K_p}$ describing the motion of a spherical particle in a Brinkman medium will have a maximum value if the particle is not to be trapped by the fibers. For a periodic fiber array one must satisfy a complementary constraint on K_p that $\Delta > 2r_s$. Curiously, this fundamental constraint does not appear to have been examined previously in the literature. For a spherical particle diffusing in a rigid fiber array, we shall show that this maximum value of α is approximately 1.5 and varies weakly with the fiber radius. This limitation on α will not apply if a large particle is forcibly moved through a highly flexible matrix with weak fiber adhesion energy. This would appear to be the case when a large tracer particle is dragged by optical tweezers through a surface glycocalyx or when a microvilli on a white cell penetrates this surface layer. In these applications our theory only describes the hydrodynamic resistance of these motions and not the elastic and adhesion energy of the fibers. α in these applications can be $O(10)$ or larger.

In the present work, we shall take advantage of the axisymmetry of the boundaries using a technique developed by Pozrikidis (1994) for Stokes flows. This allows us to decompose all the flow variables into a complex Fourier series with respect to the common azimuthal

angle. The original three dimensional integral equation is thereby reduced to a set of one-dimensional integral equations defined on the contours of the boundaries. Further simplification is achieved by considering the fact that only the first order harmonics need be retained for translation and the corresponding double layer contribution can be evaluated analytically. A standard boundary collocation technique is used to discretize the boundary contours into small segments. By using a numerical technique that can accurately calculate the singular integrals, we can also apply our method to flows in porous media of small permeability, $\alpha \gg 1$. This removes a technical difficulty of the boundary integral equation method for flows governed by the Brinkman equation, or the mathematically equivalent unsteady creeping flow equations (Pozrikidis 1988, Loewenberg 1994).

The method is then used to calculate the drag and torque coefficients for a sphere translating in a fibrous medium in a channel. These solutions illustrate the relative importance of shielding by the walls compared to shielding by the fibers. The solutions are then used as input into a Stokes-Einstein model for determining the diffusion coefficient for a spherical particle in a fiber-filled channel. A new hydrodynamic theory for determining the approximate diffusive permeability of a spherical molecule in an inter-endothelial cleft, our initial motivation for this work, is presented as an application of the numerical results. The theory also takes steric exclusion into consideration. Comparison with a previously obtained simple multiplicative formula for the diffusive permeability in which the effects of the fiber matrix and the walls were treated separately (Weinbaum *et al.* 1992) reveals that the earlier approximate method provides an underestimation of the diffusive permeability. A brief discussion of the present method and further applications in creeping flows conclude the paper.

4.2 Boundary Integral Equation for Flow in a Brinkman Medium

The Brinkman (1947) equation,

$$\nabla p = \mu \nabla^2 \mathbf{v} - \frac{\mu}{K_p} \mathbf{v}, \tag{4.2.1}$$

together with the continuity equation for an incompressible viscous fluid,

$$\nabla \cdot \mathbf{v} = 0. \tag{4.2.2}$$

are often used to describe flows in porous media in which the pressure gradient, velocity gradient and Darcy resistance are of comparable importance. As previously noted by Kim & Russel (1985a), the solution of equation (4.2.1) for the velocity field can be expressed by three scalar functions which satisfy Laplace's equation and two Helmholtz equations. However, the Helmholtz equation does not permit solutions by separation of variables in bispherical coordinates. This makes it difficult to study the motion of a sphere in the proximity of an infinite wall. In this section, a general boundary integral equation method will be formulated in order to investigate bounded flow problems such as particle motion near a planar boundary or between two parallel walls. The complexity of the resulting integral equations usually precludes analytical solution so that solutions must be obtained by numerical methods. A simple effective and flexible collocation boundary element discretization procedure will be introduced.

We first consider an arbitrary three-dimensional flow problem governed by the Brinkman equation and the continuity equation. Following a procedure similar to that used by Pozrikidis (1994) in treating creeping flow, we write the reciprocal relationship

$$\nabla \cdot (\mathbf{u}^* \cdot \sigma - \mathbf{u} \cdot \sigma^*) = 0, \tag{4.2.3}$$

in which $\mathbf{u}$ and $\mathbf{u}^*$ are any two solutions to the system (4.2.1) and (4.2.2), with corresponding

stress fields σ and σ^* at the given point $\mathbf{x}$.

The Green's function for the Brinkman equation corresponding to the Stokeslet for the creeping flow is given by

$$S_{ij}(\mathbf{x}) = \frac{\delta_{ij}}{r}A + \frac{\hat{x}_i\hat{x}_j}{r^3}B, \tag{4.2.4}$$

where

$$A = 2e^{-\alpha r}\left(1 + \frac{1}{\alpha r} + \frac{1}{\alpha^2 r^2}\right) - \frac{2}{\alpha^2 r^2}, \tag{4.2.5}$$

$$B = -2e^{-\alpha r}\left(1 + \frac{3}{\alpha r} + \frac{3}{\alpha^2 r^2}\right) + \frac{6}{\alpha^2 r^2}, \tag{4.2.6}$$

and the associated stress tensor is given by

$$T_{ijk} = \left[\frac{\partial S_{ij}}{\partial \hat{x}_k} + \frac{\partial S_{kj}}{\partial \hat{x}_i}\right] - 2\delta_{ik}\frac{\hat{x}_j}{r^3}. \tag{4.2.7}$$

Here $\hat{\mathbf{x}} = \mathbf{x} - \mathbf{x}_0$, $r = |\hat{\mathbf{x}}|$, and δ_{ij} is the Kronecker tensor. Now we select a point $\mathbf{x}_0$ in the flow domain and integrate the reciprocal relation between the desired solution and above singular solution over the entire control volume composed of the particles, a virtual sphere of infinite radius and a small sphere centered at the singular point. Using the divergence theorem in conjunction with the asymptotic properties of the singular solutions at infinity, and applying the result of a point on the surface of arbitrary solid boundaries, one can express the velocity field in terms of a boundary integral equation

$$u_j(\mathbf{x}_0) = -\frac{1}{4\pi\mu}\int_{S_p}[f_i(\mathbf{x})S_{ij}(\hat{\mathbf{x}}) - u_i(\mathbf{x})T_{ijk}(\hat{\mathbf{x}})\mathbf{n}_k(\mathbf{x})]dS(\mathbf{x}), \tag{4.2.8}$$

where $\mathbf{f} = \sigma\cdot\mathbf{n}$, S_p denotes the entire boundary including the particle surfaces, with $\mathbf{n}$ being the unit normal vector pointing into the fluid.

Equation (4.2.8) is applicable to particle motion in a Brinkman medium with or without any other confining boundaries. In deriving this equation, we have assumed that the velocity decays at infinity at a sufficiently fast rate. Otherwise, it must be applied to an appropriately chosen disturbance flow field which satisfies asymptotically decaying condi-

tions. For example, for uniform pressure-driven flow in an otherwise quiescent Brinkman medium, we can separate the contribution to the total velocity into the flow at infinity plus the integral in (4.2.8)

$$u_j(\mathbf{x}_0) = u_{j\infty}(\mathbf{x}) - \frac{1}{4\pi\mu}\int_{S_p}[f_i(\mathbf{x})S_{ij}(\hat{\mathbf{x}}) - u_i(\mathbf{x})T_{ijk}(\hat{\mathbf{x}})\mathbf{n}_k(\mathbf{x})]dS(\mathbf{x}). \tag{4.2.9}$$

To this end, we have reduced the problem to an boundary integral equation defined on the surfaces of the boundaries. For a flow problem that involves only the translation of the particle, the second term in the integral in equation (4.2.8) can be calculated explicitly, i.e., if we define the modified surface traction as $\mathbf{f} = \mathbf{f}' + \alpha^2(\mathbf{v}\cdot\mathbf{x})\mathbf{n}$, then $\mathbf{f}'$ satisfies

$$u_j(\mathbf{x}_0) = -\frac{1}{8\pi\mu}\int_{S_p} f_i'(\mathbf{x})S_{ij}(\hat{\mathbf{x}})dS(\mathbf{x}). \tag{4.2.10}$$

The total force exerted by the fluid on the particle can be obtained by integrating the surface traction over the entire particle surface. This leads to

$$\int_{S_p}\mathbf{f}ds = \int_{S_p}\mathbf{f}'ds + \alpha^2\mathbf{v}V_p \tag{4.2.11}$$

in which V_p is the volume of the particle.

For uniform flow past stationary particles, it can be verified that $\mathbf{f}$ in equation (4.2.9) is equal to the total surface traction. It does not seem possible to eliminate the associated stress field in (4.2.8) or (4.2.10) for the general motion of the particle or for non-uniform upstream flows, as was done by Kim & Karrila (1991) in the creeping flow limit. This difficulty prevents us from obtaining solutions for the rotation of the sphere. Once the integral equations (4.2.8) or (4.2.10) are solved for $\mathbf{f}$ or $\mathbf{f}'$, respectively, the net force and torque exerted on the particle can be readily calculated by integrating $\mathbf{f}$ or $\mathbf{f}'$ over the entire surface. Starting from the integral equation (4.2.8), several asymptotic solutions for large or small values of the parameter α can be obtained for the oscillation of a single particle in Stokes flow (Pozrikidis 1988, Loewenberg 1994). These asymptotic solutions can also be

applied to the Brinkman equation.

At this point, we focus our attention on a large class of flow problems that are bounded by axisymmetric surfaces, i.e., boundaries generated by rotating the contours about a common x axis in the cylindrical coordinates (σ, ϕ, x) as illustrated by figure 4.1. It can be shown that for flows parallel to this axis, the surface traction is a *zeroth* order harmonic function independent of the azimuthal angle. For the flows perpendicular to this axis, the surface traction is a *first* order harmonic function of the azimuthal angle ϕ (Ganatos *et al.* 1980b, Hsu & Ganatos 1991). A more detailed discussion of this issue can be found in Pozrikidis (1992, 1994) for more general axisymmetric boundary conditions.

Now consider a sphere moving parallel to the axis of rotation in an axisymmetric domain, figure 4.1a. In this case, one may perform the integration in the azimuthal direction to reduce the surface integral into a line integral on the contour of each particle and the confining boundaries in a meridional plane. For translational motion of a sphere, the resulting equation will be as follows

$$u_f(\mathbf{x}_0) = -\frac{1}{8\pi\mu} \sum_i \int_{C_{pi}} \Psi_{fg}(\mathbf{x}, \mathbf{x}_0) f'_g(\mathbf{x}) \sigma dl(\mathbf{x}), \tag{4.2.12}$$

where the matrix Ψ is defined as

$$\begin{bmatrix} A_{10} + \hat{x}^2 B_{30} & \hat{x}(\sigma B_{30} - \sigma_0 B_{31}) \\ \hat{x}(\sigma B_{31} - \sigma_0 B_{30}) & A_{11} + (\sigma^2 + \sigma_0^2) B_{31} - \sigma\sigma_0 (B_{30} + B_{32}) \end{bmatrix} \tag{4.2.13}$$

in which

$$A_{mn} = \int_0^{2\pi} \frac{\cos^n \phi}{r^m} A d\phi, \qquad B_{mn} = \int_0^{2\pi} \frac{\cos^n \phi}{r^m} B d\phi. \tag{4.2.14}$$

Once the surface traction $\mathbf{f}$ has been determined from equation (4.2.12), the drag on the sphere can be obtained by (4.2.11).

We next consider the motion of a sphere perpendicular to the axis of an axisymmetric domain of the Brinkman medium, figure 4.1b. We introduce the cylindrical coordinate

system (σ, ϕ, x), decompose the polar cylindrical components of the velocity and surface traction into complex Fourier series with respect to the azimuthal angle, express the integral equation (4.2.8) or (4.2.10) also in a complex Fourier series and equate the corresponding components of the boundary conditions of the same order. The linearity of the Fourier series leads to a system of equations relating the Fourier coefficients of the velocity to the boundary surface force. For a sphere translating with the velocity U_0 which is first order harmonic dependent upon the azimuthal angle, in the form

$$U_{0x} = U_x \cos\phi, \quad U_{0\sigma} = U_\sigma \cos\phi, \quad U_{0\phi} = -U_\phi \sin\phi, \tag{4.2.15}$$

the Fourier components are $(U_x, U_\sigma, U_\phi) = (0, U_0, U_0)$, whereas for a uniform flow U^∞, these components are $(U_x^\infty, U_\sigma^\infty, U_\phi^\infty) = (0, U^\infty, U^\infty)$. After some tedious evaluation, we obtain the following system of algebraic equations for the unknown Fourier components of the surface traction $\mathcal{F}_g$

$$U_f(x_0, \sigma_0) = U_f^\infty(x_0, \sigma_0) - \frac{1}{4\pi\mu} \sum_i \int_{C_{pi}} \Phi_{fg}(\hat{x}, \sigma, \sigma_0) \mathcal{F}_g(x, \sigma) \sigma dl(x). \tag{4.2.16}$$

Here $dl(x)$ denotes arc length along the tangent to the surface contour C_{pi} and the kernel Φ is given by

$$\Phi_{\alpha\beta} = \begin{bmatrix} A_{11} + \hat{x}^2 B_{31} & \hat{x}(\sigma B_{31} - \sigma_0 B_{32}) & \hat{x}\sigma_0(B_{32} - B_{31}) \\ \hat{x}(\sigma B_{32} - \sigma_0 B_{31}) & A_{12} + (\sigma^2 + \sigma_0^2) B_{32} - \sigma\sigma_0(B_{33} + B_{31}) & A_{10} - A_{12} + \sigma_0^2(B_{30} - B_{32}) - \sigma\sigma_0(B_{31} - B_{33}) \\ \hat{x}\sigma(B_{30} - B_{32}) & A_{10} - A_{12} + \sigma^2(B_{30} - B_{32}) - \sigma\sigma_0(B_{31} - B_{33}) & A_{12} + \sigma\sigma_0(B_{31} - B_{33}) \end{bmatrix}, \tag{4.2.17}$$

and A_{mn}, B_{mn} are defined by (4.2.14).

The relationship between the Fourier components of the surface traction and the actual

shear stress (f_x, f_σ, f_ϕ) is given by

$$(f_x, f_\sigma, f_\phi) = (2\mathcal{F}_x \cos\phi, 2\mathcal{F}_\sigma \cos\phi, -2\mathcal{F}_\phi \sin\phi). \tag{4.2.18}$$

The components of the force and torque over the boundary S_{pi} are computed by contour integrals along C_{pi}, i.e.

$$F_y = 2\pi \int_{C_{pi}} (\mathcal{F}_\sigma + \mathcal{F}_\phi)\sigma dl(x) \tag{4.2.19}$$

$$T_z = 2\pi \int_{C_{pi}} [x(\mathcal{F}_\sigma + \mathcal{F}_\phi) - \sigma\mathcal{F}_x]\sigma dl(x). \tag{4.2.20}$$

Numerical solution of the integral equations (4.2.12) and (4.2.16) is implemented by introducing a standard boundary element collocation technique. First, each part of the boundary contour is discretized by a line segment over which the surface traction $\mathcal{F}$ is assumed to be constant. The boundary elements are non-uniformly distributed in order to resolve the fine structure of the flow field. Typically the size of an element is adjusted smaller in regions where the flow has large gradients. We apply (4.2.12) or (4.2.16) at the mid-point of each line segment over all the contours. This yields a system of linear algebraic equations that can be solved by standard reduction methods. The accuracy of the method should improve as the number of the elements is increased. Numerical convergence tests and solutions obtained for bounded and unbounded flows will be presented in the results section.

4.3 Evaluation of Singular Integrals

One of the main difficulties in the boundary integral equation method is the accurate calculation of the singular integrals over the element that includes the collocation point. In this region, the kernel of the integral equation (4.2.12) and (4.2.16) exhibits logarithmic singularities. The diagonal components of Ψ in (4.2.13) and Φ in (4.2.17) behave in a

singular manner as $\ln(r)$ as $\mathbf{x}_0 \to \mathbf{x}$ although the off-diagonal components remain regular. Over the past two decades, several techniques have been suggested to remove this singular part of the numerical quadrature using analytic methods to accurately evaluate the singular contribution. This is critical in the numerical procedure, since the Fredholm integral equation of the first kind suffers numerical instability when an ordinary quadrature scheme is applied. The accurate evaluation of these singular integrals using asymptotic expansions improves the diagonal dominance of the coefficient matrix thereby making it more robust in numerical inversion. However, this subtraction and addition technique only works well for small values of α and will fail for large α (Pozrikidis 1988, Loewenberg 1994).

Recently, Muldowney & Higdon (1995) have suggested a technique which is very effective in solving boundary integral equations for creeping flow problems. This method is based on a transformation of the integrand that clusters quadrature points in the proximity of the singularity. Detailed numerical tests of this method on various singular integrals of the form

$$I = \int_{-1}^{1} \frac{g(s)}{\sqrt{as^2 + bs + c}} ds \tag{4.3.1}$$

in which the denominator of the integrand has a zero on $[-1, 1]$ and s is the parameterized variable, reveal extremely fast convergence and high accuracy with respect to the order of normal Gauss-Legendre quadrature. For brevity, assume a singular point $s_o = 0$ and let z_i denote a standard Gauss-Legendre quadrature point. If we define a mapped variable

$$s_i = \left(\frac{\sinh \beta \xi_i}{\sinh \beta} \right)^2 \tag{4.3.2}$$

in which $\xi_i = \frac{1}{2}(1 + z_i)$ is the shifted quadrature point and treat β as an empirical constant whose value lies in the range $3 < \beta =< 4$, one obtains good overall performance. We have also tried other transformation forms such as simple power functions and have obtained better results than simple subtraction-and-addition or multi-domain subdivision methods.

The success of this novel algorithm can be interpreted from two viewpoints. From a

geometric point of view, the mapping (4.3.2) clusters points around the singularity while maintaining a regular spacing over the remainder of the integration interval. From a mathematical viewpoint, the variable mapping transforms the original singular integrand into a much more regular one where ordinary Gauss-Legendre quadrature can be applied with high accuracy. The nearly singular integrals which arise in close proximity to the collocation point have the form

$$I = \int_{-1}^{1} \frac{g(s)}{((s - s_0)^2 + d^2)^{m/2}} ds, \tag{4.3.3}$$

where $s_0 \in (-1, 1)$, are treated in a similar manner. The mapping variable is chosen in such a way that the singular point is removed from the interval of integration, but infinity is maintained at a respectful distance. Following the procedure by Muldowney & Higdon, the following transformation is used in our numerical scheme

$$s = s_0 + d \sinh(n \sinh^{-1} \xi), \tag{4.3.4}$$

where the optimal choice of the parameter n is the greatest integer satisfying

$$n \leq (1 + \ln \epsilon^{-1}) \tag{4.3.5}$$

$$\epsilon = d \quad \text{if} \quad |s_0| < 1, \qquad \epsilon = \min\{d, |s_0| - 1\} \quad \text{if} \quad |s_0| > 1. \tag{4.3.6}$$

While this variable transformation method is used for both the singular and nearly singular integrals, the adaptive Romberg quadrature is employed for the regular integrals. The local error is prescribed as $\epsilon = 10^{-6}$ in order to ensure adequate global accuracy. One finds that our method can successfully solve the integral equation (4.2.12) and (4.2.16) for high values of α, i.e., a medium with closely spaced fibers.

4.4 Results and Discussion of Numerical Results

4.4.1 Convergence

In order to demonstrate the reliability and accuracy of our method, we have performed a series of computations for simple particle motions in a Brinkman medium where there are known accurate results. All the numerical calculations were performed on a DECstation 3100. The computational time varied from several seconds to tens of minutes, depending on the number of surface elements used, the accuracy requirement for numerical evaluation of the integrals, and the value of the parameter α which characterizes the properties of the medium. We start with the pure translation of a sphere of radius r_s, whose analytic solution for drag is given by

$$F = 6\pi\mu U r_s \left(1 + \alpha + \frac{1}{9}\alpha^2\right) \tag{4.4.1}$$

Numerical results using 12, 24, 32 and 64 evenly distributed elements on the contour circle show relatively fast convergence to the exact results for all α. The results using 32 elements and 64 elements differ by less than 0.2% and 0.1% from the exact solution (4.4.1), respectively. Using an error analysis similar to creeping flow, one can show that the discretization error in the present method is $O(\delta^2)$, where δ is the maximum size of the elements. The accuracy is further improved by using Richardson extrapolation for successive computations. We also calculated the drag on a disk translating edgewise using the boundary integral equation method. Comparison with the solution obtained by the dual integral equation method (Feng *et al.* 1998) shows very good agreement for α up to 50.

We next examined the translation of two spheres of the same radius r_s and center-to-center spacing $2d$ moving perpendicular to their line of centers in a Brinkman medium (Kim & Russel 1985a). This motion is equivalent to a sphere translating parallel to a free surface, which will be discussed in detail in the next section, see figure 4.1b. To the authors' knowledge, this is the only particle geometry other than a single sphere for which the Brinkman equation has been solved using either the method of reflections or

the more accurate boundary collocation techniques developed by Gluckman *et al.* (1971). Unfortunately, Kim & Russel present graphical results rather than the detailed numerical results needed to rigorously evaluate the accuracy of the present technique. Thus, we first construct a solution using the original formulation of Gluckman *et al.* and then compare the results with those obtained by the present boundary integral equation method. This formulation is simpler but less versatile than the more robust method provided by Kim & Russel.

It can be shown that the multipole expansion of the general series solution of the Brinkman equation can be constructed from three auxiliary functions obtained by solving the Helmholtz equation (Kim & Russel 1985a). These auxiliary functions, representing the pressure field p, poloidal field Φ and toroidal field χ, respectively, have simple forms in spherical coordinates. The velocity due to the translation of these two spheres $i = 1, 2$ can be expressed in terms of the following multipole expansion:

$$\mathbf{v} = \sum_{i=1}^{2}[-\frac{1}{\mu\alpha^2}\nabla_i p_i + \nabla_i \times \nabla_i \times (\mathbf{x}_i\Phi_i) + \nabla_i \times (\mathbf{x}_i\chi_i)] \tag{4.4.2}$$

where

$$p_i = \sum_{n=1}^{\infty} a_{ni} r_i^{-n-1} P_n^1(\cos\theta_i)\sin\phi \tag{4.4.3}$$

$$\Phi_i = \sum_{n=1}^{\infty} b_{ni} k_n(\alpha r_i) P_n^1(\cos\theta_i)\sin\phi \tag{4.4.4}$$

$$\chi_i = \sum_{n=1}^{\infty} c_{ni} k_n(\alpha r_i) P_n^1(\cos\theta_i)\cos\phi, \tag{4.4.5}$$

where the modified spherical Bessel function of the second kind k_n is defined by

$$k_n(x) = \sqrt{\frac{\pi}{2x}} K_{n+\frac{1}{2}}(x). \tag{4.4.6}$$

The subscript $i = 1, 2$ means that the indicated quantities and operators are defined in a local coordinate system centered at the center of the ith sphere, as shown in figure 4.1. The

coefficients a_{ni}, b_{ni} and c_{ni} are determined by applying the boundary collocation technique. The drag and torque exerted on each sphere can be expressed as $2a_{11}/3$ and c_{11}/α^2, respectively, after normalization by the single-sphere result (4.4.1) for the drag and the following expression for the torque (Solomentsev & Anderson 1996)

$$T = 8\pi\mu r_s^3\Omega\frac{1+\alpha+\frac{1}{3}\alpha^2}{1+\alpha} \tag{4.4.7}$$

in which Ω is the angular velocity.

In solving equation(4.4.2) using the boundary collocation technique of Gluckman *et al.*, one satisfies the boundary conditions on the surface of each sphere at discrete points evenly distributed on the contour. Since the resulting coefficient matrix will be singular if any of the collocation points are located on either the equator or at the poles, a small shift from these positions is made as discussed in Ganatos *et al.* (1982b,c) in order to circumvent this difficulty. The calculation converges very rapidly as the number of collocation points is increased. These results are listed in table 4.1 along with the numerical results obtained by the present boundary integral equation method. In the present method, each of the sphere contours is divided into 32 line segments of equal length and further calculation using a larger number of elements has little influence on the convergence of the drag and torque coefficients. From table 4.1, we find that there is remarkably good agreement for both the drag and the torque coefficient even when the two spheres are close to each other, $d/r_s = 1.05$. It is also important to note that the torque exerted on each sphere is largely damped out by the intervening medium as α increases. This rapid decrease in torque indicates that confining boundaries or the other particles in the flow field will be significantly shielded by the medium at relatively small porosity. This shielding will be discussed further in the following sections.

4.4.2 Results for Translation of a Sphere Near a Planar Boundary

In this section, we first consider the motion of a translating sphere of radius r_s with velocity U in the presence of a planar boundary in a fiber-filled medium with dimensionless permeability α, as illustrated in figure 4.1a, b. The effective medium approach and the boundary integral equation method formulated in the previous sections are used to obtain the solutions. The confining boundary can be either a solid wall on which the no-slip boundary condition must be observed or a planar free surface on which the shear stress vanishes. We only consider translation of the particle because for rotation, the double layer contribution cannot be evaluated analytically and the computational expense will be tremendously increased. It is of particular interest to calculate the force and torque exerted on the sphere. These results will serve to demonstrate the combined effects of the surrounding fibers and the confining wall on the particle motion and reveal the hydrodynamic interactions in a fiber-filled medium.

Following established notation for Stokes flow, we express the drag and torque exerted on the sphere that translates perpendicular to a planar boundary with velocity U in terms of dimensionless resistance coefficients which are normalized by either the Stokes results for an unbounded sphere, which reveal the combined effects of the fibrous medium and the confining boundary, or the Brinkman results for an unbounded sphere, which are suitable for inspecting the effect of the confining boundary in a Brinkman medium. Similarly, for parallel motion, the torque introduced by the presence of the wall will be normalized by either the Stokes torque on a rotating sphere in an infinite medium or result (4.4.7) for a sphere rotating in an unbounded Brinkman medium with angular velocity U/r_s.

For translation of a sphere toward a free surface, the flow field is equivalent to that generated by two spheres exhibiting mirror symmetry with respect to the free surface moving toward each other with equal velocity along their line of centers. In order to compare with the results obtained by the boundary integral method, we present an alternative solution procedure based on the multipole expansion method. Although one can construct the solu-

tion using the general solution (4.4.2) as was done for parallel motion, it is now convenient to introduce the stream function since the flow field is independent of the azimuthal angle ϕ. Following Lawrence & Weinbaum (1986), we express the stream function as

$$\psi = \sum_{i=1}^{2} \left[\sum_{n=2}^{\infty} A_{ni} r_i^{-n+1} C_n^{-1/2}(\zeta_i) + \sum_{n=2}^{\infty} B_{ni} R_n(r_i) C_n^{-1/2}(\zeta_i) \right] \tag{4.4.8}$$

from which the fluid velocity components can be evaluated by

$$v_\sigma = \frac{1}{\sigma}\frac{\partial \psi}{\partial x}, \qquad v_x = -\frac{1}{\sigma}\frac{\partial \psi}{\partial \sigma}. \tag{4.4.9}$$

Here $C_n^{-1/2}(\zeta_i)$ are Gegnebauer function of degree n with argument $\zeta = \cos\theta_i$ and θ_i is shown in figure 4.1a. The R_n are polynomials in $1/r_i$, with an exponential multiplier, given by

$$R_n(r) = r^n \left(\frac{1}{r}\frac{d}{dr}\right)^{n-1} \frac{1}{r} e^{-\alpha r} = \sqrt{r} K_{n+\frac{1}{2}}(\alpha r) \tag{4.4.10}$$

The no-slip boundary conditions are applied on the surface of each sphere using the boundary collocation technique. Once the coefficients A_{ni} and B_{ni} are obtained, the drag on each of the spheres is obtained by the expression (Lawrence & Weinbaum 1986)

$$F_i = \alpha^2 (2\pi A_{2i} + V_p) \tag{4.4.11}$$

where V_p is the particle volume. This expression can be used to check the accuracy of the more general boundary integral solution.

The geometry for both perpendicular and parallel motions can be obtained by rotating the contours $C_{pi}, i = 1, 2$ around the x axis as indicated in figure 4.1. When the sphere moves perpendicular to the boundary, equation (4.2.12) is appropriate, whereas for parallel motion, equation (4.2.16) should be used instead. For parallel motion, we require that $u_x = 0$, $u_y = U$, $u_z = 0$ on the sphere surface, yielding $U_x = 0$, $U_\sigma = U_0$, $U_\phi = U_0$ for the Fourier components. On the solid wall, all velocity components vanish, whereas on the free surface, the derivatives of the velocity with respect to x vanish. The standard boundary

element method is used to discretize the resulting integral equation. More precisely, the sphere contour C_{p1} is divided into straight line segments of equal length, whereas the semi-infinite confining walls C_{p2} are truncated at various distances, $\sigma/r_s = 20$ or larger. Our numerical tests on these various truncations show that $\sigma/r_s = 30$ yields good convergence for both the drag and torque exerted on the sphere at all particle-to-wall spacings tested. The size of the wall elements is adjusted smaller in regions with large flow variation. The smallest wall element near the axis of symmetry is set equal to the size of the smallest element on the sphere surface, whereas the largest boundary element can be $20 - 30$ times that of the smallest element adjacent to the axis of symmetry.

In figure 4.2 we plot the dimensionless resistance for a sphere translating perpendicular to a solid wall, normalized by single-sphere result for either unbounded Stokes flow or the Brinkman medium. The figure shows the variation of the drag with respect to the relative particle-wall spacing h/r_s for some representative values of α. Figure 4.3 shows the corresponding results for a free surface. Comparison of the present results for $\alpha = 0$, i.e., Stokes flow, with the analytical solutions of Brenner (1961), indicates that the relative error lies within 0.1% for all spacings $h/r_s \geq 0.1$. This demonstrates the efficiency and accuracy of the present technique.

As mentioned above, the motion of a sphere in the presence of a free surface is equivalent to the motion of two identical spheres with appropriate boundary conditions. Since this geometry also falls into the category in which the present technique can be applied, the results obtained by solving the integral equations numerically along C_{p1} and C_{p3} (see figure 4.1) can serve to eliminate the discretization and truncation errors due to the infinite extent of the planar boundary and further enables the solution to be obtained using velocity boundary conditions rather than their derivative. Comparison of the numerical results obtained by these two approaches and those calculated by equation (4.4.11) shows excellent agreement, with a relative difference less than 0.1%.

As the gap h tends to zero, the dimensionless drag for both perpendicular and parallel

motion exhibit certain singular behaviors. Surprisingly, the family of curves for small values of α seem to converge to the same value. From a physical viewpoint, the Brinkman equation describes the fluid motion on a length scale of $O(\sqrt{K_p})$, or a fiber boundary layer of thickness $O(r_s/\alpha)$; therefore, the presence of a nearby planar wall will have a major influence on the flow field when $\alpha \leq O(1)$. Mathematically, there are two length scales involved in the motion of a particle near a wall in a Brinkman medium, the fiber boundary layer thickness and the particle-wall spacing. An asymptotic analysis using a multiple scaling technique is required to assess the relative importance of these two effects. In the appendix, a local analysis indicates that the effect of the surrounding fibers is negligible compared to the effect of the confining boundary when $\alpha \leq O(1)$ and $\epsilon/r_s \leq O(1)$, where ϵ is the dimensionless gap width between the sphere and the boundary. Therefore, the well-known results for creeping flow are useful for this case. Comparing figure 4.2a and figure 4.3a, one finds that for small values of α, the effect of the confining boundary on the particle differs greatly depending upon whether the planar boundary is a free surface or a solid wall, as one would expect for Stokes flow. As α increases, the effect of the boundary is shielded by the surrounding fibers which now play a dominant role. The drags are essentially identical for the two cases for large values of α except in a very localized region near contact, see figure 4.2b and 4.3b. In general, the solid wall retards the motion of the sphere more than a free surface for all α.

As mentioned earlier, the motion of a sphere perpendicular to a planar boundary can be used as a idealized model to estimate the hydraulic resistance of a microvilli tip as it penetrates the endothelial surface glycocalyx coating the exterior surface of the cell membrane. The minimum gap height between the microvilli and the membrane before receptor-ligand binding occurs is between 20 and 50nm, leading to values of h/r_s that range from 1.2 to 1.5 for a microvilli of 100nm diameter. If the fiber spacing is 7nm and the fiber radius lies between 0.6 and 2nm, the approximate formula (4.5.3), discussed in the next section, predicts that α lies in the range 18.8 to 23.6. Using the results for $\alpha = 10$ in figures 4.2a and 4.2b, one concludes that the drag exerted by the glycocalyx will be much higher than the Stokes drag, and, although the effect of the membrane is greatly diminished by the surface glyco-

calyx, there is still a significant effect for $1.2 \leq h/r_s \leq 1.5$, see figures 4.2b and 4.3b. Thus the present results indicate that the previous use of resistance functions based on Stokes flow is inappropriate for modeling the motion of microvilli in proximity to the endothelial surface. Detailed calculations for the local surface traction on the sphere indicate that the front half of the sphere encounters more than 70% of the total drag experienced by the particle for $h/r_s = 1.2$ and $\alpha = 1$, but that this differential decreases as α increases and h/r_s decreases. A more realistic model for a microvilli is a hemisphere attached at the end of a circular cylinder. The hydrodynamic penetration force can be approximated by adding the resistance due to the longitudinal translation of a long cylinder in an unbounded medium and the resistance due to the front half of a sphere moving toward a planar boundary.

Figures 4.4a and 4.4b present the resistance coefficient for the parallel motion of a sphere adjacent to a plane normalized by the Stokes or Brinkman results for a sphere moving in an unbounded medium, respectively. One observes that the effect of the boundary on the sphere is much weaker than for perpendicular motion and exhibits new features not present for perpendicular motion. The drag on a sphere moving parallel to a free surface does not decrease monotonically with increasing distance from the boundary, although this is the case for parallel motion adjacent to a solid wall. The drag normalized by the Brinkman solution for an unbounded sphere can be smaller or larger than unity, indicating that the nearby free surface will either retard the motion of the sphere or enhance it depending on the relative distance from the free surface. This behavior is the result of two competing effects. When $\alpha \leq O(1)$, which means that the porous medium is dilute, the far field Stokes interaction, which decays as $(O(1/r))$ is most important. In this case, due to the shear-free boundary condition on the surface, the fluid in the region between the sphere and the free surface moves along with the sphere rather than retarding its movement. Therefore, the resistance coefficient is smaller than one. On the other hand, when α increases, the resistance of the fibers dominates the motion and the fluid displaced in the near contact region contributes an additional resistance, which causes $F/F_b > 1.0$. The motion of a sphere parallel to a free surface is equivalent to two identical spheres moving perpendicular to their line of centers.

When their center-to-center distance is sufficiently small, the fluid between the two spheres move with the particles as if the sphere pair is enlarged, leading to a higher resistance. For intermediate values of α, the competition between the fiber layer and the nearby boundary produces more a complicated behavior for the drag and torque, as shown in figures 4.4 and 4.5. Figure 4.5 shows that the effect of the fibers on the torque is much weaker than their effect on the drag and that the torque has a maxima for $\alpha \geq 0.5$.

The results presented in figures 4.4a, b are most relevant for the lateral diffusion of molecules in the surface glycocalyx. Using formula (4.5.3), one finds that α for a molecule of 4nm diameter varies between 0.75 and 0.94 for fibers of 0.6 to 2nm radius when $\Delta = 7$nm. For α in this range, the influence of the membrane can be considerable. For example, the membrane can cause a 45 percent increase in drag compared to an unbounded Brinkman medium for $\alpha = 1.0$ and $h/r_s = 1.1$. One also notes that there is about 50 percent more drag for motion near a solid wall than near a free surface when $h/r_s = 1.1$ and $\alpha = 1.0$. This difference diminishes as h/r_s or α increases. In single particle tracking experiments, where 40nm colloidal gold or 210nm latex particles are used as tracers to study the cytoplasmic regulation of the movement of cell-to-cell adhesion molecules (Sako *et al.* 1998), the surface dynamics of transmembrane integrins (Schmidt *et al.* 1993) and the fence structure of the actin cytoskeleton (Sako & Kusumi 1995), the values of α greatly exceed those plotted in figure 4.4. Formula (4.5.3) predicts that α varies between 7.5 and 9.4 for the 40nm gold particles and 39.4 and 49.5 for the 210nm latex beads when $\Delta = 7$nm and $0.6 < a < 2$nm. For these values of α the drag is almost the same as for an unbounded Brinkman medium for either the solid or free surface boundary condition. Using the unbounded Brinkman expression for the drag and the Stokes-Einstein relation for the diffusion coefficient D, one estimates that D for the 40nm gold particle lies in the range $5.1 \times 10^{-9}\text{cm}^2/\text{sec}$ to $7.2 \times 10^{-9}\text{cm}^2/\text{sec}$. The experiments in Lee *et al.* (1993) which are based on the total resistance of the matrix, including elastic and fiber binding energy, indicate that for the diffusion of the gold-tagged molecule, D ranges from 1.1 to $1.7 \times 10^{-9}\text{cm}^2/\text{sec}$. However, the average diffusion coefficient of the bilipid molecule is about 5.4 to $9.5 \times 10^{-9}\text{cm}^2/\text{sec}$, which is

much higher than the measured value due to the absence of the attached gold particle. If we assume the that the plasma membrane and the surface glycocalyx are separate layers whose components move independently, then the total drag exerted on the gold-tagged molecule is the sum of these two individual contributions. This suggests that the hydrodynamic resistance on the gold-tagged particle accounts about 15 to 50 percent of the increased resistance. Therefore, the additional resistance can not be adequately accounted for by only the hydrodynamic resistance. We conclude that in this case, the elastic and binding energy associated with the surface glycocalyx is of comparable importance to hindered diffusion of the gold-tagged molecule in a bilipid membrane.

4.4.3 Results for Translation of a Sphere in a Channel

We next consider a sphere translating in a fiber-filled medium confined by a parallel walled channel of normalized height $2H$ scaled by the sphere radius r_s, see figure 4.6. This geometry can be obtained by rotating the contours $C_{pi}, i = 1, 2, 3$ around x axis as indicated in the figure. The solution for this flow problem is obtained by solving the boundary integral equations (4.2.12) and (4.2.16) along $C_{pi}, i = 1, 2, 3$. The standard boundary element method is used to discretize the resulting integral equation, as described in detail in the previous subsection. Typical convergence tests on the normalized drag for parallel motion are presented in table 4.2 with increasing number of elements on the contours. As we can see in table 4.2a, our results for $\alpha = 0$ agree closely with those obtained by the multipole collocation technique (Ganatos *et al.* 1980b) for the creeping motion of a sphere in a channel. The relative error is less than 0.5 percent for all values of H. For $\alpha = 1.0$, table 4.2b, the number of boundary elements is increased until 0.5 percent convergence was achieved. This convergence test indicates that sufficiently accurate solutions can be achieved with 64 elements on each of the boundary contours for all possible types of motion.

We focus our attention to parallel motion. In figures 4.7 and 4.8 we have plotted the resistance coefficients for the drag and torque for a sphere translating in a parallel walled

channel for various values of α and H. These coefficients are normalized by the drag and torque on a sphere translating or rotating in Stokes flow with the same translational or angular velocity. The results for the drag have the same qualitative behavior as for Stokes flow. The results for the torque show that the direction of rotation, if the sphere were not held fixed, would change for a significant range of b/H. This phenomenon is also observed for a sphere translating in a channel in Stokes flow (Ganatos *et al.* 1980b). From these figures, we can conclude that the effect of the walls on the sphere is localized to the region near the walls for all α. As the value of the parameter α increases, the effect of the wall becomes even smaller as one would intuitively expect due to fiber shielding. In Stokes flow, we know the wall effect decays as $O(1/r)$, where r is the distance from the boundary. However, in a fiber-filled medium, the effect of the confining boundaries is diminished by the presence of the fibers which shield the sphere from the wall. As α increases, the effect of the fibers dominates the drag and torque on the sphere even when the sphere is close to the wall. Therefore, the effect of the confining walls becomes less important for $\alpha \geq 2.0$. The corresponding results for the torque on the sphere exhibit a more complicated departure from the results for Stokes flow. As α increases, the torque becomes exclusively positive. It is also evident that the torque coefficient has steep gradients in the proximity of the walls.

4.5 Application to Transendothelial Transport

In this section, numerical results presented in section 4.4 are utilized to provide an improved model for determining the diffusion coefficient for the passage of spherical molecules through an interendothelial cleft filled with a fiber matrix. The continuum hydrodynamic theory used to calculate the phenomenological coefficients in the Kedem-Katchalsky equations derived from irreversible thermodynamics, will be extended to a Brinkman medium to account for particle-matrix interactions produced by the fiber components in the intercellular cleft between adjacent endothelial cells. In an earlier paper (Weinbaum *et al.* 1992), a new three-dimensional model was developed to elucidate some long-standing issues

arising from attempts to relate the observed ultrastructural organization of the capillary interendothelial cleft and measured values for its permeability. A simple multiplicative formula was proposed to estimate the diffusive permeability of spherical solute molecules in an interendothelial cleft with cross-bridging cylindrical fibers.

We first wish to determine the permeability K_p of the intercellular matrix. According to Darcy's law, the global permeability of the medium can be expressed as

$$\frac{Q}{A} = \frac{K_p}{\mu}\frac{\Delta p}{L}, \tag{4.5.1}$$

in which Q is the volumetric flux rate through a cross-sectional area A due to a pressure gradient over a length L in the fiber-filled medium. Tsay *et al.* (1991) have examined the validity of the effective medium approach by comparing the solution for the Stokes flow through a periodic square array of circular cylindrical fibers in a channel with the solution for the same channel flow using effective medium theory. An empirical formula based on the extrapolation of the results for the two-dimensional drag coefficient, was obtained for the case in which the height of the channel becames infinite. The following simple expression for the Darcy permeability was proposed

$$K_p = 0.0572a^2\left(\frac{\Delta}{a}\right)^{2.377}, \tag{4.5.2}$$

where a is the radius of the fibers and Δ is the open gap between two adjacent fibers in the periodic array. Equation (4.5.2) provides good agreement with the numerical solutions of Sangani & Acrivos (1982) for an infinite two-dimensional fiber array for all values of the fiber fraction S in the range $0.001 \leq S < 0.7$. Using (4.5.2), one can express the dimensionless parameter α as

$$\alpha = 4.18\frac{r_s a^{0.189}}{\Delta^{1.189}}. \tag{4.5.3}$$

It is clear that the diameter of the spherical particle must be smaller than Δ for it to undergo Brownian motion in this periodic fiber array. This leads to a maximum allowable

value α_{max} for a spherical particle of diameter $2r_s = \Delta$, namely,

$$\alpha_{max} = 2.09 \left(\frac{a}{\Delta}\right)^{0.189}. \tag{4.5.4}$$

Two typical fibers that are believed to comprise the intercellular matrix are the sialyic side chains of proteoglycans, $a = 0.6$ nm radius, and their protein core, $a = 2$ nm radius. The variation of α_{max} with Δ is plotted in figure 4.9 for three fiber radii in this range. For $\Delta = 7$ nm, a fiber spacing that would allow only molecules smaller than albumin (diameter 7.2 nm) to pass, α_{max} lies between 1.30 and 1.65 for fiber radii between 0.6 and 2 nm. Subject to this constraint on α_{max}, we shall now apply the effective medium approach to estimate the diffusion coefficient for a spherical particle moving in a parallel walled channel.

The hydrodynamic force and torque on a translating spherical particle in a fiber-filled channel can be written as

$$F = 6\pi\mu r_s[UF_y^t + r_s\Omega F_z^r], \tag{4.5.5}$$

$$T = 8\pi\mu r_s^2[UT_y^t + r_s\Omega T_z^r], \tag{4.5.6}$$

where F_y^t, T_z^t are the force and torque coefficients for the motion of a sphere due to a pure translation in the y direction, while F_y^r and T_z^r are the corresponding coefficients due to a pure rotation about the z axis, see figure 4.6. The balance between the hydrodynamic force and the gradient of the chemical potential on a neutrally buoyant, torque free particle yields

$$\frac{6\pi\mu r_s}{F(\alpha,\delta,s)}U = \frac{1}{N_A}\left[RT\frac{dc}{dx} + \bar{V}_s r_s \frac{dP}{dx}\right], \tag{4.5.7}$$

where

$$F(\alpha,\delta,s) = \frac{-T_z^r}{F_y^t T_z^r - F_z^r T_y^t}. \tag{4.5.8}$$

Here c is the molar concentration, $\bar{V}_s$ is the molar volume, N_A is Avogadro's number, R is the universal gas constant, T is the absolute temperature, and δ and s are geometric parameters defined by $\delta = r_s/H$ and $s = b/2H$. As noted earlier, considerable computational effort is

required to calculate the double layer potential in the boundary integral equation presented in section 4.4 for the pure rotation of a sphere. We notice, however, that the rate of growth of F_y^t with respect to α is much faster than that of T_y^t. According to the Lorentz reciprocal theorem, the two coefficients F_z^r and T_y^t are related to each other in the creeping limit as $3F_z^r = 4T_y^t$. Thus, a reasonable approximation to $F(\alpha, \delta, s)$ is

$$F(\alpha, \delta, s) \simeq -\frac{1}{F_y^t} \tag{4.5.9}$$

Using a procedure proposed by Levitt (1975), one can write the diffusive permeability ω of the particle, after applying the conservation of flux through the cleft, as

$$\omega = \frac{L_p}{V_s}\frac{2}{3}\delta^2(1-\delta)\bar{F}, \tag{4.5.10}$$

where

$$\bar{F}(\alpha, \delta) = \frac{2}{1-\alpha}\int_{r_s/2H}^{1/2} F(\alpha, \delta, s)ds. \tag{4.5.11}$$

The left side of equation (4.5.7) is the drag force on the sphere. If we assume as a first approximation that all possible positions in the channel cross section are equally likely, except the region of steric exclusion near the walls, then one can show that the mobility of the solute in the channel is given by $6\pi\mu r_s/\bar{F}(\alpha, \delta)$. If we now multiply (4.5.7) by $F(\alpha, \delta, s)/6\pi\mu r_s)$, integrate across the channel height and notice that the ratio R/N_A is just the Boltzman constant k, one can define the effective diffusion coefficient as

$$D_m = \bar{F}(\alpha, \delta)D_\infty, \tag{4.5.12}$$

where D_∞ is the free diffusion coefficient from Stokes-Einstein theory for an infinite medium without a matrix.

The foregoing hydrodynamic theory does not include the effects of steric exclusion of the particle by the fibers and the spatial variation of the particle concentration in the

available space of the fiber-filled medium. The steric exclusion contributes significantly to the diffusive permeability of the particle, especially when $r_s/a \sim 1$. In Weinbaum *et al.* (1992), a simple multiplicative formula was proposed to account for the combined effects of hydrodynamics and steric exclusion, namely, that the effective diffusion coefficient could be written as

$$D_{eff} = D_m F(S), \tag{4.5.13}$$

where D_m describes the hydrodynamic interaction and $F(S)$ the steric exclusion. The function $F(S)$ describes the diffusion of a point solute in the unbounded fiber array. The steric factor S is defined by the excluded volume that is not accessible to the solute molecule. This same approach has also been adopted in Johnson *et al.* (1996) on the basis of hydrodynamic arguments proposed in Brady (1994).

Weinbaum *et al.* (1992) determined the steric factor $F(S)$ by solving the solute diffusion equation for a doubly periodic fiber array in which the zero flux boundary condition is imposed at the exclusion radius, $r_e = r_s + a$. Therefore, steric exclusion is treated as a geometric restriction in which the center of the particle cannot enter a region within a distance less than r_s from the fiber surface. Equivalently, the fiber radius is augmented by the particle radius. Using (4.5.13) and this solution for the steric function $F(S)$, one obtains

$$D_{eff} = D_m \left(\frac{1 - b_1 S_e}{1 + b_1 S_e} \right), \tag{4.5.14}$$

where b_1 is a constant representing the flow configuration. b_1 depends only on the effective fiber solid fraction $S_e = S(1 + r_s/a)^2$ and is given in figure 5 of Weinbaum *et al.* (1992). It decreases rapidly with increasing effective solid fraction S_e.

To test the applicability of the simple approximation (4.5.14), we first examine the diffusion of a solute molecule of radius r_s in an unbounded square array of parallel fibers of radius a. This same problem has been rigorously treated using generalized Taylor dispersion theory and a Stokesian dynamic simulation in which the fibers are described by a bead and string model (Phillips *et al.* 1990). This comparison is shown in figure 4.10. In the

effective medium approach one uses the Brinkman solution for the motion of a sphere in an unbounded medium (4.4.1) to calculate D_m. Also shown in the figure are the results predicted by the effective medium theory without the steric correction factor in (4.5.14). It is clear that the steric correction provided by the simple multiplicative formula (4.5.14) provides a substantial improvement, especially for values of $r_s/a \neq 1$.

To examine the diffusion of a solute molecule in a channel filled with a Brinkman medium, D_m given by equation (4.5.12) has been plotted in figure 4.11. One notes that the effect of the walls, the departure from the solution for $H = \infty$, is most significant for small values of α, i.e., low fiber fractions. For $\alpha > 1.0$, the effect of the fibers becomes more important than the walls for $H > 5$, while for $\alpha > 1.65$ the wall effect is greatly damped by fiber shielding. However, as shown in figure 4.9, depending on the fiber spacing parameter Δ, particle trapping may have already occurred and values of $\alpha > 2$ may not be achievable. In general, the presence of the confining walls reduces the diffusion coefficient and is a significant effect for $H < 2$ for all $\alpha \leq \alpha_{max}$ in figure 4.9.

We have also plotted in figure 4.11, dashed lines, the simple multiplicative formula proposed in Weinbaum *et al.* (1992) for D_m in which the hydrodynamic effects of the fibers and the walls are treated separately, i.e., the expression for D_m in (4.5.12) is approximated by

$$D_m = D_{iw}\left(1 + \alpha + \frac{\alpha^2}{9}\right), \tag{4.5.15}$$

where D_{iw} is the diffusion coefficient for a sphere in a parallel walled channel in Stokes flow (Ganatos *et al.* 1980a), and the second factor is the added resistance due to the motion of a sphere in an unbounded Brinkman medium, see equation (4.4.1). We see that the presence of the fibers leads to a substantial increase in the diffusion coefficient beyond the value of predicted by (4.5.15). This increase in D_m results from the shielding of the wall by the fibers surrounding the diffusing solute molecule. One notes that the agreement of (4.5.15) with the present numerical results is good only for either small α, where the effect of the wall dominates, or large α and large H, where the fibers completely shield the particle from

the walls. The discrepancy for intermediate values of α is substantial for all values of the dimensionless channel half height H.

Finally, in figure 4.12, we have plotted the normalized effective diffusion coefficient, scaled by the diffusion coefficient $D_{b\infty}$ for an infinite Brinkman medium, for two different fiber radii when the gap between fibers is 7 nm. At this fiber spacing all molecules larger than albumin would be sieved. Figure 4.12 shows the combined effects of the walls and the steric exclusion factor in equation (4.5.14). For a fine fiber of radius 0.6 nm, for which α_{max} increases linearly with r_s up to $\alpha_{max} = 1.3$, $D_{eff}/D_{b\infty}$ decreases rapidly as r_s increases. As r_s approaches $\Delta/2$, the steric correction $F(S)$ becomes more important than the hydrodynamic interaction. For the larger fibers of 2 nm radius, for which $\alpha_{max} = 1.7$, the hydrodynamic drag on the solute is 20 to 25 percent larger than for the 0.6 nm radius fibers. The steric exclusion factor $F(S)$ is also smaller since the exclusion radius r_e will be larger for the same value of r_s. In general, the combined effects of hydrodynamic wall interaction and steric exclusion result in a significantly lower diffusion coefficient than a solute molecule diffusing in an unbounded Brinkman medium with the same value of α. These results are particularly useful in evaluating current studies of the structure-function relationship for solutes diffusing through interendothelial clefts (Weinbaum *et al.* 1992; Fu *et al.* 1994).

4.6 Concluding Remarks

In summary, this paper has developed a general numerical approach to the solution of the Brinkman equation describing particle motion in a fiber-filled medium with confining walls. Although the present technique is capable of solving the governing equations for any value of α, there is a maximum allowable value for a given fiber structure if a diffusing particle is not to exceed the open clearance between two adjacent fibers. In many biological problems which involve particle diffusion in a fiber-filled medium, this maximum value of α lies in the range 1.2 to 1.7. The hydrodynamic effect of the fibers surrounding the particle will significantly diminish the effect of confining boundaries or other particles when $\alpha > 1.0$.

Since the torque on a rotating sphere due to a confining boundary is a lower order effect than the drag, we are able to neglect particle rotation in our simplified theory for the diffusion of a spherical solute molecule in a parallel walled channel. The results in section 4.5 show that this assumption is also acceptable in the small α limit, Stokes flow. This approximate theory shows that the simple multiplicative formula proposed in Weinbaum *et al.* (1992), where the contribution from the walls and the fibers are treated separately, underpredicts the solute diffusion coefficient.

The boundary integral equation method developed in this paper takes advantage of the symmetry of the flow geometry to reduce the problem to a system of one dimensional integral equations defined on the contours of the particle and the boundaries. An efficient numerical algorithm for evaluating the singular integrals, based on the procedure proposed by Muldowney & Higdon (1995) for Stokes flow is extended to the Brinkman equation. It is demonstrated that the present method is both efficient and accurate, even for large values of α. However, when we consider the general motion of the particle, such as rotation or the presence of a non-uniform upstream flow, the much more complicated contribution of the double layer integral in (4.2.8) can not be simply evaluated as in Stokes flow. Thus the computational efforts will be substantially increased, especially for flows with infinite boundaries, in which a large number of boundary elements are required when the integral equation is discretized. The present method can be readily extended despite these limitations. For example, the axisymmetric motion of sphere in a cylinder filled with a Brinkman medium or the motion of a sphere across the centerline of a circular orifice or the entrance of a circular tube of finite length, can all be investigated using the present method. Since the Brinkman equation is analogous to the unsteady Stokes equation, one can utilize the present method to solve the axial oscillation of an axisymmetric particle at high frequency, a problem for which most earlier techniques will fail.

Appendix

In this appendix, we will show that the leading term for the motion of a sphere near a planar boundary is independent of the permeability parameter α if $\alpha \sim O(1)$ and $\epsilon = \delta/r_s = h/r_s - 1$, the dimensionless gap height, is $< O(1)$. The procedure is an extension to that used for creeping flow (Jeffrey 1982; O'Neill & Stewartson 1967).

For axisymmetric motion perpendicular to an infinite planar boundary, the flow is axisymmetric and it is convenient to introduce the dimensionless stream function which satisfies

$$E^2(E^2 - \alpha^2)\psi = 0 \tag{A1}$$

Introducing two stretched variables

$$R = \epsilon^{-1/2}\sigma, \qquad X = \epsilon^{-1}x, \tag{A2}$$

the governing equation becomes

$$\left[\frac{\partial^2}{\partial X^2} + \epsilon\left(\frac{\partial^2}{\partial R^2} - \frac{1}{R}\frac{\partial}{\partial R}\right)\right]\left[\frac{\partial^2}{\partial X^2} + \epsilon\left(\frac{\partial^2}{\partial R^2} - \frac{1}{R}\frac{\partial}{\partial R}\right) - \epsilon^2\alpha^2\right]\psi = 0 \tag{A3}$$

The boundary condition on the sphere surface in the near contact region is given by

$$\psi = -U_0\sigma^2/2 = -\epsilon R^2/2 \tag{A4}$$

Thus we expand the stream function ψ as

$$\psi = r_s^2\epsilon(\psi_0 + \epsilon\psi_1 + \cdots) \tag{A5}$$

and on substitution into (A3), we obtain a hierarchy of equations,

$$\frac{\partial^4\psi_0}{\partial X^4} = 0, \qquad \frac{\partial^4\psi_1}{\partial X^4} = -2\Theta\frac{\partial^2\psi_0}{\partial X^2}, \cdots \tag{A6}$$

for $\alpha = O(1)$ and

$$\frac{\partial^2}{\partial X^2}\left(\frac{\partial^2}{\partial X^2} - \beta^2\right)\psi_0 = 0, \tag{A7}$$

$$\frac{\partial^2}{\partial X^2}\left(\frac{\partial^2}{\partial X^2} - \beta^2\right)\psi_1 = -2\Theta\frac{\partial^2\psi_0}{\partial X^2} + \beta^2\Theta\psi_0, \qquad \cdots\cdots \tag{A8}$$

for $\alpha = \epsilon^{-1}\beta$ and $\beta = O(1)$ where the operator $\Theta = \partial^2/\partial R^2 - \partial/R\partial R$. The boundary conditions for ψ_i are obtained by a Taylor expansion at $X = 1 + R^2/2$. Notice that for $\alpha = O(1)$, the regular expansion of ψ is identical to creeping flow.

Now consider a sphere of unit radius moving parallel to a planar solid wall. Due to the axisymmetric flow configuration, the pressure $p = \mu P(\sigma, x)\cos\phi$. The momentum equation when expressed in terms of the velocity components $(U\cos\phi, V\sin\phi, W\cos\phi)$ can be written in cylindrical coordinates (σ, ϕ, x) as

$$\frac{\partial P}{\partial \sigma} = L_0^2 U - \frac{2(U+V)}{\sigma^2} - \alpha^2 U \tag{A9}$$

$$-\frac{P}{\sigma} = L_0^2 V - \frac{2(U+V)}{\sigma^2} - \alpha^2 V \tag{A10}$$

$$\frac{\partial P}{\partial x} = L_1^2 W - \alpha^2 W \tag{A11}$$

and the continuity equation becomes

$$\frac{\partial U}{\partial \sigma} + \frac{U+V}{\sigma} + \frac{\partial W}{\partial z} = 0 \tag{A12}$$

where the operator L_m^2 is defined by

$$L_m^2 \equiv \frac{\partial^2}{\partial \sigma^2} + \frac{1}{\sigma}\frac{\partial}{\partial \sigma} - \frac{m^2}{\sigma^2} + \frac{\partial^2}{\partial x^2}. \tag{A13}$$

Introducing the stretched coordinates X and R as defined in (A2), the boundary conditions on the sphere surface together with the continuity equation suggest expansions of the

pressure velocity components in the form

$$P = \epsilon^{-3/2}P_0(R,X) + \epsilon^{-1/2}P_1(R,X) + \cdots \quad \text{(A14)}$$

$$U = U_0(R,X) + \epsilon U_1(R,X) + \cdots \quad \text{(A15)}$$

$$V = V_0(R,X) + \epsilon V_1(R,X) + \cdots \quad \text{(A16)}$$

$$W = \epsilon^{1/2}W_0(R,X) + \epsilon^{3/2}W_1(R,X) + \cdots \quad \text{(A17)}$$

Substitution of the asymptotic expansions into the governing equations leads to a hierarchy of equation, of which the leading order for $\mathbf{U}_0$ and P_0 is either

$$\frac{\partial P_0}{\partial R} = \frac{\partial^2 U_0}{\partial X^2} \quad \text{(A18)}$$

$$-\frac{P_0}{R} = \frac{\partial^2 V_0}{\partial X^2} \quad \text{(A19)}$$

$$\frac{P_0}{R} = 0 \quad \text{(A20)}$$

$$\frac{\partial U_0}{\partial R} + \frac{U_0 + V_0}{2} + \frac{\partial W_0}{\partial X} = 0 \quad \text{(A21)}$$

for $\alpha = O(1)$ or

$$\frac{\partial P_0}{\partial R} = \frac{\partial^2 U_0}{\partial X^2} - \beta^2 U_0 \quad \text{(A22)}$$

$$-\frac{P_0}{R} = \frac{\partial^2 V_0}{\partial X^2} - \beta^2 V_0 \quad \text{(A23)}$$

$$\frac{\partial P_0}{R} = 0 \quad \text{(A24)}$$

$$\frac{\partial U_0}{\partial R} + \frac{U_0 + V_0}{2} + \frac{\partial W_0}{\partial X} = 0 \quad \text{(A25)}$$

for $\alpha = \beta\epsilon^{-1}$ and $\beta \sim O(1)$, provided that $\alpha \leq O(\epsilon^{-1})$. Note that equations (A18)-(A21) are exactly the same as for creeping flow.

The new parameter β defined by $\alpha\epsilon$ can be estimated using the empirical formula

$$\beta = 4.18\left(\frac{a}{\delta}\right)^{0.189}\left(\frac{\delta}{\Delta}\right)^{1.189}, \tag{A26}$$

derived from equation (4.5.3), where δ is the dimensional gap height. When $\beta = O(1)$ the minimum gap between the sphere and the confining wall is comparable with fiber spacing. We anticipate that in this case, the contribution from the surrounding fibers to the drag is as important as that from the boundary.

Comparison with the numerical results for $\epsilon = 0.05, 0.1$ indicates that the following additive formula for the drag provide good approximation for $\alpha \leq 2.0$ for both perpendicular and parallel motions

$$\frac{F}{6\pi\mu r_s U_0} = \left(1 + \alpha + \frac{\alpha^2}{9}\right) + F_{Stokes}, \tag{A27}$$

where F_{Stokes} is the asymptotic drag for a sphere moving close to a planar boundary in Stokes flow.

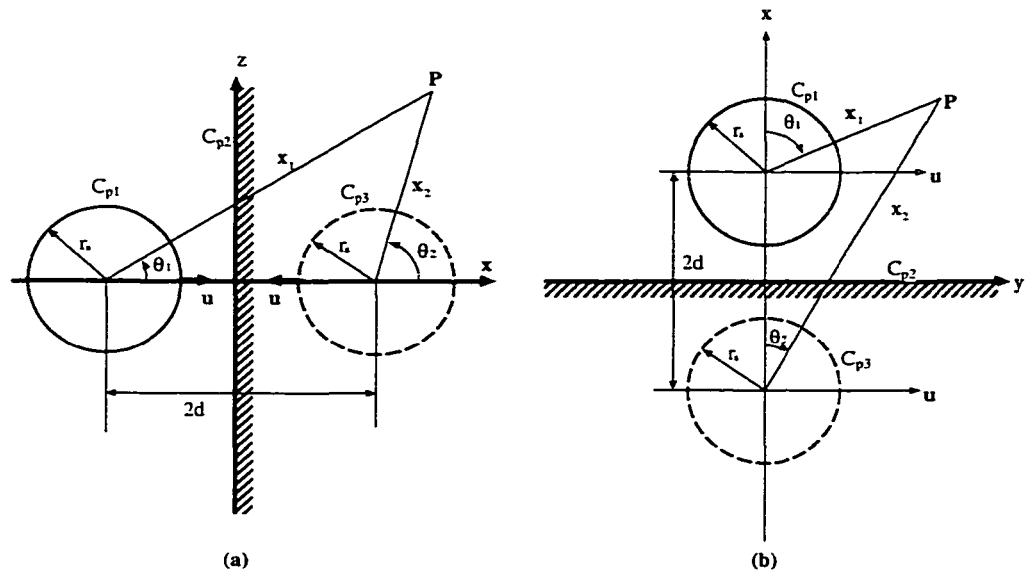

Figure 4.1: Geometry for a sphere translating in the presence of a planar boundary. (a) perpendicular motion; (b) parallel motion.

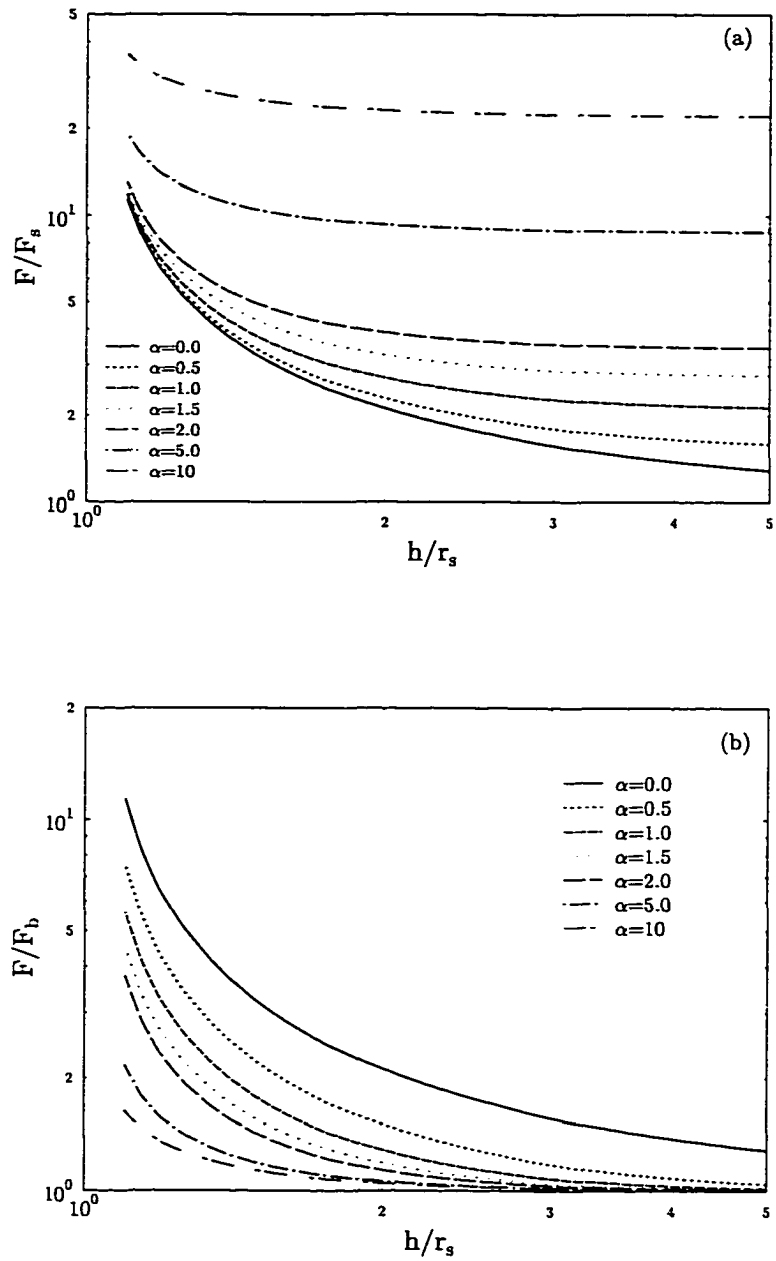

Figure 4.2: Normalized drag on a sphere moving perpendicular to a solid wall. (a) Results normalized by Stokes drag for a single sphere translating in a viscous fluid; (b) Results normalized by drag for a single sphere translating in an unbounded Brinkman medium.

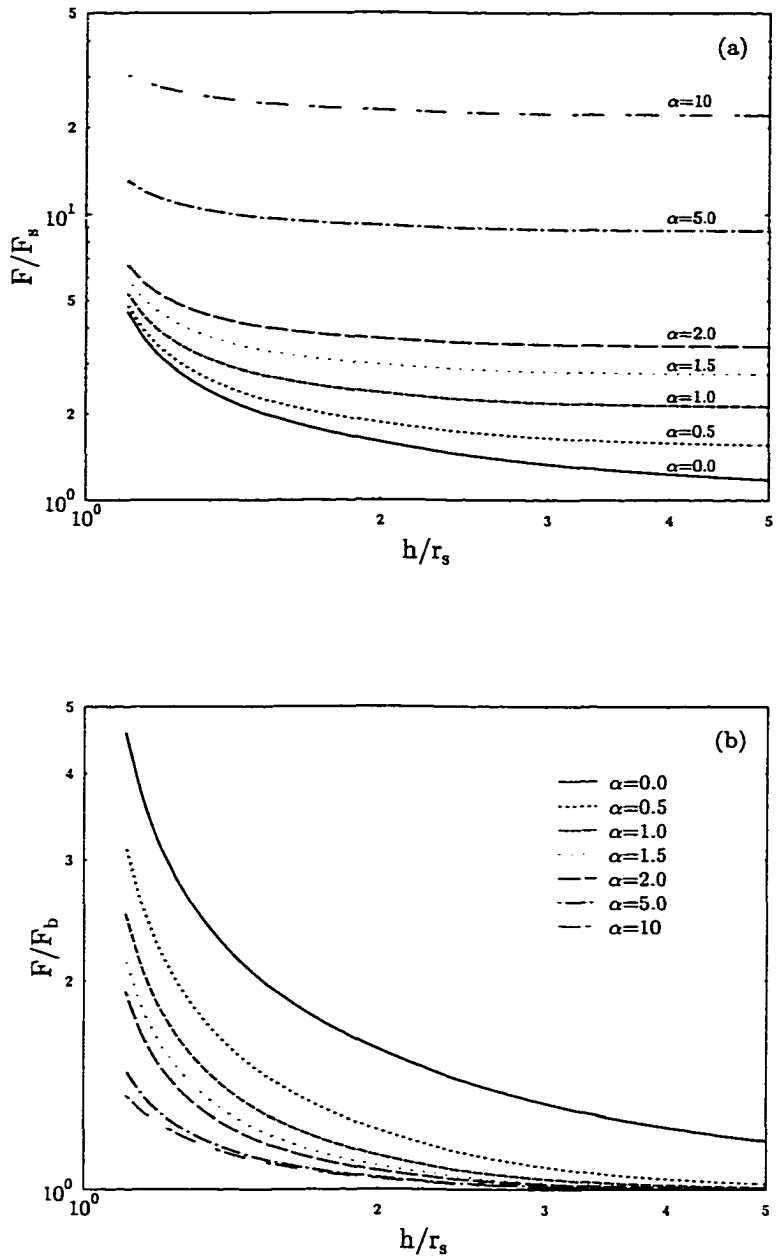

Figure 4.3: Normalized drag on a sphere moving perpendicular to a free surface. (a) Results normalized by Stokes drag for a single sphere translating in a viscous fluid; (b) Results normalized by drag for a single sphere translating in an unbounded Brinkman medium.

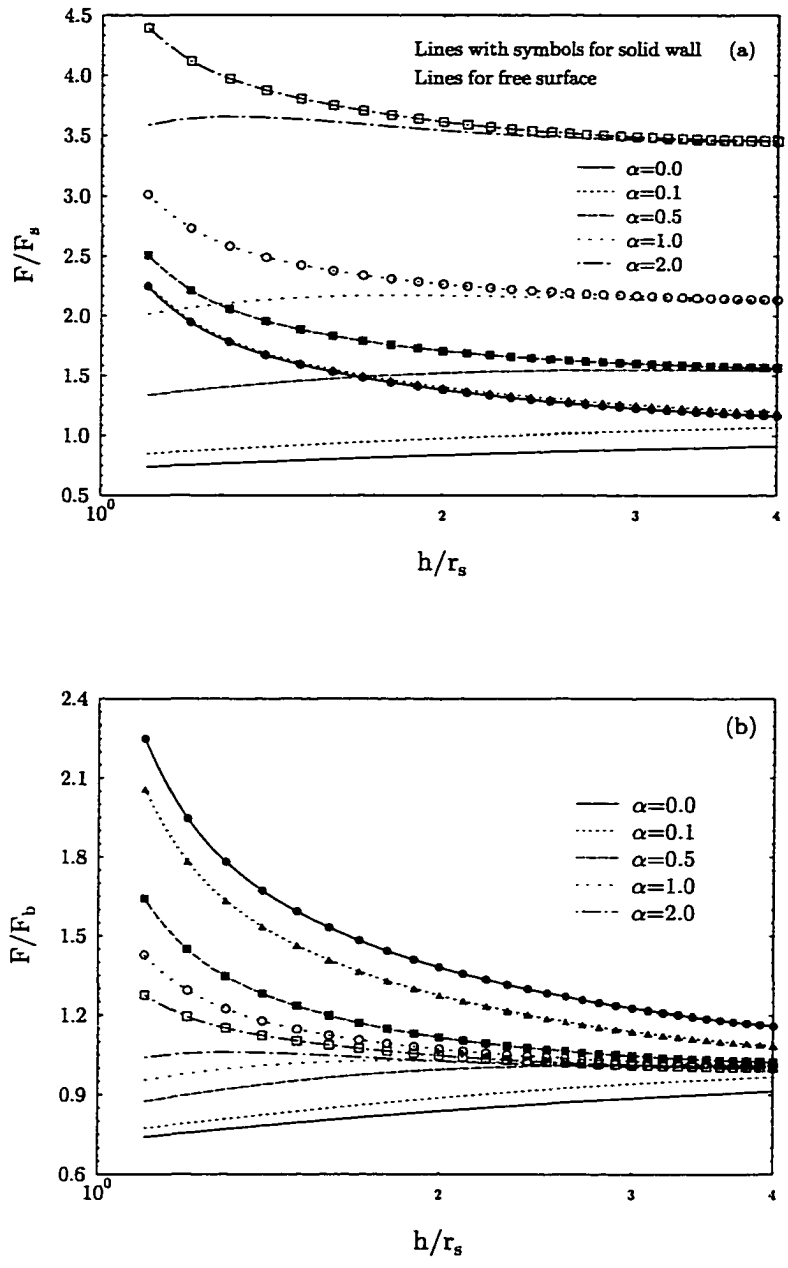

Figure 4.4: Normalized drag on a sphere moving parallel to a planar boundary. (a) Results normalized by Stokes drag for a single sphere translating in a viscous fluid; (b) Results normalized by drag for a single sphere translating in an unbounded Brinkman medium.

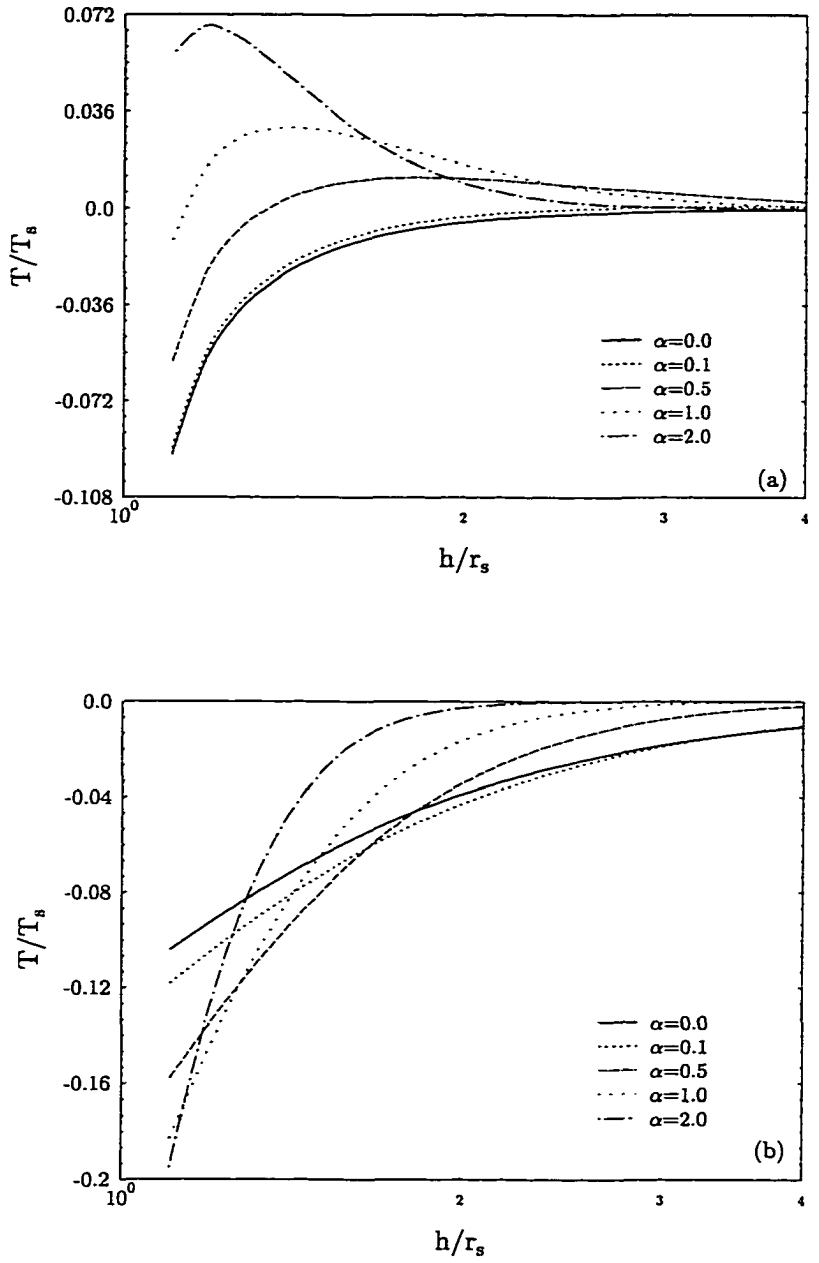

Figure 4.5: Torque on a sphere moving parallel to a planar boundary normalized by Stokes torque for a single sphere rotating in a viscous fluid. (a) solid wall. (b) free surface.

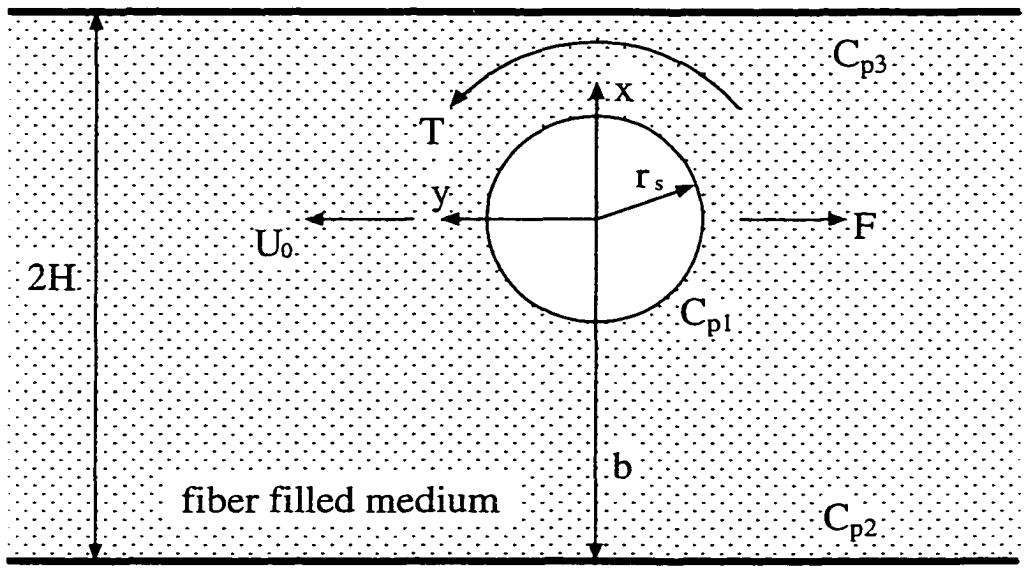

Figure 4.6: Geometry for a sphere moving in a channel.

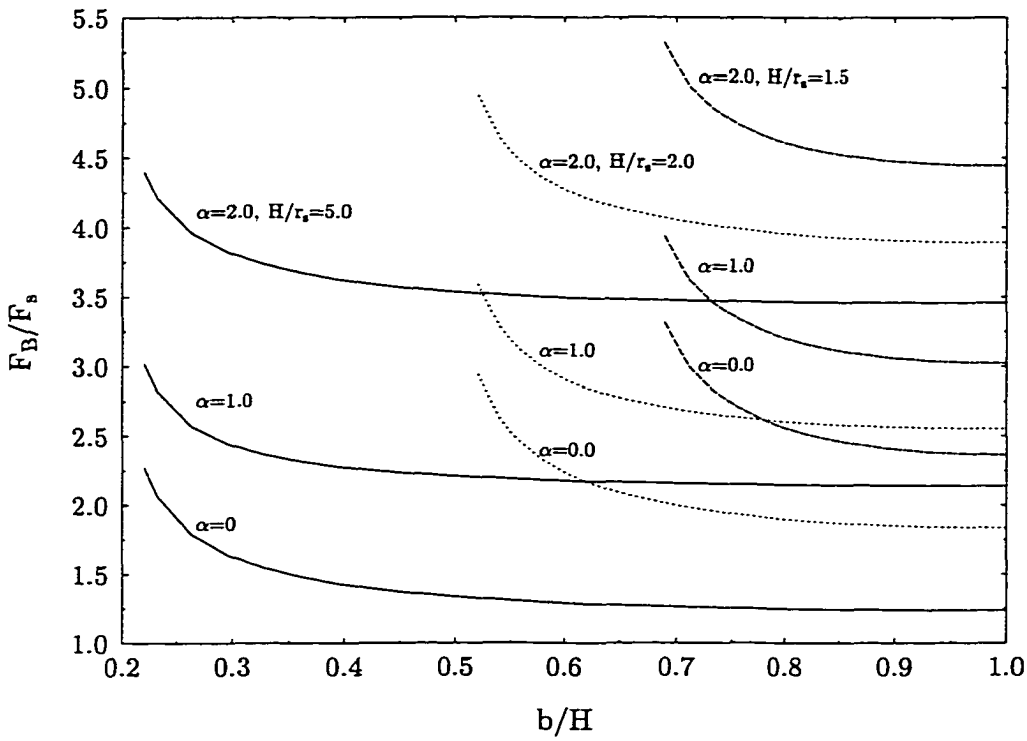

Figure 4.7: Normalized drag on a sphere moving in a channel for various dimensionless channel half heights, H, and representative values of α. F_s it the Stokes drag on a sphere in unbounded flow.

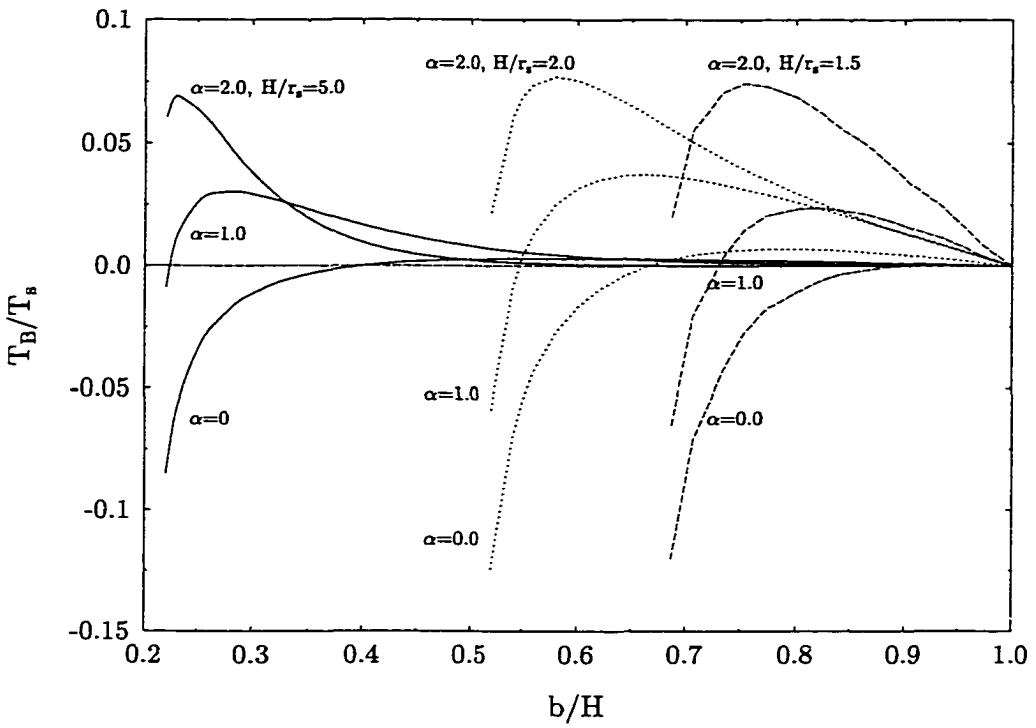

Figure 4.8: Normalized torque on a sphere moving in a channel for various dimensionless channel half heights, H, and representative values of α. T_s is the torque on a sphere rotating in unbounded Stokes flow.

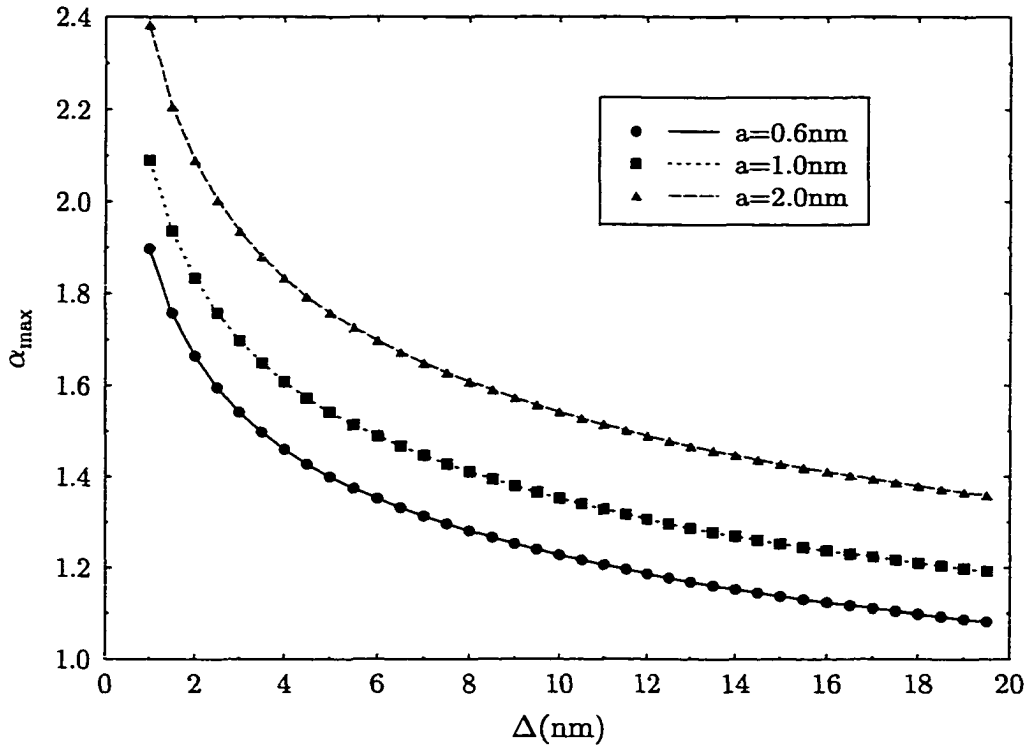

Figure 4.9: Variation of the maximum value of dimensionless permeability parameter α_{max} with respect to the gap between adjacent fibers for three different values of fiber radii.

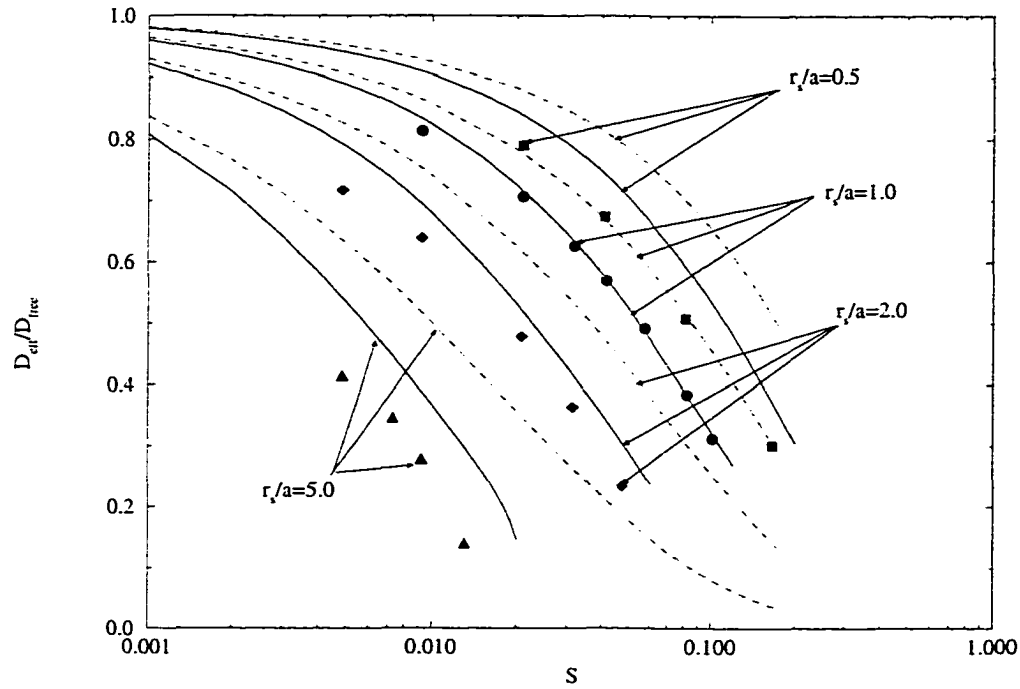

Figure 4.10: Comparison of the normalized diffusion coefficient obtained by a simple multiplicative formula (4.5.14), solid lines, and data points (symbols) obtained using Stokesian dynamics simulation for a sphere moving in an unbounded fiber-filled medium. Also shown, dashed lines, are the results for effective medium theory without the steric exclusion factor $F(S)$ in (4.5.14).

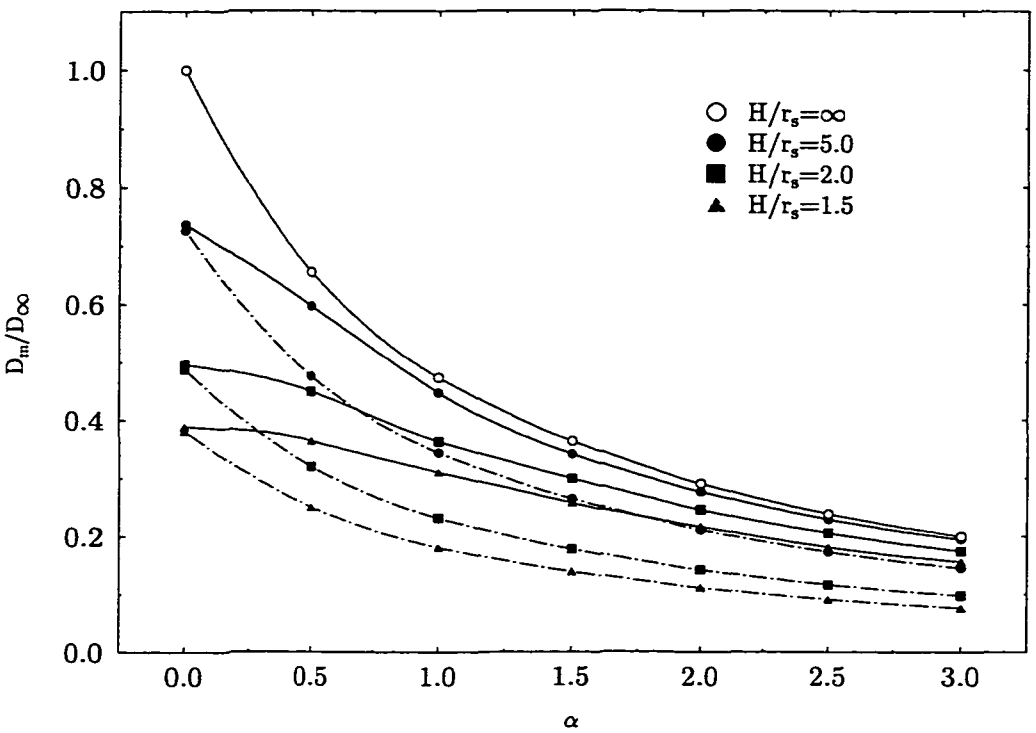

Figure 4.11: Comparison of the normalized diffusion coefficient obtained by the present numerical method (4.5.12)(solid lines), and simple multiplicative formula (4.5.12)(dashed-dot lines), for a sphere diffusing in a fiber-filled channel of various dimensionless channel half heights H.

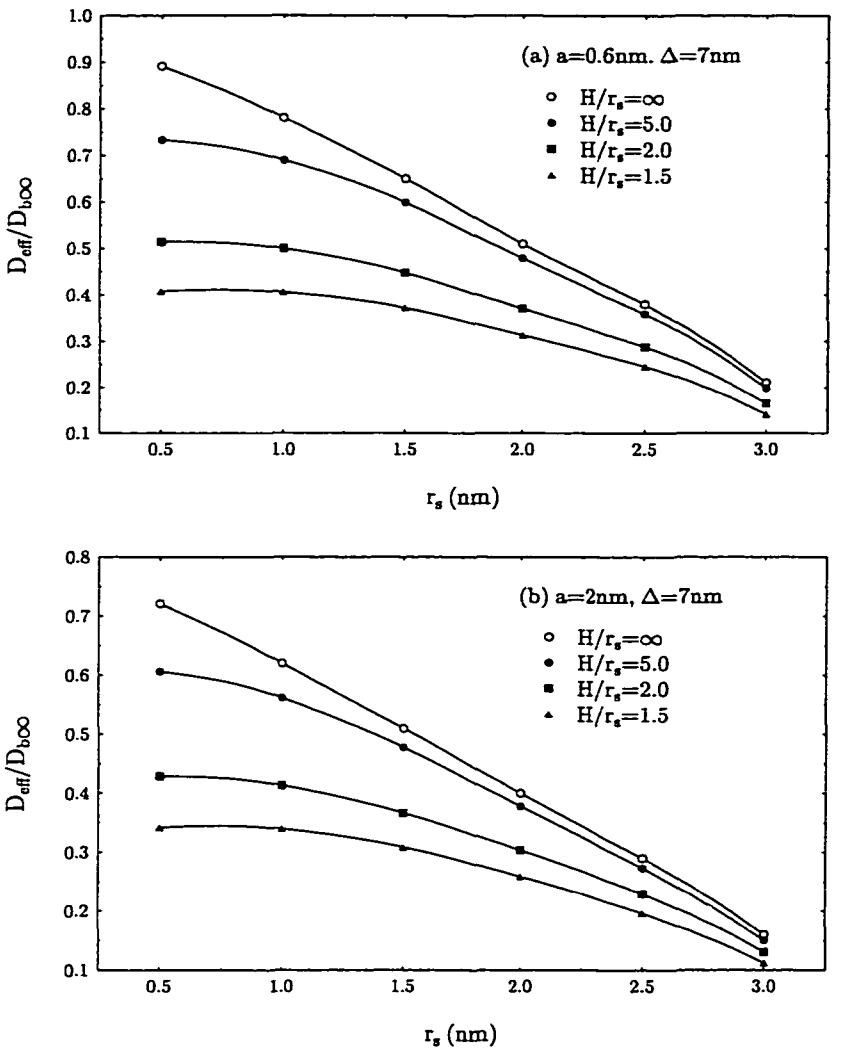

Figure 4.12: Normalized diffusion coefficient obtained by present numerical method for a sphere of radius r_s diffusing in a fiber-filled medium in a channel of various channel half heights H including the steric correction for a periodic fiber array given by equation (4.5.14). $D_{b\infty}$ is the Brinkman result for an infinite medium without the steric correction function $F(S)$.

d/r_s		$\alpha = 0.0$		$\alpha = 0.1$		$\alpha = 1.0$		$\alpha = 10.0$	
		F_z	T_y	F_z	T_y	F_z	T_y	F_z	T_y
1.05	(a)	0.733	1.11×10^{-1}	0.765	1.26×10^{-1}	0.946	1.77×10^{-1}	1.082	4.64×10^{-2}
	(b)			0.769	1.29×10^{-1}	0.948	1.79×10^{-1}	1.084	4.66×10^{-2}
1.5	(a)	0.795	6.41×10^{-2}	0.838	7.21×10^{-2}	1.018	5.40×10^{-2}	1.023	1.19×10^{-5}
	(b)			0.839	7.24×10^{-2}	1.020	5.44×10^{-2}	1.024	1.21×10^{-5}
2.0	(a)	0.839	3.88×10^{-2}	0.889	4.27×10^{-2}	1.026	1.41×10^{-2}	1.008	2.86×10^{-6}
	(b)	0.839	3.89×10^{-2}	0.890	4.29×10^{-2}	1.027	1.43×10^{-2}	1.009	2.88×10^{-6}
3.0	(a)	0.888	1.84×10^{-2}	0.942	1.90×10^{-2}	1.012	1.16×10^{-3}	1.001	5.62×10^{-7}
	(b)	0.888	1.84×10^{-2}	0.942	1.91×10^{-2}	1.013	1.17×10^{-3}	1.001	5.64×10^{-7}
5.0	(a)	0.930	6.97×10^{-3}	0.982	5.98×10^{-3}	1.002	1.19×10^{-5}	1.000	7.32×10^{-8}
	(b)	0.930	6.98×10^{-3}	0.982	5.99×10^{-3}	1.002	1.21×10^{-5}	1.000	7.34×10^{-8}

Table 4.1: Comparison of the drag and torque coefficients normalized by the single sphere result for two spheres moving perpendicular to their line of centers. (a) Results using the present boundary integral equation method with a total of 64 elements; (b) Results using the exact solution of Goldman, Cox & Brenner (1966) for $\alpha = 0$, or results using the boundary collocation technique of Gluckman *et al.* (1971) described in the text with a total of 32 boundary collocation points for $\alpha \neq 0$.

(a) $\alpha = 0.0$

No. of Elements	$b/r_s = 2.5$	$b/r_s = 2.0$	$b/r_s = 1.5$	$b/r_s = 1.2$	$b/r_s = 1.1$
12/12/12	1.590	1.826	2.347	3.182	3.760
24/24/24	1.598	1.836	2.365	3.222	3.916
32/32/32	1.600	1.839	2.369	3.230	3.933
64/64/64	1.600	1.839	2.370	3.233	3.939
Ganatos *et al.*		1.846	2.377		3.94

(b) $\alpha = 1.0$

No. of Elements	$b/r_s = 2.5$	$b/r_s = 2.0$	$b/r_s = 1.5$	$b/r_s = 1.2$	$b/r_s = 1.1$
12/12/12	2.346	2.536	2.996	3.783	4.436
24/24/24	2.361	2.554	3.022	3.831	4.506
32/32/32	2.365	2.558	3.028	3.842	4.526
64/64/64	2.366	2.559	3.030	3.846	4.531

Table 4.2: Convergence of the normalized drag F^t scaled by the Stokes drag $6\pi\mu U_0 r_s$ for a sphere translating in the middle of a channel parallel to the walls.

Chapter 5 Lubrication Theory in Highly Compressible Porous Media: The Mechanics of Skiing from Red Cells to Humans

5.1 Introduction

In this paper we shall present the detailed development of a new type of lubrication theory based on an effective medium approach (Brinkman equation) that is applicable to highly deformable porous layers. In particular, we shall want to look into the limit where the porous structure is so compressible that the normal forces generated by elastic compression of the fibers comprising the solid phase are negligible compared with the pressure force generated within the porous layer and the deformation of the solid phase is primarily due to boundary compression as opposed to the motion of the fluid phase. The most important new feature that we wish to capture in the model is the large non-linearity that results from order of magnitude spatial variations in Darcy permeability that arise from the large amplitude deformations of the fiber matrix. We shall show that the lift forces generated in such layers can be orders of magnitude larger than the lift forces generated in classical lubrication theory. Existing lubrication analyses have been limited to either a pure fluid layer satisfying a classical Reynolds equation or mixture or biphasic theories where the matrix deformation is small enough to neglect the changes in Darcy permeability due to the compression.

The initial motivation for this study grew out of several fundamental questions relating to the role of the thin fiber matrix layers that surround cells in an *in vivo* fluid environment, see Weinbaum (1998). One of the most important of these layers is the endothelial glycocalyx, a negatively charged layer of glycoproteins and proteoglycans that uniformly coats the luminal surface of vascular endothelium. This layer has been estimated to vary

from 0.1μm in *in vitro* studies of frog mesentery capillaries, Adamson & Clough (1992), to 0.4μm in *in vivo* studies of hamster cremaster microvessels, Vink & Duling (1996). From a hydrodynamic viewpoint this layer can be thought of as a hydrated gel, whose fiber volume fraction has been theoretically estimated to be between 1 and 2 percent. (Curry, 1986; Weinbaum *et al.* 1992). This extracellular layer has recently been proposed to be the primary molecular filter or osmotic barrier that determines the Starling forces that act across vascular endothelium (Michel 1997; Weinbaum 1998; Hu & Weinbaum 1999). To serve this function the barrier must exclude albumin (7nm in diameter) and other plasma proteins. Since numerous permeability studies in many tissues have shown that the reflection coefficient approaches 1.0 as the solute size approaches that of albumin the open gap between fibers has generally been assumed to be close to 7 nm, at least in the sieving part of the layer.

One of the great mysteries in the microcirculation is how the cellular components of blood, the red and white cells, are able to traverse the microvessels without undergoing constant molecular interaction with the plasmalemma membranes of the endothelial cells forming the vascular surface. In the case of the mammalian red cell, 8μm diameter cells are easily able to squeeze through 5-6 μm true capillaries with a separation distance near the wall that is typically 0.4 to 0.5 μm when the cells are moving at normal speed, Vink & Duling (1996). However, this separation distance appears to essentially vanish when the motion of the red cells is arrested, indicating that the matrix layer is highly deformable. In larger microvessels, where the red cells do not travel in single file, a similar separation distance is observed, Schmid-Schoenbein (1999). Here the red cells are also driven away from the plasmalemma boundaries by diffusion like forces generated by the shear induced migration of the red cells due to their hydrodynamic interaction, Leighton & Acrivos (1987). One of the most puzzling conundrums is the large difference in the *in vitro* and *in vivo* viscosity laws measured when the resistance of red cells in capillary networks is compared with their motion in small glass tubes (Pries *et al.* 1992, 1994). Significant differences start to appear for vessels smaller than 40 μm diameter which grow to an order of magnitude or more for

true capillaries. In the case of white cells the tips of the microvilli are known to be coated with adhesion molecules that promote the tethering and adhesive interaction of leukocytes with transmembrane receptors and ligands in the endothelial plasmalemma. The interaction of these microvilli with the endothelial glycocalyx is treated for the first time in Feng *et al.* (1998).

While these fundamental biological questions provided the initial motivation for the new theory proposed herein, the critical insights for understanding these phenomena arose from crude measurements by the senior author of the depth of ski tracks in freshly fallen snow at a ski resort in the northern Catskills. Nearly every experienced skier will tell you that skiing on fresh powder is like riding on air. Expert skiers achieve velocities that are 15 times their body height per second. However, this is small compared to the relative velocity that the red experiences in navigating through the microcirculation where a red cell can achieve a velocity that is more than 100 times its diameter per second. Both fresh snow and the endothelial glycocalyx share a common property that they are highly porous and easily compressed. Neither will support the compressive forces they are subjected to when the motion of the red cell or a skier is arrested. Snow will compress tenfold when it has to bear the static load due to the weight of the skier and, as noted above, a red cell will crush the surface glycocalyx and fill nearly the entire lumen of a microvessel due to the elastic restoring forces in its membrane and cytoskeleton when its motion is arrested. The crude measurement of the depth of the ski tracks readily confirmed that the skier could rise off the packed base and create a thin layer of partially compressed dry powder beneath the ski. Rough estimates of the lift forces predicted using a conventional lubrication theory based on a classical Reynolds equation indicate that such forces would support a weight of order 10 grams for a constrained air layer beneath the ski at small tilt angles. This is four orders of magnitude smaller than the weight of a 70 kilogram human being with his/her skis.

The forgoing observation suggested that there might be a striking similarity between a human skier gliding through fresh snow powder and the red cell skimming along the surface of the endothelial glycocalyx. In the case of snow the lift forces generated by the

porous media protect the bottom of our skies from the roughness of the surface beneath the powder and in the case of red cell the endothelial surface glycocalyx prevents molecular level adhesive interactions between the endothelial surface and the red cell membrane. This membrane can be thought of as a snow board and the red cell itself as an extraordinarily efficient skier. In both cases, we shall show that the pressure forces generated within the compressed porous layer are approximately four orders of magnitude greater than predicted by classical lubrication theory where the gap is filled with a pure fluid. However, the red cell is far more efficient since for the human skier or snow boarder much of the excess pressure that is built up beneath the planing surface leaks out the lateral edges of the ski or snowboard.

5.1.1 Previous Models for Red Cell Motion

Numerous models based on classical lubrication theory have been developed over the years to describe the motion of red cells in microvessels. Until 1995 the vessel wall was treated as a circular cylindrical tube without matrix. The red cells were initially modeled as rigid pellets (Lighthill 1968; Barnard 1968) or periodic arrays of spheres (Wang & Skalak 1969; Tozeren & Skalak 1978). More sophisticated models were then developed to predict the axisymmetric deformed shape of a moving cell using measured properties of the red cell membrane (Secomb & Gross 1983; Secomb *et al.* 1986). In the latter studies membrane shearing and bending stresses are treated within the framework of axisymmetric lubrication theory. It is only recently that the critical role of the endothelial surface glycocalyx in red cell motion has been recognized. The so called "sugar coat" of glycoprotein fibers was first identified by Luft (1964), but it was not until 1992 that Adamson & Clough (1992) clearly demonstrated *in vitro* that this coat was of nearly uniform thickness (0.1μm) and that this thickness depends on the proteins present in the perfusate. The first *in vivo* measurement of the glycocalyx in hamster cremaster microvessels by Vink & Duling (1996) indicated a significant thicker glycocalyx (0.4μm) than the electromicroscopic studies of Adamson & Clough, where the thickness could have been underestimated due to dehydration artifacts.

Vink & Duling also demonstrated that if the glycocalyx were non-invasively removed using epifluorescence, the red cell would fill the entire lumen. Perhaps most intriguing, if a red cell were started from rest it would exhibit a striking popout phenomenon in which it would quickly lift off the surface and then glide near the outer edge of the matrix layer.

The first models that attempted to take account of the matrix layer, Wang & Parker (1995) and Damiano *et al.* (1995), used lubrication and binary mixture theory to describe the motion of rigid particles in a circular tube whose walls were covered by a porous medium. In more recent analyses, Damiano (1998) and Secomb *et al.* (1998) have extended this model to a deformable cell without bending stiffness which moves within the fluid core. Damiano assumes a thin pure fluid layer exists between the edge of the glycocalyx and the red cell membrane, whereas Secomb *et al.* assume a value for K_p that varies with distance from the wall and vanishes in the fluid core. This model allows for the penetration of the matrix but not its compression. The presence of a matrix free fluid layer between the red cell and the glycocalyx provides a low resistance pathway for the relaxation of the pressure in the matrix and the new phenomena described in this paper are absent. No previous model has attempted to describe the penetration of the red cell into a compressible matrix or the popout phenomenon wherein the cell rises off the wall at low velocity. Furthermore, the zero drag condition, which describes the global force balance on the red cell, must be modified to take account of the integrated distributed force of the fibers.

5.1.2 Skiing and Snowboarding

To our knowledge this is the first time that the mechanics of skiing or snowboarding has been approached from viewpoint presented in this paper. The theory in its present form is most applicable to a thin layer of compressed fresh powder on a packed base. There is an extensive literature on the hydrodynamics of water skiing or planing on a free surface. The fundamental lift mechanism in the latter application is inertial and not viscous and the lift forces are generated by the momentum of the fluid that is pushed ahead of the planing

surface. This mechanism might be operative in snow plowing or turning, where the edges of the skies are turned into the snow, but it is intuitively clear that large lift forces can not be generated by the inertia of the snow in the normal skiing position because of the low angle of attack relative to the snow surface and the fact that the density of the snow is only about a tenth that of water. On the other hand, the viscous lift forces predicted by classical lubrication theory, as noted previously, would be several orders of magnitude too small. In the new theory two mechanisms contribute to the tremendous increase in the lift force and the pressure distribution under the ski. One is the large increase in the resistance of the air due to the fact that it is literally pushed and dragged through the porous solid. The resulting velocity profiles and streamlines depart dramatically from those in classical lubrication theory. The second is the compression of the soft powder which greatly increases the fluid resistance and the lift force acting at the back of the ski. By slightly adjusting the angle of tilt the skier can regulate the center of pressure and come to an equilibrium position where moments due to gravity and pressure cancel each other. In skiing or snowboarding the snow will compress and the permeability parameter α will increase until the lift force is just sufficient to balance the gravitational force.

The fundamental difference between the red cell gliding on the endothelial glycocalyx and the human skier is the pressure relaxation that occurs at the lateral edges of the skis. This pressure loss is characterized by a second parameter that appears in the governing equation, namely the aspect ratio L/W of the ski or snowboard. For the same value of α, the dimensionless lift forces will be at least two orders of magnitude lower than for the red cell. This is compensated for by a greater density of the matrix. For the endothelial glycocalyx the estimated volume fraction of the sialyic acid side chains in the undeformed solid phase is approximately one to two percent and is unlikely to increase much beyond 10 percent during compression. This is an order of magnitude smaller than the fibers that form the crystals in a snow flake.

5.1.3 Deformation of the Porous Media

In mixture theory, which has been applied to the artery wall (Kenyon 1979) or articular cartilage (Mow & Lai, 1980; Hou *et al.* 1991), there is a governing equation for the solid phase which relates the deformation of the porous matrix to the fluid flow. In the present approach we shall propose a much simplified model for the elastic deformation of the solid matrix phase based on the fact that this deformation is assumed to occur primarily due to the normal compressive force between the confining boundaries and not the fluid force on the matrix elements. This is a good approximation for the endothelial glycocalyx since the experiments have shown that the matrix is not disrupted even by the tightly fitting white cell and that the glycocalyx quickly rebounds to its initial thickness after the passage of the cell (Vink & Duling 1996). In the case of the snow the solid phase moves due to the pressure gradient established by the motion of the air, but this velocity is small compared to that of the air that passes through the porous medium both because of packing and the large difference in the density of the two phases.

The simplified model that we have constructed for the fibrous network lining the vasculature assumes that these fibers form a two-dimensional, diamond shaped, parallel array perpendicular to the flow direction. The matrix compresses linearly with gap height in the normal direction, but in planes parallel to the lower boundary the fiber spacing remains unchanged since there is negligible compression in the lateral direction. In this simplified model, the Darcy permeability is a function of just two dimensionless geometric parameters, the aspect ratio of the periodic fiber array and the ratio of the initial undeformed fiber spacing and the fiber radius. The local hydrodynamic resistance, or Darcy permeability, is then calculated using creeping flow theory. This simple model retains the essential physics of the compression process, and is a reasonable approximation to the much more complicated three-dimensional fiber structure of the surface glycocalyx about which little is presently known. For snow, no attempt is made to model the hexagonal crystal structure of the snow flake, and the model is intended only as a rough guide in estimating the local value of the

dimensionless permeability parameter α, defined as $H/\sqrt{K_p}$, where H is the undeformed characteristic layer thickness and K_p the Darcy permeability, that appears in the Brinkman equation.

The paper is organized into seven sections. In section 5.2, a new Reynolds type equation is derived for highly compressible porous media in which the Darcy permeability is spatially varying. Two new parameters appear in this analysis which do not arise in classical lubrication theory, where the only parameters are the Reynolds number Re and the slope of the boundaries. These parameters are the dimensionless permeability parameter α and the aspect ratio of the upper boundary. In section 5.3 we develop the theory for predicting the spatial variation of the local Darcy permeability. In section 5.4 we simplify the governing equation for a one-dimensional planar surface where we assume there is no lateral leakage of pressure. The resulting highly non-linear differential equation is solved for large deformations to show the effects of both varying the slope of the moving boundary and the permeability parameter α. Results are shown for the pressure distribution, lift force, velocity profiles and the streamline pattern. In section 5.5 we generalize these results for two-dimensional planar surfaces with lateral edges as a model for skiing and snowboarding. In section 5.6 we first derive a new global force balance for the zero drag condition on the cell and then examine the pressure drop and apparent viscosity for axisymmetric rigid models of red cells to provide new insight into the *in vivo* viscosity law of Pries *et al.* (1994). Concluding comments and future directions are given in section 5.7.

5.2 Lubrication Theory for the Porous Layer

Classical lubrication theory was initially developed by Reynolds for incompressible, Newtonian fluid (Schlichting 1954). This was subsequently generalized for Newtonian fluids with variable properties and non-Newtonian fluids. The theory has been applied to both impermeable and porous stationary and moving journal-bearing systems. In biological applications, where the stresses are associated with the compression of a porous solid phase,

biphasic mixture theory has been extensively used to described cartilage, Mow & Lai (1980), and more recently the glycocalyx (Wang & Parker 1995; Damiano 1998; Secomb *et al.* 1998). In most of these previous analyses the deformation of the porous matrix is sufficiently small for the Darcy permeability to remain constant. As a result, the velocity profile in the lubricating layers depends only on the local value of the pressure gradient and boundary velocity. However, as the porous layer, which in the present application is either the endothelial surface glycocalyx or fresh snow powder, is compressed by the moving cell membrane or ski, respectively, the change of the Darcy permeability K_p can be huge. As will be shown later, this can lead to dramatic changes in the pressure distribution in the matrix compared to the constant Darcy permeability case for large compressions. Therefore, in the present model, a simplified anisotropic fiber matrix model is developed to account for the local variation of the matrix permeability. Consequently, an additional parameter, which depends on the local matrix height, appears in the new Reynolds-type equation derived using effective medium theory. For two-dimensional lubricating layer theory, which is required for studying the mechanics of skiing or snow boarding, the geometric aspect ratio will also play an important role.

For the general case, we consider a two-dimensional rigid boundary moving arbitrarily with velocity $\boldsymbol{U} = (U_x, U_x, U_z)$ in Cartesian coordinates over a fibrous matrix which is thin compared to the characteristic dimensions of the moving boundary in the x and y directions. The local matrix height is denoted by $h(x, y)$. Note that $\boldsymbol{U}$ and h can not be specified independently, because there is a simple Eulerian relationship between them:

$$U_z = \frac{\partial h}{\partial t} + U_x \frac{\partial h}{\partial x} + U_y \frac{\partial h}{\partial y}. \tag{5.2.1}$$

Nevertheless, it it convenient to treat $\boldsymbol{U}$ and h as though they were independent.

The effective medium theory for flow in a fiber layer is described by the Brinkman

equation (Brinkman 1947; Feng *et al.* 1998)

$$\mu\left(\nabla^2 - \frac{1}{K_p}\right)\boldsymbol{u} = \nabla p \tag{5.2.2}$$

which can be derived either by renormalization of the Stokes flow in a periodic microscopic domain or by averaging the Stokes equation for flow in a random assemblage of spherical particles (Howells 1974; Tam 1969; Lundgren 1972). Recently, Howells (1998) studied flow through randomly distributed fibers by a renormalization technique and recovered the Brinkman equation at the leading order. Feng *et al.* (1998) have developed a boundary integral equation method for bounded particle motion in a Brinkman medium and have applied the results to several biological problems in cellular mechanics and transendothelial transport. The validity and accuracy of the Brinkman equation in bounded porous media is also addressed in Tsay & Weinbaum (1991) and Feng *et al.* (1998).

We introduce the dimensionless primed coordinates, velocities and pressure as

$$x' = \frac{x}{L}, \qquad y' = \frac{y}{W}, \qquad z' = \frac{z}{H}, \tag{5.2.3}$$

$$u' = \frac{u}{U_c}, \quad v' = \frac{v}{V_c}, \quad w' = \frac{w}{W_c}, \quad p' = \frac{p}{P_c}, \tag{5.2.4}$$

where L and W are the characteristic lengths of the moving surface in the x and y directions. For a ski or a snow board, L and W are its length and width, respectively. H is the undeformed matrix gap height. In these dimensionless variables, the continuity equation in Cartesian coordinates is rewritten as

$$\frac{\partial u'}{\partial x'} + \frac{V_c}{U_c}\frac{L}{W}\frac{\partial v'}{\partial y'} + \frac{W_c}{U_c}\frac{L}{H}\frac{\partial w'}{\partial z'} = 0. \tag{5.2.5}$$

For the coefficient of the dimensionless pressure gradient in the x, y and z directions to be unity, we choose the characteristic velocities as

$$U_c = U_x, \qquad V_c = \frac{L}{W}U_x, \qquad W_c = \frac{H}{L}U_x, \tag{5.2.6}$$

and define the characteristic pressure P_c as

$$P_c = \frac{\mu L U_x}{H^2}. \tag{5.2.7}$$

With these definitions of the characteristic velocities and pressure, the three components of the Brinkman equation in (5.2.2) in Cartesian coordinates can be written as

$$\frac{\partial p'}{\partial x'} = \left(\epsilon_x^2 \frac{\partial^2}{\partial x'^2} + \epsilon_y^2 \frac{\partial^2}{\partial y'^2} + \frac{\partial^2}{\partial z'^2} - \alpha^2\right) u', \tag{5.2.8}$$

$$\frac{\partial p'}{\partial y'} = \left(\epsilon_x^2 \frac{\partial^2}{\partial x'^2} + \epsilon_y^2 \frac{\partial^2}{\partial y'^2} + \frac{\partial^2}{\partial z'^2} - \alpha^2\right) v', \tag{5.2.9}$$

$$\frac{\partial p'}{\partial z'} = \epsilon_x^2 \left(\epsilon_x^2 \frac{\partial^2}{\partial x'^2} + \epsilon_y^2 \frac{\partial^2}{\partial y'^2} + \frac{\partial^2}{\partial z'^2} - \alpha^2\right) w', \tag{5.2.10}$$

where $\epsilon_x = H/L$, $\epsilon_y = H/W$ and K_p is the Darcy permeability parameter α defined by

$$\alpha = \frac{H}{\sqrt{K_p}}. \tag{5.2.11}$$

If we assume that both $\epsilon_x << O(1)$ and $\epsilon_y << O(1)$, then it is clearly seen from (5.2.8)-(5.2.10) that the pressure gradient in the vertical direction is $O(\epsilon_x^2)$ smaller than that in either lateral direction. Thus we assume that the pressure is a constant across the matrix layer, i.e. $p = p(x, y)$, and to $O(\epsilon_x^2)$ or $O(\epsilon_y^2)$ equations (5.2.8) and (5.2.9) reduce to equations similar to those obtained in classical lubrication theory (prime omitted for brevity)

$$\frac{\partial p}{\partial x} = \left(\frac{\partial^2}{\partial z^2} - \alpha^2\right) u, \tag{5.2.12}$$

$$\frac{\partial p}{\partial y} = \left(\frac{\partial^2}{\partial z^2} - \alpha^2\right) v. \tag{5.2.13}$$

These equations in conjunction with the dimensionless continuity equation

$$\frac{\partial u}{\partial x} + \frac{L^2}{W^2}\frac{\partial v}{\partial y} + \frac{\partial w}{\partial z} = 0 \tag{5.2.14}$$

determine the flow within the thin layer of fiber matrix.

Solutions to (5.2.12) and (5.2.13) which satisfy the no slip boundary conditions at $z = 0$ and $z = h$ are given by

$$u = \frac{\sinh \alpha z}{\sinh \alpha h} + \frac{1}{\alpha^2}\frac{\partial p}{\partial x}\left[\cosh \alpha z - 1 - \frac{\sinh \alpha z}{\sinh \alpha h}(\cosh \alpha h - 1)\right] \tag{5.2.15}$$

$$v = \frac{W}{L}\frac{U_y}{U_x}\frac{\sinh \alpha z}{\sinh \alpha h} + \frac{1}{\alpha^2}\frac{\partial p}{\partial y}\left[\cosh \alpha z - 1 - \frac{\sinh \alpha z}{\sinh \alpha h}(\cosh \alpha h - 1)\right]. \tag{5.2.16}$$

Note that in view of the definition of V_c in (5.2.4), v at $z = h$ is given by $(W/L)(U_y/U_x)$. The corresponding fluxes in the x and y directions are computed by integrating over the local dimensionless channel height, i.e.

$$Q_x = \int_0^h u dz = f(\alpha, h) + \frac{1}{\alpha^2}\frac{\partial p}{\partial x}(2f(\alpha, h) - h), \tag{5.2.17}$$

$$Q_y = \int_0^h v dz = \frac{W}{L}\frac{U_y}{U_x} f(\alpha, h) + \frac{1}{\alpha^2}\frac{\partial p}{\partial y}(2f(\alpha, h) - h), \tag{5.2.18}$$

in which

$$f = \frac{\cosh \alpha h - 1}{\alpha \sinh \alpha h}. \tag{5.2.19}$$

If we integrate the continuity equation (5.2.5) over the channel height, apply the Newton-Leibnitz rule for differentiating an integral with variable limits

$$\frac{\partial Q_x}{\partial x} = \int_0^{h(x,y)} \frac{\partial u}{\partial x} dz + \frac{\partial h(x,y)}{\partial x}, \tag{5.2.20}$$

treat $\frac{\partial Q_y}{\partial y}$ in a similar manner, and satisfy the dimensionless boundary conditions

$$U_x'(x, y, h) = 1, \quad U_y'(x, y, h) = \frac{W}{L}\frac{U_y}{U_x}, \quad U_z'(x, y, h) = \frac{L}{H}\frac{U_z}{U_x}, \tag{5.2.21}$$

we obtain

$$\frac{\partial Q_x}{\partial x} + \frac{L^2}{W^2}\frac{\partial Q_y}{\partial y} = -\frac{U_z}{\epsilon_x U_X} + \frac{\partial h}{\partial x} + \frac{L}{W}\frac{U_y}{U_x}\frac{\partial h}{\partial y}, \tag{5.2.22}$$

where the prime has been dropped for convenience. Inserting the definitions (5.2.17) and (5.2.18) in (5.2.22), one obtains a generalized Reynolds equation for a Brinkman medium

$$\frac{\partial}{\partial x}\left[f+\frac{1}{\alpha^2}\frac{\partial p}{\partial x}(2f-h)\right]+\frac{L^2}{W^2}\frac{\partial}{\partial y}\left[\frac{W}{L}\frac{U_y}{U_x}f+\frac{1}{\alpha^2}\frac{\partial p}{\partial y}(2f-h)\right]=\frac{\partial h}{\partial x}+\frac{L}{W}\frac{U_y}{U_x}\frac{\partial h}{\partial y}-\frac{1}{\epsilon_x}\frac{U_z}{U_x}. \tag{5.2.23}$$

In the limit $\alpha \to 0$,

$$f \to \frac{h}{2}-\frac{\alpha^2 h^3}{24},$$

and equation (5.2.23) reduces to the classical Reynolds equation for an incompressible, Newtonian viscous fluid,

$$\frac{\partial}{\partial x}\left[6h-h^3\frac{\partial p}{\partial x}\right]+\frac{L^2}{W^2}\frac{\partial}{\partial y}\left[6\frac{W}{L}\frac{U_y}{U_x}h-h^3\frac{\partial p}{\partial y}\right]=12\left[\frac{\partial h}{\partial x}+\frac{L}{W}\frac{U_y}{U_x}\frac{\partial h}{\partial y}-\frac{1}{\epsilon_x}\frac{U_z}{U_x}\right] \tag{5.2.24}$$

The lateral velocity components are given by (5.2.15) and (5.2.16). The vertical velocity component w is calculated from the dimensionless continuity equation (5.2.14).

In the case of one-dimensional flow, where $\boldsymbol{U}=u_x\boldsymbol{i}$ and there is no flow leakage in the y direction, equation (5.2.23) reduces to

$$\frac{d}{dx}\left[f+\frac{1}{\alpha^2}\frac{dp}{dx}(2f-h)\right]=\frac{dh}{dx}. \tag{5.2.25}$$

This one-dimensional equation is suitable for describing the gliding motion of a red cell membrane over the endothelial glycocalyx. Equation (5.2.25) is non-linear since K_p and hence α is a non-linear function of the lateral coordinates if large compressions of the matrix are considered. K_p is determined from the solution of equations (5.3.2) and (5.3.3), which is presented in the next section.

The modified Reynolds equation (5.2.25) can be solved for the pressure distribution using the appropriate boundary conditions. Once the pressure field is determined, the flow field, the lift force and the drag exerted on the moving membrane can be calculated. These results, together with new features, which are absent for a pure fluid layer, are discussed in

subsequent sections.

5.3 Permeability of the Porous Layer

In this section, we propose a simplified model for the local change in Darcy permeability that is suitable for both the endothelial glycocalyx and the flexible crystalls comprising snow powder. A schematic illustration of the geometry of the model for the sliding motion of a planar membrane over a thin fiber matrix layer is shown in Fig. 5.1(A). For simplicity, we model this surface matrix as a doubly periodic fiber array with lateral and vertical fiber spacings Δ_1 and Δ_2, see Fig. 5.1(C, D). The Darcy permeability K_p of the matrix depends upon the fiber radius a and the spacing, which varies with position as a result of the non-uniform compression.

The simplified model that we have constructed for the compression of the fibrous network assumes that the fibers in the matrix form a periodic two-dimensional, diamond or rectangular shaped, parallel array perpendicular to the flow direction that compresses linearly with change in gap height, $H - h$, in the vertical direction. Thus, in planes parallel to the lower boundary the fiber spacing Δ_1 remains unchanged, since there is negligible compression in the lateral direction and only Δ_2 changes with the local deformation. Thus,

$$\frac{h}{H} = \frac{2a + \Delta_2}{2a + \Delta_{2H}}, \tag{5.3.1}$$

where Δ_2 and Δ_{2H} are the deformed and initial vertical fiber spacing, respectively. This type of matrix deformation is reasonable when the solid phase deforms due to the relative boundary motion rather than drag forces arising from the motion of the fluid phase. The motion of the solid phase is neglected. This is a realistic approximation for the endothelial glycocalyx and a reasonable approximation for skiing since the velocity of the skis far exceeds that of the snow powder.

The flow past this periodic, diamond, Fig. 5.1(C), or rectangular, Fig. 5.1(D), shaped

fiber array is described by the two-dimensional Stokes equations written in terms of the stream and vorticity functions

$$\nabla^2\psi = \omega, \tag{5.3.2}$$

$$\nabla^2\omega = 0. \tag{5.3.3}$$

For the diamond shaped fiber array in Fig. 5.1(C), the boundary conditions are

$$\psi = \omega = 0, \qquad \text{on BC} \tag{5.3.4}$$

$$\frac{\partial\omega}{\partial x} = \frac{\partial\psi}{\partial x} = 0, \qquad \text{on GH, CD} \tag{5.3.5}$$

$$\omega = 0, \quad \psi = U\left(a + \frac{\Delta_2}{2}\right), \qquad \text{on FG} \tag{5.3.6}$$

In addition, because of the no slip condition on the fiber post, we require that

$$\psi = \frac{\partial\psi}{\partial n} = 0, \qquad \text{on BH} \tag{5.3.7}$$

$$\psi = U\left(a + \frac{\Delta_2}{2}\right), \quad \frac{\partial\psi}{\partial n} = 0, \qquad \text{on DF} \tag{5.3.8}$$

in which U is the mean velocity in the x direction and $\boldsymbol{n}$ is the outer normal unit vector. For the rectangular fiber array arrangement depicted in Fig. 5.1(D), the corresponding boundary conditions are given by

$$\psi = \omega = 0, \qquad \text{on BC} \tag{5.3.9}$$

$$\frac{\partial\psi}{\partial x} = \frac{\partial\omega}{\partial x} = 0, \qquad \text{on CE and GE} \tag{5.3.10}$$

$$\omega = 0, \quad \psi = U\left(a + \frac{\Delta_2}{2}\right), \qquad \text{on GE} \tag{5.3.11}$$

$$\psi = \frac{\partial\psi}{\partial n} = 0, \qquad \text{on BH} \tag{5.3.12}$$

Once the solution for the stream function and vorticity, ψ and ω, are obtained, the

dimensionless drag exerted on any given fiber per unit length is given by

$$\frac{F}{\mu U} = a\int_0^{2\pi}[\omega\sin\theta - p\cos\theta]d\theta, \tag{5.3.13}$$

The Darcy permeability is readily calculated by applying the force balance on a unit cell. This leads to

$$\frac{K_p}{a^2} = \frac{\pi}{c}\frac{\mu U}{F}, \tag{5.3.14}$$

where c, the solid fiber fraction is given by

$$c = \frac{2\pi a^2}{(2a+\Delta_1)(2a+\Delta_2)}. \tag{5.3.15}$$

The dimensionless permeability parameter α in the Brinkman equation is, therefore, given by

$$\alpha = \frac{H}{\sqrt{K_p}} = \frac{H}{a}\sqrt{\frac{Fc}{\mu U\pi}}. \tag{5.3.16}$$

The pressure p is obtained by integrating the coupled relations

$$\frac{\partial p}{\partial x} = \mu\frac{\partial\omega}{\partial y}, \tag{5.3.17}$$

$$\frac{\partial p}{\partial y} = -\mu\frac{\partial\omega}{\partial x}. \tag{5.3.18}$$

In our calculations, equations (5.3.2)-(5.3.3) are solved by a least square boundary collocation technique that is applied to the periodic unit cells sketched in Fig. 5.1(C) and (D). Following Sangani & Acrivos (1982), we can write general solutions to (5.3.2) and (5.3.3) as[1]

$$\begin{aligned}\omega &= 2\left(4a_1 r - \frac{(4a_1+2b_1)a^2}{r(2\ln a+1)}\right)\sin\theta + 8\sum_{n=2}^{\infty}\sin(2n-1)\theta \\ &\times\ [na_n r^{2n-1} + (n-1)a^{4n-2}r^{1-2n}(2na_n - (2n-1)b_n)],\end{aligned} \tag{5.3.19}$$

[1]Note there is a typographical error in Eq. [11] in Sangani & Acrivos (1982)

and

$$\begin{aligned}\psi &= \left[a_1 r^3\left\{1-\frac{4\ln r}{2\ln a+1}\left(\frac{a}{r}\right)^2+\frac{2\ln a-1}{2\ln a+1}\left(\frac{a}{r}\right)^4\right\}+b_1 a^2 r\left\{1-\frac{2\ln r}{2\ln a+1}\right.\right.\\ &- \left.\left.\frac{1}{2\ln a+1}\left(\frac{a}{r}\right)^2\right\}\right]\sin\theta+\sum_{n=2}^{\infty}\left[a_n r^{2n+1}\left\{1-2n\left(\frac{a}{r}\right)^{4n-2}+(2n-1)\left(\frac{a}{r}\right)^{4n}\right\}\right]\\ &+ b_n a^2 r^{2n-1}\left\{1-(2n-1)\left(\frac{a}{r}\right)^{4n-4}+2(n-1)\left(\frac{a}{r}\right)^{4n-2}\right\}\Bigg]\sin(2n-1)\theta. \quad (5.3.20)\end{aligned}$$

Equations (5.3.19) and (5.3.20) are expressed in the cylindrical coordinates so that the boundary conditions on BC, GH and BH can be satisfied exactly. The unknown coefficients a_n and b_n are determined by applying the remaining boundary conditions in some approximate sense. This is accomplished by a least square collocation technique adopted in Sangani & Acrivos (1982). We first select a sufficient number of collocation points on either CD, DF and FG for the diamond fiber array, or on CE and EG for the square fiber array, respectively. The boundary conditions are satisfied at discrete points along these remaining boundaries and the resulting linear algebraic equations for a_n and b_n are determined in a least square sense. The results converge as the number of collocation points increases. We have also solved the biharmonic equation for the stream function using a boundary integral method and obtained results in good agreement with those presented herein.

The dimensionless force exerted on a fiber per unit length is obtained by evaluating the integral in (5.3.13) using equations (5.3.17) to (5.3.20). Note that $G(z) = G(x+iy) = p - i\psi$ is an analytic function so that

$$\frac{F}{\mu U} = -Im\int_{\gamma} G(z)dz = -2\pi Re[res(G(z))] \quad (5.3.21)$$

where $res(G)$ denotes the residues of $G(z)$ within the contour γ, defined by the closed curve $r = a$. It is apparent that both p and ψ have simple poles at $r = 0$ and $G(z)$ has a simple pole at $z = 0$. One finds that, as shown in Sangani & Acrivos (1982), that the dimensionless

drag per unit length

$$\frac{F}{\mu U} = -\frac{8\pi a^2(2a_1 + b_1)}{2\ln a + 1} \tag{5.3.22}$$

depends only on the two leading coefficients a_1 and b_1, although their values depend on all the other coefficients. The dimensionless Darcy permeability parameter α is given by (5.3.16).

In Figs. 5.2, 5.3 and 5.4 we present the results for both the deformed hexagonal and square fiber arrays. If the results for the fiber drag per unit length are written in terms of the fiber solid fraction c, $F/\mu U$ is independent of the fiber radius and is only a function of the aspect ratio of the fiber array λ. Thus in Fig. 5.2 we first present general results which are independent of the fiber radius. The fiber solid fraction for the undeformed hexagonal array is twice that of the square array. Fig. 5.2 plots the dimensionless drag $F/\mu U$ as a function of fiber solid fraction c defined by (5.3.15). These results extend the solutions presented in Sangani & Acrivos (1982) in which only results for $\lambda = (2a + \Delta_2)/(2a + \Delta_1)$ equal to $\sqrt{3}$, the undeformed hexagonal fiber array and $\lambda = 1$, the undeformed square array are presented. As the vertical fiber spacing decreases, the rectangular fiber arrangement experiences monotonically increasing drag on the fibers, as shown in Fig. 5.2(B). However, this is not true for a diamond shaped fiber array. Because the hexagonal fiber matrix is completely isotropic, the drag for $\lambda = \sqrt{3}$ and $\sqrt{3}/3$ should be the same. Thus, there must be a critical value of λ for which the drag reaches a maximum and the monotonic behavior with increasing λ can not be maintained. This is revealed in Fig. 5.2(A) where the result for $\lambda = 1$ almost overlaps with that for $\lambda = 0.5$.

For application in microcirculation, where a layer of endothelial glycocalyx seems to be ubiquitous, we calculated the Darcy permeability for a compressed initially hexagonal fiber array whose undeformed fiber spacing $\Delta_1 = 7$nm and $\Delta_2 = 13$nm. Two fiber radii, $a = 0.6$nm and $a = 2$nm are considered herein since they are representative of the sialyic acid side chains in glycosaminoglycans(GAG) and the protein core in proteoglycans, respectively.

The variation of the dimensionless drag as the fiber matrix is compressed vertically is

shown in Fig. 5.3(A) for the initially square and rotated square ($\pi/4$) fiber arrays when the initial fiber spacing, $\Delta_1 = 7$nm, $\Delta_2 = 7$nm for both arrays. Results are shown for two fiber radii, 0.6nm corresponding to GAG side chains and protein core, and 2nm, typical of protein. As expected the drag increases as Δ_2 decreases. The two sets of curves for a specific fiber radius a converge into a single curve for both arrays as the fiber spacing between adjacent vertical fibers narrows. This is anticipated since, if the fibers are sufficiently close to each other in the vertical direction, the horizontal spacing plays only a minor role in determining the drag exerted on each fiber. Therefore, in the dilute limit when Δ_1 remains fixed and Δ_2 becomes small, the Darcy permeability for a square fiber array will be twice that for a diamond shaped array. Fig. 5.4 exhibits the streamline patterns in a unit cell for the two fiber arrangements. It is clear that the streamlines are squeezed together as λ decreases. For this near contact case, Sangani & Acrivos (1982) have shown that the resistance can be described by a lubrication force which usually differs for square and hexagonal fiber arrays.

Fig. 5.3(B) shows the Darcy permeability for a deformed hexagonal fiber array in which the initial fiber spacings are $\Delta_1 = 7$nm and $\Delta_2 = 13$nm. Note that this fiber arrangement differs from our previous applications using the fiber matrix model (Weinbaum *et al.* 1992; Fu *et al.* 1994) in which the fiber array is obtained by rotating the square array through $\pi/4$ radians . Most of the calculations presented later in this paper are based on the Darcy permeability shown in Fig. 5.3(B) for the initially hexagonal fiber array which exhibits a strong non linear behavior as the matrix is compressed. As will be discussed later, this non-linearity will cause a shift in the pressure distribution and a large increase in the lift force on a moving surface at an attack angle for large matrix deformations.

5.4 One-Dimensional Analysis: Gliding Motion of a Membrane

In this section, we will apply the one-dimensional lubrication theory developed in section 5.2 to study the motion of a red cell membrane that penetrates the endothelial glycocalyx. We are also interested in a more general model for an arbitrary one-dimensional surface moving parallel to a fixed planar boundary. We shall show that for this case closed form solutions can be obtained for the pressure distribution for an arbitrary $h(x)$ provided the boundaries are not deformable. This analysis is a simplified model for many applications in compressible porous media where the leakage of the excess pressure at the lateral boundaries is unimportant. This simple model is also used to illustrate the fundmental new hydrodynamic features that are absent in classical lubrication theory. A related simplified model for an axisymmetric rigid red cell moving in a circular tube lined with a surface glycocalyx is presented in section 5.6.

We assume that the thickness of the fiber matrix in the fluid gap between the two surfaces is small compared to the characteristic length in the x direction. This is a reasonable model for a red cell membrane that comes in near contact with the endothelial surface in larger microvessels. We consider first the case of an arbitrary $h(x)$ and show that the one-dimensional Reynolds type equation (5.2.25) can be solved exactly. This exact solution will also be used to check the numerical method developed for solving the full two-dimensional equation discussed in the next section.

One notes that if the sliding velocity U is a constant, equation (5.2.25) can be integrated directly yielding the general solution

$$f + \frac{1}{\alpha^2}\frac{dp}{dx}(2f - h) = h + C, \tag{5.4.1}$$

where C is a constant. The constant C is evaluated by prescribing the leading and trailing edge pressures. If the pressures at the leading and trailing edges of the cell membrane are

the same and α is only a function of x, C can be expressed as

$$C = -\frac{\int_0^1 \frac{\alpha^2(h-f)}{2f-h}dx}{\int_0^1 \frac{\alpha^2}{2f-h}dx}. \tag{5.4.2}$$

The pressure distribution from (5.4.1)is given by

$$p - p_0 = \int_0^x \frac{\alpha^2(h-f+C)}{2f-h}dx, \tag{5.4.3}$$

where p_0 is the pressure at $x = 0$ and $x = 1$ if C is given by (5.4.2).

The total dimensionless lift force F is obtained by integrating (5.4.3) over the entire surface. This leads to

$$F = \int_0^1 (p - p_0)dx = \int_0^1 (1-x)\frac{\alpha^2(h-f+C)}{2f-h}dx, \tag{5.4.4}$$

where we have changed the order of integration in evaluating the double integral. The velocity components, flow patterns and drag force on the membrane can be calculated in a manner similar to that for classical lubrication theory. In general α will be a highly non-linear function of h as quickly surmised from Fig. 5.3(B). Once $h(x)$ is prescribed, equations (5.4.2) and (5.4.3) provide a remarkably simple solution for the pressure distribution in the compressed matrix layer for any $h(x)$. This will greatly facilitate the treatment of deformable surfaces using iterative methods.

To illustrate the general behavior, we performed numerical calculations for a simple example in which an inclined planar surface of length L moves at a constant velocity over a thin fiber matrix. The undeformed thickness of the matrix is assumed to be h_2 and the compression ratio k is defined by the ratio h_2/h_1, where h_1 is the compressed matrix thickness at the trailing edge. Typical solutions for the pressure distribution beneath this planar surface are shown in Fig. 5.5. Here the undeformed thickness h_2 and $\alpha(h_2)$ at the leading edge are prescribed. The slope of the plane $(h_2-h_1)/L$ is given in terms of the matrix

compression ratio, $k = h_2/h_1$, as $(1 - 1/k)h_2/L$, see Fig. 5.1. In Fig. 5.5(A), the pressure distribution for a moderately compressed matrix, $k = 4$, is plotted for several increasing values of the undeformed permeability parameter $\alpha(h_2)$. Also shown for comparison are the predictions of classical lubrication theory, the limiting case of Eq. 5.2.25 when $\alpha = 0$. It is observed that the pressure increases remarkably as $\alpha(h_2)$ increases from zero, a pure fluid layer, to $\alpha(h_2) = 100$. The pressure is generated within the matrix for $\alpha(h_2) = 100$ is three orders of magnitude greater than for $\alpha = 0$. Fig. 5.5(B) shows the change in the pressure distribution as the matrix compression ratio is increased when $\alpha(h_2) = 50$, a value representative of a 100nm thick endothelial glycocalyx. The maximum compression ratio is about 12. One notes that there is a pronounced shift in the maximum pressure towards the trailing edge for large values of k. The combined results in Fig. 5.5(A,B) lead to the dramatic increase in the integrated lift force shown in Fig. 5.6, where the dimensionless lift force is plotted as a function of k. We note that the total lift force on the moving surface increases as the compression ratio k increases due to the large increase in α as one approaches the trailing edge. This is in contrast to the well known result in classical lubrication theory for a slider bearing where the lift force is a maximum when $h_2 \approx 2.2h_1$ and h_1 is fixed.

It is also of interest to plot the position of the maximum pressure x_m/L as a function k for different values of $\alpha(h_2)$. This is shown in Fig. 5.7, where we notice that x_m/L exhibits a more complicated behavior. For small values of $\alpha(h_2)$, the maximum pressure is achieved closer to the midpoint than for $\alpha = 0$, the pure fluid layer. However, as $\alpha(h_2)$ increases there is a large shift in the position of the maximum pressure towards to the trailing edge of the plate as k increases. For the purpose of comparison, we have also calculated x_m/L if the matrix compression is neglected, i.e., $\alpha = \alpha(h_2)$ throughout the matrix. The results show that there is a much larger shift in the pressure maximum toward the trailing edge when matrix compression is considered. This is due to the large non-linearity in the Darcy permeability that develops as the matrix is compressed near the trailing edge. This gives rise to the large asymmetry in the pressure profile shown in Fig. 5.5. Fig. 5.7 also indicates

that x_m/L is nearly independent of $\alpha(h_2)$ once $\alpha(h_2)$ exceeds 20 for all values of k.

Fig. 5.8 illustrates the change in the streamline pattern as $\alpha(h_2)$ increases. One observes that for $\alpha = 0$ there is a small recirculation region near the trailing edge where the pressure gradient is negative. However, as $\alpha(h_2)$ increases a dividing streamline develops starting near the trailing edge and fluid is either expelled in front of the leading edge or ejected at the trailing edge of the moving surface. This behavior is more easily interpreted in terms of the velocity profiles exhibited in Fig. 5.9, where horizontal velocity profiles are presented at three positions, the leading edge $x/L = 1$, the trailing edge $x/L = 0$ and the position x_m/L, the pressure maximum. The velocity component is normalized relative to the sliding velocity U. In sharp contrast to a pure fluid layer, $\alpha = 0$, the horizontal velocity remains almost constant in the central region of the matrix for large values of α, except for a thin transition layer near the boundaries where the no slip condition must be satisfied. In fact, as the Darcy term becomes larger and dominates the effect of the viscous dissipation terms, the Brinkman medium reduces to a Darcy medium in which a uniform plug flow proportional to the local pressure gradient is anticipated. Therefore, the Brinkman medium bridges the transition from a slow viscous creeping flow characteristic of classical lubrication theory to a Darcy flow which satisfies a potential equation for the pressure field and no slip conditions can not be satisfied. This transition in behavior was also observed by the authors in a recent study of the flow through a circular orifice in a Brinkman medium (Feng & Weinbaum 1999). Although not shown one finds that at large α the bulk motion in the central region is small and it is only near the leading and trailing edges, where the pressure gradient is large, that there is a significant bulk flow.

The key result observed in this section is the large increase in the pressure generated within the fiber matrix as $\alpha(h_2)$ increases. In the microcirculation, this results in a huge repulsive lift force on a moving red cell as it attempts to penetrate the endothelial glycocalyx. This has very important implications for the microcirculation where an 8μm deformable red cell is able to squeeze through 5-6μm capillaries without undergoing constant molecular interaction with the plasmalemma membranes of the endothelial cell at the luminal surface

(Weinbaum & Feng 1999).

5.5 Motion of a Ski or Snowboard

While the motion of red cells inside a microvessel provided the initial motivation for this study, the behavior of the red cell has a striking similarity to the gliding motion of a ski or a snow board on a thin layer of compressed fresh powder. In this section, we propose a two-dimensional fiber matrix model to analyze the mechanics of skiing. Fig. 5.10 is a schematic illustration of a ski or a snow board on a thin layer of fresh powder, which is described by the Brinkman equation. A Cartesian coordinate systems is chosen in which the z axis is in the vertical direction. We consider a rectangular shaped ski or snowboard whose length and width are L and W, respectively. We assume that the thickness of the lubricating layer does not vary in the y direction and is only a function of x. This implies that the permeability parameter α is also independent of y. The sliding velocity is denoted by $U\boldsymbol{i}_x$. The primary difference between the red cell and the ski lies in that there is substantial pressure loss from the leakage at the lateral edges of the skis, which is absent for a red cell if its membrane fills the entire vessel circumference. In the absence of experimental data for the permeability of freshly fallen snow, we use the same fiber matrix model described in section 5.3 for the endothelial surface glycocalyx to estimate the variation of α with h without any further attempt to model the detailed crystal structure of the snow flakes. The purpose of this study is to provide a simple prototype model to obtain some insight into this complicated problem. It is also emphasized that for a ski the assumption that $h/W << 1$ for the compressed powder layer is reasonable for compressed snow depths of at most a few centimeters. The theory in its present form is more applicable in the much wider snowboard.

By introducing the characteristic variables as detailed in section 5.2, one can write the

Reynolds type equation (5.2.23) for the pressure within the powder as

$$\frac{\partial}{\partial x}\left[f+\frac{1}{\alpha^2}\frac{\partial p}{\partial x}(2f-h)\right]+\frac{L^2}{W^2\alpha^2}(2f-h)\frac{\partial^2 p}{\partial y^2}=\frac{\partial h}{\partial x}. \tag{5.5.1}$$

Equation (5.5.1) is a second order elliptic partial differential equation for which we were unable to find an analytic form of solution and developed instead a numerical method based on the pseudo-spectral collocation technique of Orszag (1971).

5.5.1 Numerical Solution of the Reynolds Type Equation

In order to solve the Reynolds equation (5.5.1), we expand the pressure in a double series defined on the domain $D=[0,1]\times[0,1]$ as

$$p(x,y)=\sum_{n=0}^{\infty}\sum_{m=1}^{\infty}p_{nm}T_n(2x-1)\sin(2m-1)\pi y, \tag{5.5.2}$$

in which p_{nm} are unknown coefficients and T_n is a Chebyshev polynomial of order n. Solution (5.5.2) already satisfies the boundary conditions at $y=0$ and $y=1$. When (5.5.2) is substituted into (5.5.1) and the orthogonality of the sine function is employed, one obtains the following set of algebraic equations for p_{nm}

$$\sum_{n=0}^{\infty}p_{nm}\left(\frac{2f-h}{\alpha^2}\left[\frac{d^2}{dx^2}T_n(2x-1)-\frac{L^2}{W^2}T_n(2x-1)\right]+\frac{d}{dx}\frac{2f-h}{\alpha^2}\frac{d}{dx}T_n(2x-1)\right)=$$

$$\left(1-\frac{1}{k}-\frac{\partial f}{\partial x}\right)\frac{4}{(2m-1)\pi},\qquad m=1,2,\cdots. \tag{5.5.3}$$

Using the orthogonality of the Chebyshev polynomial, one can express the derivatives of $T_n(x)$ appearing in (5.5.3) in terms of Chebyshev polynomials. The details of the required formulae can be found in the appendix of Orszag (1971).

We choose the first M equations in (5.5.3) and truncate the infinite summation at its $N+2$ term, where N is sufficiently large to ensure the convergence of the solution. The coefficients p_{nm} are obtained by applying equation (5.5.3) at N collocation points which are

the zeros of $T_N(x)$. These algebraic equations are combined with the boundary condition $p(0) = p(1) = 0$ to solve for the $N + 2$ coefficients for a given m. The numerical scheme is quite stable and convergent as N increases compared with the solution expressed in a double Fourier series.

In our calculations, we use $M = 50$ and $N = 100$. The pressure at the center point of the ski varies within 0.1 percent for $M \geq 100$ and $N \geq 200$. The numerical results for the pressure at $y = 1/2$ when $W/L > 20$ are in excellent agreement with the exact solution presented in the previous section for $W/L \to \infty$.

5.5.2 Results and Discussion

To facilitate comparison with the one-dimensional solution the results for the pressure are presented only at the center line of the ski or snowboard, $y = 1/2$. One of the most important parameters in this application is the choice of the undeformed Darcy permeability for fresh snow powder. Here we assume that the powder is composed of a fibrous matrix whose effective fiber radius a is 0.1mm. However, as noted in Fig. 5.3 the results are not very sensitive to the value of a. For the purpose of illustrating how large a pressure can be built up beneath a ski or snowboard, we will also present the results for various values of $\alpha(h_2)$. The actual value of the fiber spacing at the leading edge in the present model has to be determined by matching the total lift force generated by the compressed powder to the weight of the skier and his/her skis.

The fundamental difference between a red cell gliding on the endothelial glycocalyx and the human skiing on fresh powder is schematically shown in Fig. 5.10. For the human skier or snow boarder there can be a very large loss in the excess pressure due to the escape of the air at the lateral edges of the skis. The magnitude of this loss in excess pressure is largely determined by the parameter L/W in the second term in Eq. 5.5.1. For straight skis a typical of value of L/W is 20, whereas for a snow board this is closer to 4. In either case L^2/W^2 is $>>$ 1. We illustrate the essential physics by presenting results for the pressure

distribution for L/W=10 in Fig. 5.11 for $k = 2$, a moderate compression, for both $\alpha = 0$ (classical lubrication theory) and $\alpha(h_2) = 100$, a value representative of moderately packed snow powder. Also shown for comparison are the results for $L/W = 0$, the case where there is no leakage at the lateral edges, as for the tightly fitting red cell. One observes that the dimensionless excess pressure beneath a planar surface with $L/W = 10$ is two orders of magnitude smaller than for $L/W = 0$. However, for $L/W = 10$ there is a large shift in the maximum pressure towards the rear of a ski or snow board even at this moderate value of k. The pressure builds up gradually over most of the length of the ski and there is a sharp drop in pressure near the trailing edge. This asymmetric pressure distribution would exert a large torque on the skier's ankles and the skier would adjust to a smaller angle of attack.

Fig. 5.12 provides an overall comparison of the changes in lift or repulsive forces as α increases for both a planar surface $L/W = 0$ and $L/W = 10$. The transition for the large increase in lift due to the porous media occurs at α order one. For the red cell the value of α at the leading edge, $\alpha(h_2)$, where the membrane first penetrates the glycocalyx is 160 based on a 0.4μm thickness for the undeformed matrix and an open gap between fibers of 7 nm. This value of α will increase greatly as one proceeds toward the trailing edge of the red cell due to the compression of the matrix. For a human skier the value of α at the leading edge is determined by the requirement that the total lift force must equal the weight of the skier plus his/her skis. The value of α at the leading edge required to achieve this lift will depend on k, the compression ratio, and, as observed in Fig. 5.12, will decrease from about 400 to 100 as k increases from 2 to 5. By digging one's heels into the snow one can achieve the same lift with a small compression at the leading edge and a large compression at the trailing edge. This will also lead to a much larger drag force (not shown).

5.6 Pressure Driven Flow of a Red Cell in a Capillary

The results of the analysis presented in section 5.4 have important implications for the *in vivo* rheology of blood in the microcirculation in which the endothelial glycocalyx plays a

vital role. We are interested, in particular, in the role of the endothelial surface glycocalyx in determining the rheological properties of blood and the popout phenomenon in which the red cell will rise off the endothelial surface and then glide near the edge of the surface matrix layer. Although there is limited experimental data available on the material properties of the glycocalyx, the fiber matrix model based on the Brinkman equation has been applied to several biological transport problems where the model has successfully predicted the measured hydraulic and diffusive permeability coefficients (Weinbaum *et al.* 1992; Weinbaum 1998; Fu *et al.* 1994, 1997, 1998; Hu & Weinbaum 1999). The advantage of the Brinkman equation lies in its simplicity and that one does not need a detailed knowledge of the glycocalyx structure to estimate K_p. We can thus use the model in section 5.3 to represent the fiber deformation. Although this model is based on a flow transverse to a periodic fiber array, these results compare quite well with those for a randomly distributed fiber matrix (Either 1990). We first present a simple geometric model for the pressure driven motion of an idealized red cell which penetrates into the glycocalyx and then examine the effect of this motion on the tube hematocrit and apparent viscosity.

5.6.1 Model and Formulation

There have been numerous previous models for the motion of red cells in microvessels (Lighthill 1968; Fitz-Gerald 1969; Tozeren & Skalak 1978; Secomb *et al.* 1986; Damiano 1998; Secomb *et al.* 1998). Early studies used classical lubrication theory to describe the fluid layer near the capillary wall. The most recent investigations have applied mixture theory to describe a glycocalyx with small deformation and, with the exception of Secomb *et al.* (1998), have assumed that the red cell membranes do not penetrate the glycocalyx. Secomb *et al.* (1986) have shown that axisymmetric lubrication theory yields very accurate results for rigid spheres even for moderate sphere to tube diameter ratios. We thus wish to generalize the analysis in section 5.2 to treat the axisymmetric motion of a rigid pellet in a circular tube which has a deformable matrix lining its walls, as illustrated in Fig. 5.13. The simplified shape assumed for the red cell pellet in Fig. 5.13 is a cylinder with a linearly

varying radius with hemi spherical caps at both its front and rear surfaces. The length of the cell and the size of the caps are determined by requiring the surface area and the volume of the red cell, which in our calculation, are 141.6 μm^2 and 91.5 μm^3, respectively, to remain constant. In this highly idealized model the deformation of the red cell is neglected.

The dimensionless Brinkman equation in cylindrical coordinates is given by

$$\frac{1}{r'}\frac{\partial}{\partial r'}\left(r\frac{\partial u_z'}{\partial r'}\right) = \frac{\partial p'}{\partial z'} + \alpha^2 u_z', \tag{5.6.1}$$

where the dimensionless primed variables are defined by

$$u_z' = \frac{u_z}{U_c}, \qquad r' = \frac{r}{R}, \qquad z' = \frac{z}{R}, \qquad p' = \frac{P}{\mu U_c L/R^2}. \tag{5.6.2}$$

Here R is the vessel radius and U_c is the translational velocity of the red cell. The permeability parameter α is now defined as

$$\alpha = \frac{R}{\sqrt{K_p}}. \tag{5.6.3}$$

For convenience, we now drop the prime on the dimensionless quantities.

The solution to (5.6.1) which satisfies the no slip boundary conditions on the capillary wall and the cell surface closely parallels the derivation in Damiano *et al.* (1996) except that no intervening fluid layer is present between the red cell and the edge of the glycocalyx. The axial velocity is given by

$$u_z = A\left[I_0(\alpha r) - \frac{I_0(\alpha)}{K_(\alpha)}K_0(\alpha r)\right] + \frac{1}{\alpha^2}\left[\frac{K_0(\alpha r)}{K_0(\alpha)} - 1\right]\frac{dp}{dz}, \tag{5.6.4}$$

where

$$A = \frac{1 - \frac{1}{\alpha^2}\left[\frac{K_0(\alpha r_c)}{K_0(\alpha)} - 1\right]\frac{dp}{dz}}{I_0(\alpha r_c) - \frac{I_0(\alpha)}{K_0(\alpha)}K_0(\alpha r_c)}.$$

Here $r_c(z)$ denotes the shape of the red cell and I and K are modified Bessel functions. When

equation (5.6.4) is substituted into the continuity equation and integrated, one obtains

$$Rq_0 = \frac{1}{2}r_c^2 + \int_{r_c}^{R} u_z(r,z)rdr, \tag{5.6.5}$$

where q_0 is the total flux through the cross section normalized by $U_c R^2$. Substituting (5.6.4) into (5.6.5), one obtains the following Reynolds type equation for an arbitrary axisymmetric red cell flowing through a circular tube coated by a layer of fiber matrix:

$$\frac{dp}{dz} = \frac{Rq_0 - \frac{1}{2}r_c^2 + C/D}{B + \frac{1}{\alpha^2}\left[\frac{K_0(\alpha r_c)}{K_0(\alpha)} - 1\right]C/D}. \tag{5.6.6}$$

Here the auxiliary functions B, C and D are given by

$$B = \frac{r_c^2 - 1}{2\alpha^2} + \frac{1}{\alpha^3 K_0(\alpha)}[r_c K_1(\alpha r_c) - RK_1(\alpha)],$$

$$C = \frac{RI_1(\alpha) - r_c I_1(\alpha r_c)}{\alpha} + \frac{I_0(\alpha)}{\alpha K_0(\alpha)}[RK_1(\alpha) - r_c K_1(\alpha r_c)],$$

$$D = I_0(\alpha r_c) - \frac{I_0(\alpha)K_0(\alpha r_c)}{K_0(\alpha)},$$

respectively. Note that in (5.6.6) r_c is an arbitrary function of z and that α is determined by the local compression of the matrix layer. In order to determine the pressure distribution, q_0 has to be prescribed. If the red cell is freely suspended, the total applied force has to vanish. This zero drag condition uniquely determines the motion.

We choose a control volume, bounded by two cross sections at $z = 0$ and $z = L$ in Fig. 5.13 and the corresponding segment of tube wall. Since the freely suspended red cell does not exert a net force, the total force applied on this control volume must be zero for steady flow. In contrast to mixture theory, in which there is a governing equation for the solid phase and the stress is calculated in terms of the summation of forces in both the fluid and the solid phases, special attention must be paid to the Brinkman medium, in which a distributed body force is implicitly included in the governing equation. In fact, when we

integrate the Brinkman equation over any volume ($\mathcal{V}$), the following relation is obtained

$$\int\int_{\partial\mathcal{V}} \mu \frac{\partial \boldsymbol{u}}{\partial n} dS - \int\int\int_{\mathcal{V}} \frac{\mu}{K_p} \boldsymbol{u} dV = \int\int_{\partial\mathcal{V}} p\boldsymbol{n} dS \tag{5.6.7}$$

where $\boldsymbol{n}$ is the normal unit vector of the control volume. Note the second term, which is absent for Stokes flow, represents a body force within the control volume. This force is balanced by the drag force on the fibers.

When equation (5.6.7) and the lubrication approximation are applied, one finds that

$$2\pi \int_0^L \left[\frac{1}{2} \frac{dp}{dz} - \tau_w - \alpha^2 \int_{r_c}^1 u r dr \right] dz = 0, \tag{5.6.8}$$

where τ_w, the shear stress exerted on the tube wall from (5.6.4) is given by

$$\begin{aligned} \tau_w &= \mu \left. \frac{\partial v_z}{\partial r} \right|_{r=R} \\ &= -\frac{K_1(\alpha R)}{\alpha K_0(\alpha R)} \frac{dp}{dz} + A\alpha \left[I_1(\alpha R) + \frac{I_0(\alpha R) K_1(\alpha R)}{K_0(\alpha R)} \right]. \end{aligned} \tag{5.6.9}$$

The Reynolds equation, together with the zero drag condition (5.6.8) are sufficient to solve for the pressure and the total flux q_0.

5.6.2 Results and Discussion

We assume that the glycocalyx can be modeled by the fiber matrix structure described in section 5.3. For comparison with previous studies, we consider a red cell flowing through a 5 μm capillary coated by a 0.5 μm thick glycocalyx as shown in Fig. 5.14. Theoretical predictions for the dimensional pressure distribution along the tube axis for a red cell velocity of 0.1cm/s are shown in the upper portion of Fig. 5.14. The relative penetration of the red cell membrane into the glycocalyx at the trailing edge is given by $\beta = (r_c(0) - r_c(L))/(R - r_c(L))$. This can be written as $\beta = 1 - 1/k$ in terms of the matrix compression ratio k defined previously. The model predicts a large pressure increase over the length of

the cell as a consequence of the penetration. The behavior of the pressure resembles that presented earlier for a gliding plane, except for the large pressure drop that occurs across the cell due to the pressure driven flow. The curves with symbols in Fig. 5.14 are the pressure profiles for $\alpha = 0$, a pure fluid layer without glycocalyx, in which the parameter $\beta = 0$ and 0.9.

Fig. 5.14 shows the elevation in pressure that arises from the penetration. The value of α for the undeformed matrix is approximately 1000 and the pressure differential on the hemispherical caps is the primary contribution to the total driving force. In fact, the zero drag condition applied on the red cell membrane requires that this pressure drop be balanced by the summation of the shear stress and the component of the pressure on the inclined surface in the axial direction. Since there is only a small bulk flow except near the leading and trailing edges where there are steep pressure gradients, one finds (not shown) that the shear stress on the red cell does not vary significantly as the membrane penetrates the glycocalyx, but the pressure contribution grows substantially due to the large increase in drag from the fibers. Physically, the fluid within the matrix has to be expelled by the slanting membrane. Thus, a much greater driving force is needed to achieve the same cell velocity, compared to the non-penetrating case. The high penetration creates a large pressure drop across the cell, an effect which was absent for the gliding motions of a planar surface over a wall in an unbounded medium considered in section 5.4.

The presence of the glycocalyx affects two important rheological quantities: the apparent viscosity ratio, μ_{app}, and the ratio of tube to discharge hematocrit, H_T/H_D. These quantities can be determined from the solution for the driving force $\pi R^2 \Delta P$ over the entire length of the cell and the actual flux through any cross section.

Because the repulsive force generated within the glycocalyx prevents the cell from touching the capillary wall, the red cells will be driven toward the center of the capillary. As a result, the red cell velocity U_c is greater than the average plasma velocity, $\bar{u}$. By applying

mass conservation, one can readily show that

$$\frac{\bar{u}}{U_c} = \frac{2q_0}{U_c} = \frac{H_T}{H_D}. \tag{5.6.10}$$

Figs. 5.15(A), (B) show the pressure drop ΔP across the length of the cell and the tube to discharge hematocrit ratio H_T/H_D for both 5 and 6 μm capillaries lined with a 0.5 μm thick glycocalyx. It is seen that ΔP grows exponentially with respect to the penetration, whereas H_T/H_D approaches unity. The increase of H_T/H_D agrees with one's intuition, since the effective diameter of the capillary is reduced as the cell penetrates the glycocalyx. For a given value of penetration, the 6 μm capillary always exhibits a larger average flux since the leak back through the glycocalyx is smaller than for a 5 μm capillary. However, the pressure drop for a 6 μm capillary is lower than for a 5 μm capillary primarily due to the decreased length of the moving red cell, since cell volume is conserved.

We are particularly interested in examining whether the red cell membrane will penetrate the glycocalyx when the cell moves at velocities ($U_c > 100\mu$m/s). The apparent viscosity ratio of whole blood moving in a capillary is given by (Damiano, 1998) as

$$\mu_{\text{app}} = \frac{1}{8}\left[\frac{R}{L}\frac{dp_0'}{dz'} + \frac{\pi R^3}{V_c}\left(\Delta p' - \frac{\bar{u}}{U_c}\frac{dp_0'}{dz'}\right) H_D\right], \tag{5.6.11}$$

where V_c denotes the cell volume, $\Delta p'$ is the dimensionless presure drop over the cell, and dp_0'/dz' is the dimensionless pressure gradient in the plasma between cells. dp_0'/dz' can be obtained from the solution for a pressure driven flow in a tube coated by a layer of glycocalyx in the absence of red cells. The prime indicates dimensionless variables. The difference between (5.6.11) and the original equation (21) in Damiano (1998) arises from the characteristic length in the axial direction. We have used the total length of the red cell, L, as the characteristic length scale, whereas Damiano used the radius of the capillary instead.

The apparent viscosity ratio calculated using (5.6.11), even when the red cell does not

invade the glycocalyx, $\mu_{\text{app}} \sim 500 H_D$, is one order of magnitude larger than that has been measured *in vivo* (Pries *et al.* 1994). Damiano's calculations using mixture theory predict values for μ_{app} for 5, 6 and 7 μm capillaries which are a factor of 4 lower than the experimental observations in Pries *et al.* (1994). This large difference in the predicted value of μ_{app} between Damiano and the results in Fig. 5.15 is due to two effects. One is the large difference in Darcy resistivity assumed in the two models for the undeformed matrix and the second is that Damiano assumes that a thin plasma layer exists between the red cell membrane and the glycocalyx. In our model, the undeformed matrix has a hydraulic resistivity of $O(10^{11})$ dyn-s/cm^4, corresponding to an open gap between fibers Δ_{2H} of 7 nm. This resistivity is three orders of magnitude greater than that used in Damiano (1998). The values assumed for the Darcy resistivity in Damiano are based on filtration gels with proteoglycans rather than experiments where the capillary selectivity and permeability coefficients are measured *in vivo* as in the present analysis. If we want to match the measured μ_{app}, our calculations indicate that a hydraulic resistivity which is approximately $\sim O(10^{10})$ dyn-s/cm^4 should be used if there is no pure fluid layer above the glycocalyx. If there is a pure fluid layer above the glycocalyx and our predicted resistivity for a fiber spacing of 7 nm is used, we find that measured μ_{app} of 11 for a 5 μm capillary in Pries *et al.* (1994) can be achieved if the thickness of this pure fluid layer is about 0.1 μm. This is about 2.5 percent of the functional diameter of the capillary. However, if Damiano's resistivity is used, one finds that the red cell membrane would need to penetrate 75 percent of the glycocalyx in order to match the measured $\mu_{\text{app}} \approx 11$. If the red cell were to just fill the entire lumen and not invade the glycocalyx, the calculated μ_{app} using Damiano's resistivity is approximately 5.2. This is still only one half the measured value. While the mechanical properties of the glycocalyx are still open to question, the present model for K_p compares much more favorably with the observations in Vink & Duling (1996) where the edge of the FITC-dextran column is approximately 0.2 μm from the edge of the red cell when it is moving with velocities greater than 125 μm/s.

Secomb *et al.* (1998) introduced a variable K_p in their model which allows for a transition

layer at the outer edge of the glycocalyx. However, their results indicate that varying the thickness of this transition layer over the range 0.05-0.4 μm has very little effect on H_T/H_D and the pressure drop ΔP. In the *in vitro* experimental investigation of Adamson & Clough (1992), where cationized ferritin (CF), 10 nm diameter, was used as a marker for the outer edge of the endothelial surface glycocalyx in frog mesentery capillaries, one observes a uniform layer of about 100 nm separating the capillary wall and the CF layer when plasma was present. The electron micrographs of the vessel wall show that the CF layer forms a sharp and distinct interface at the edge of the surface glycocalyx. Since the glycocalyx is negatively charged, CF would have exhibited a diffuse labeling of the outer edge of the matrix if it was less dense a not well defined. These results seem to support the hypothesis that the surface glycocalyx is highly uniform and homogeneous. Similar observations are reported in Vink & Duling's (1996) *in vivo* study using hamster cremaster capillaries where the fluorescent labeling of the glycocalyx by FITC-dextran is also homogeneous.

5.7 Concluding Remarks

Motivated by recent *in vivo* studies in the microcirculation and a rapidly growing recognition of the importance of the endothelial glycocalyx, we have developed a new lubrication theory for highly compressible porous layers based on an effective medium approach. This theory also accounts for order of magnitude variations in the Darcy permeability within the porous layer. The predictions of this theory support Vink & Duling's (1996) *in vivo* experimental observations for both the popout phenomenon and final equilibrium position of the red cell at physiologically observed velocities in 5-7 μm diameter mammalian capillaries. When a 8 μm red cell is first squeezed into a capillary with smaller diameter or when it passes through arterial sphincter, it will elongate and crush the glycocalyx if its velocity is small. As the pressure gradient and thus the red cell velocity increase, the red cell membrane will gradually rise off the vessel wall due to the large repulsive force generated within the glycocalyx. This popout is characterized by an increased clearance between the capillary wall and the red

cell membrane. When the velocity of the red cell achieves values of $U_c > 120\mu$m/s, the cell membrane will first lift off the glycoalyx, creating a thin layer of plasma between the matrix and the red cell whose thickness then increases with U_c. Although the present results are for a rigid planar membrane, the theory can be extended to a deformable red cell membrane using the approach in Secomb *et al.* (1986). Of particular interest is the effect of membrane bending moments on red cell shape at low velocities where there are large compressions of the extracellular matrix. Future work should also include the possible existence of another thin layer of deformable surface glycocalyx coating the red cell membrane, an effect which is not taken into account in the present model.

When the present theory is applied to the motion of a ski or snowboard, a strikingly similar behavior is observed for the pressure distribution and the lift force. By introducing a small tilt angle, a hydrodynamic lift force can be generated which is large enough to sustain a 70 kg human. Several extensions of the basic problem treated in this paper are of interest. In an effort to understand more sophisticated maneuvers in skiing, such as turning and stopping, one must consider the mechanics of edging, where the snow powder is compressed in the transverse direction. The numerical method adopted in section 5.5 is greatly simplified when the lubricating layer does not vary in the transverse direction. This method needs to be generalized to apply to the situation in which h is an arbitrary function of both x and y.

As demonstrated in this paper, large compressions of the fiber matrix lead to dramatic pressure increase in the matrix layer. These huge pressures may give rise to elastic or plastic deformation of the base on which the matrix resides and result in well known elastohydrodynamic complications. Since the Darcy term appearing in the Brinkman equation can also be incorporated in the Navier-Stokes equation to represent an average effect of the porous material (Hornung 1996), it may be worthwhile to investigate the relative importance of viscous dissipation, fluid inertia and matrix deformation in the time-dependent draining of fluid from thin fiber matrix layers, where one has an inertial squeeze film between two closely juxtaposed solid surfaces.

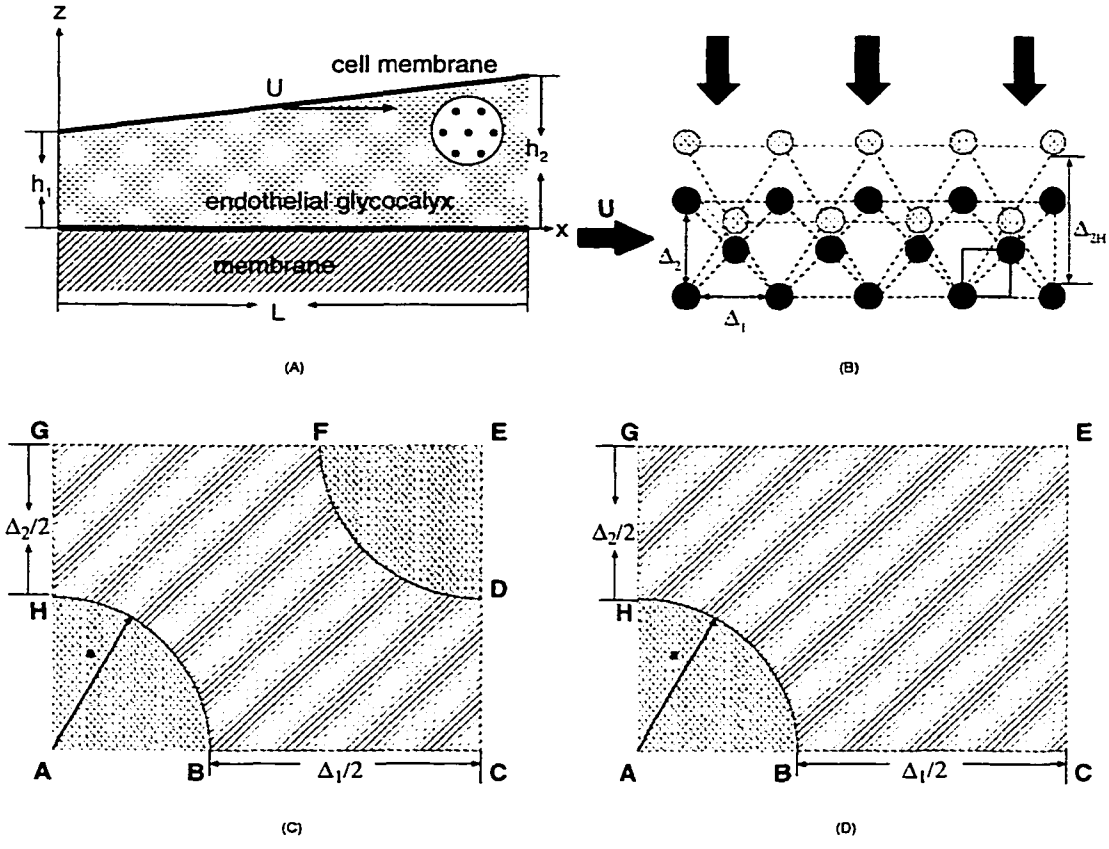

Figure 5.1: (A) Schematic illustration of the present model for sliding motion of a rigid surface over a thin layer of fiber matrix. (B) Inset in (A) shows an idealized model for the fiber matrix which is composed of doubly periodic array of cylindrical fibers of radius a. The undeformed fiber spacings in the lateral and vertical directions are denoted by Δ_1 and Δ_{2H}, respectively. (C) A unit cell for a deformed hexagonal fiber array in which the Stokes equation is solved for the local Darcy permeability. (D) A unit cell showing the deformed rectangular fiber array.

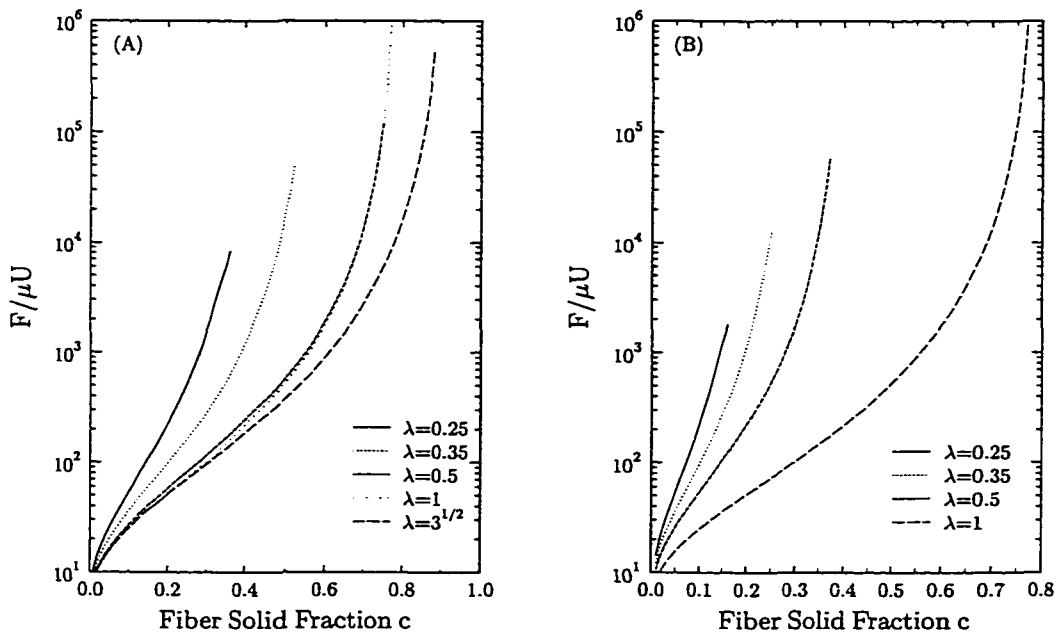

Figure 5.2: The dimensionless drag on a unit length of fiber as a function of fiber solid fraction for different values of $\lambda = (2a + \Delta_2)/(2a + \Delta_1)$. (A) Results for diamond shaped fiber array. (B) Results for rectangular fiber array.

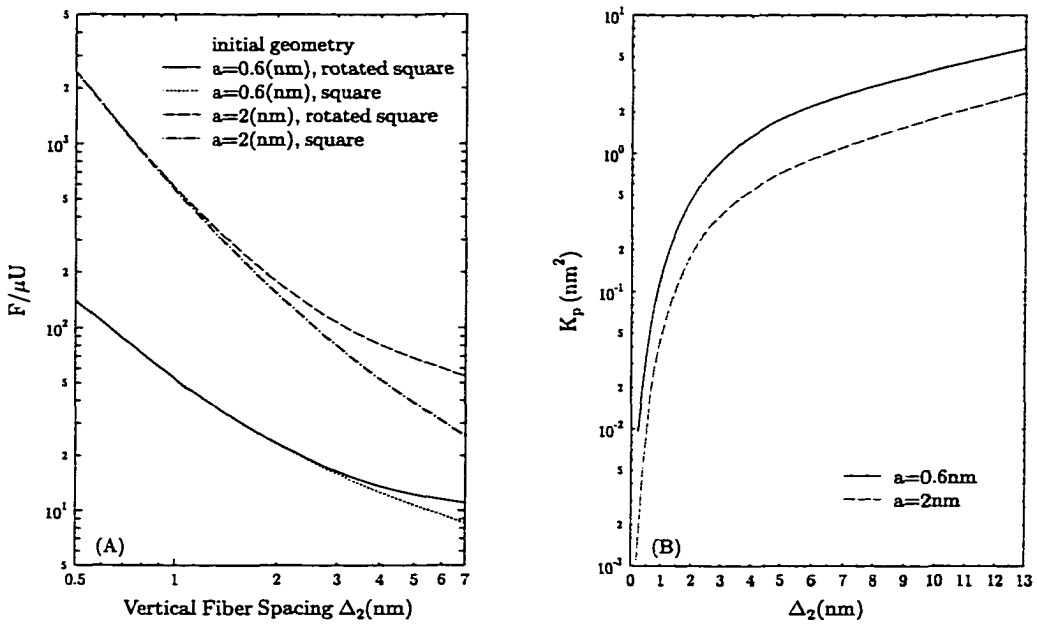

Figure 5.3: (A) Increase in the dimensionless fiber drag per unit length as the fiber matrix is compressed vertically for two different fiber radii, $a = 0.6$nm, GAG side chains in proteoglycans, and $a = 2$nm, the core protein in a proteoglycan. The undeformed square and rotated square ($\pi/4$) fiber spacing $\Delta_1 = \Delta_{2H} = 7$nm. (B) Variation of the Darcy permeability of the fiber matrix for an initially hexagonal fiber arrangement in which $\Delta_1 = 7$nm, $\Delta_{2H} = 13$nm.

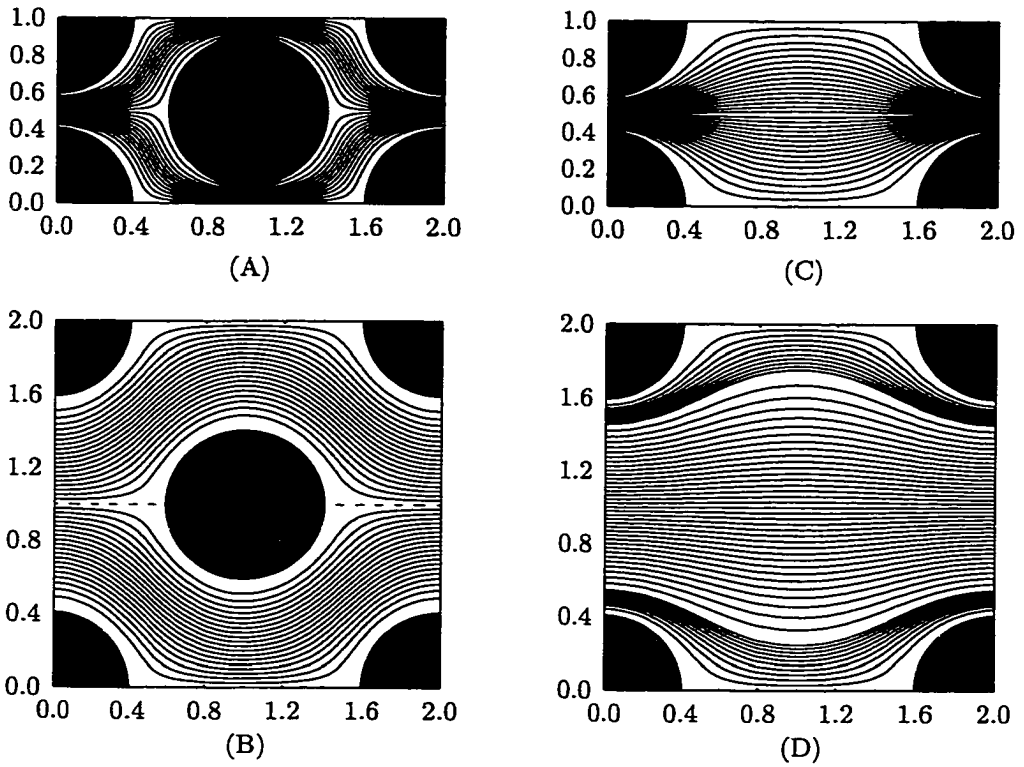

Figure 5.4: Flow patterns within the fiber matrix for both diamond shaped (A, C) and rectangular (B, D) fiber arrays for $\Delta_1/a = 3$, $(2a + \Delta_2)/(2a + \Delta_1) = 1/2$ (A, C) and $(2a + \Delta_2)/(2a + \Delta_1) = 1$ (B, D).

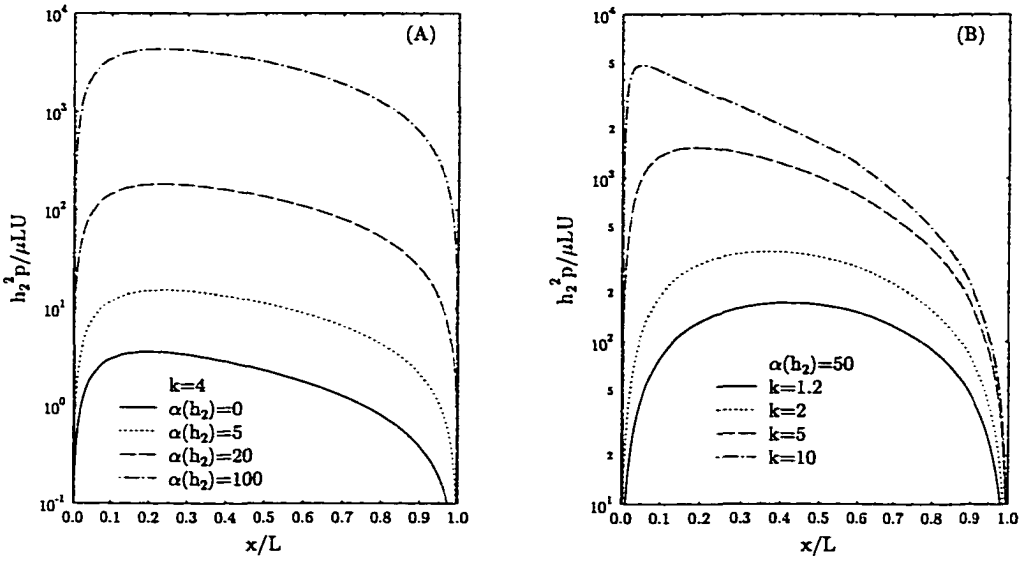

Figure 5.5: Dimensionless pressure distribution in a compressed fiber matrix. (A): Pressure for different values of the undeformed $\alpha(h_2)$ in which the compression ratio $k = 4$. (B): Pressure for various compression ratios k in which $\alpha(h_2) = 50$, a value close to that predicted for a 100nm thick glycocalyx with an initially undeformed hexagonal fiber array in which $\Delta_1 = 7$ nm, $\Delta_{2H} = 13$ nm and $a = 0.6$ nm.

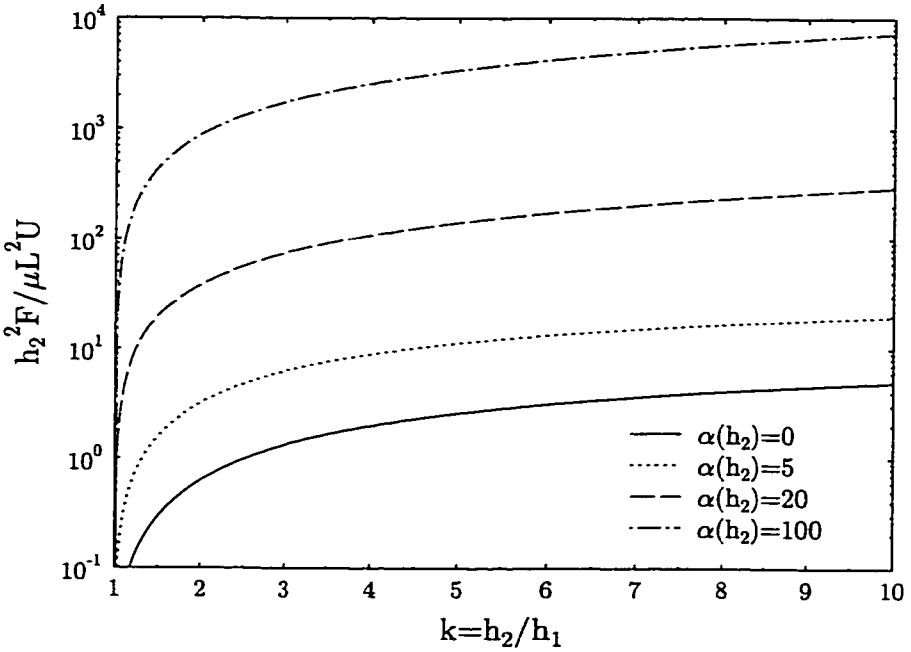

Figure 5.6: The dimensionless lift force on a moving planar boundary as a function of compression ratio k for different values of $\alpha(h_2)$.

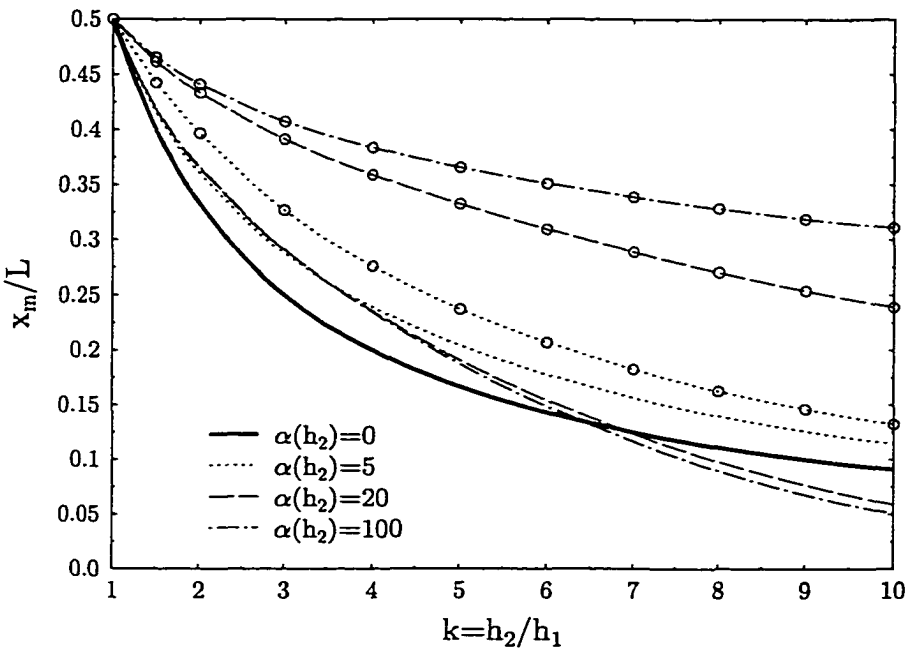

Figure 5.7: Shift of the maximum pressure on the moving surface. For comparison, results for constant α throughout the matrix are shown by circles. The thick solid curve is the result for a pure fluid layer.

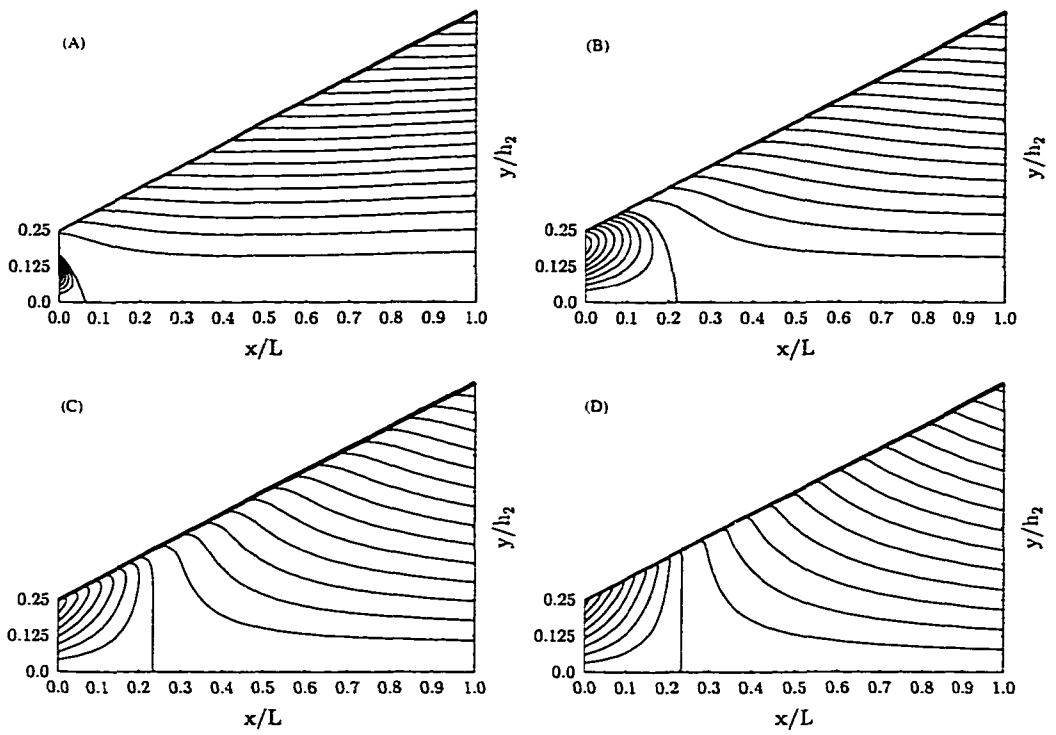

Figure 5.8: Streamline patterns within the fiber matrix for four increasing values of the permeability parameter $\alpha(h_2)$. (A) $\alpha = 0$, classical lubrication theory, (B) $\alpha(h_2) = 5$, (C) $\alpha(h_2) = 20$, (D) $\alpha(h_2) = 100$. The fiber matrix is described by the same parameters as in Fig. 5.5.

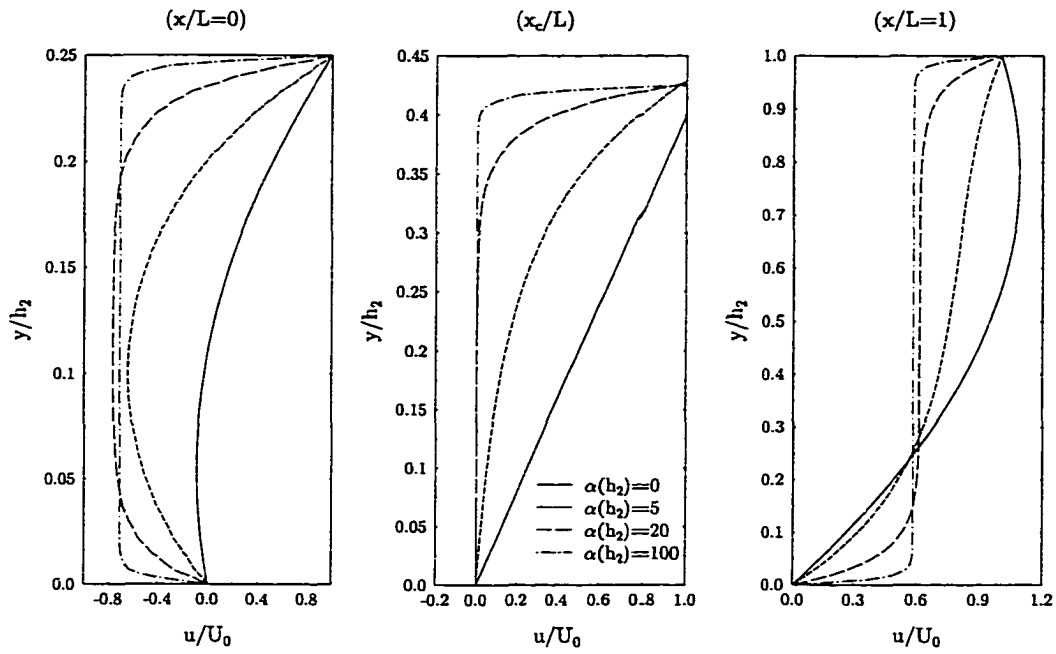

Figure 5.9: Normalized horizontal velocity profiles in fiber matrix for representative $\alpha(h_2)$. Three sets of profiles are shown which correspond to the leading and trailing edges and the position where the pressure reaches its maximum, x_m/L.

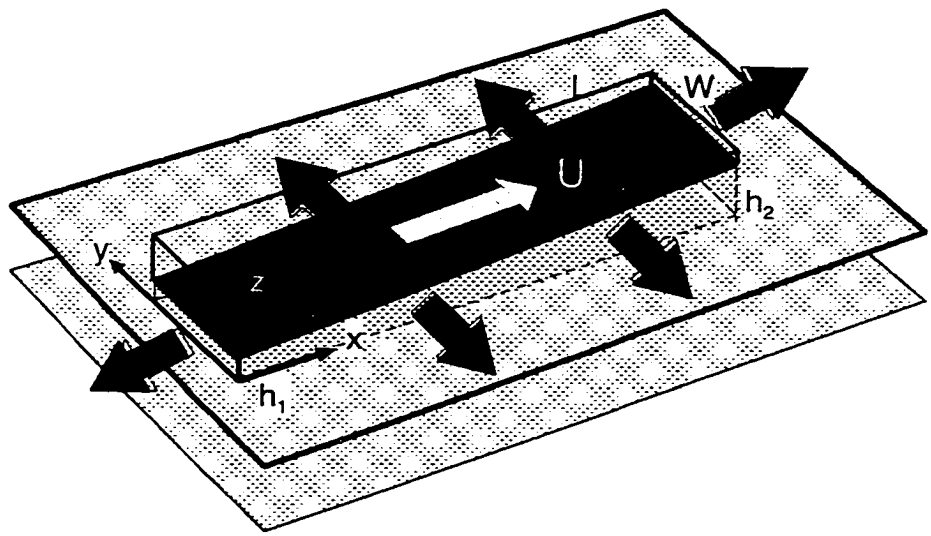

Figure 5.10: Schematic illustration of a snow board or ski compressing a thin layer of fresh powder. Note the escape of air at lateral edges.

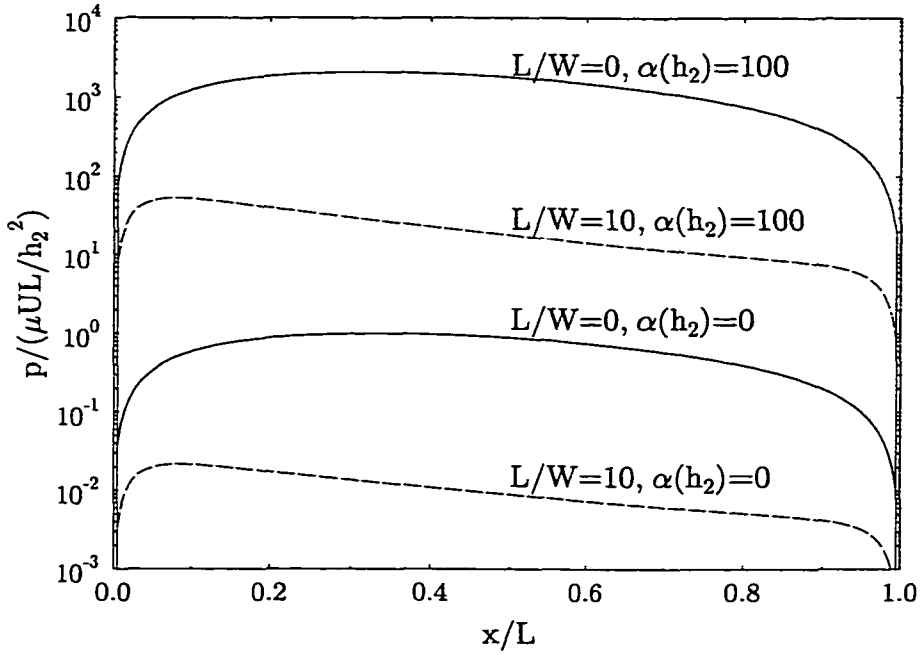

Figure 5.11: Comparison of the pressure distribution on the centerline of a ski or snow board for an intermediate value of $L/W = 10$ and on an infinitely wide surface, $L/W = 0$, with no leakage of air at the lateral edges. In both cases $k = h_2/h_1 = 2$. The thickness of the compressed snow powder at the leading edge is assumed to be 2cm and the value of α at this location, $\alpha(h_2) = 100$, a value typical of moderately packed fresh snow. In the absence of experimental data for the variation of K_p with compression for snow, we have applied the same simple fiber model sketched in Fig. 5.1 for the endothelial glycocalyx.

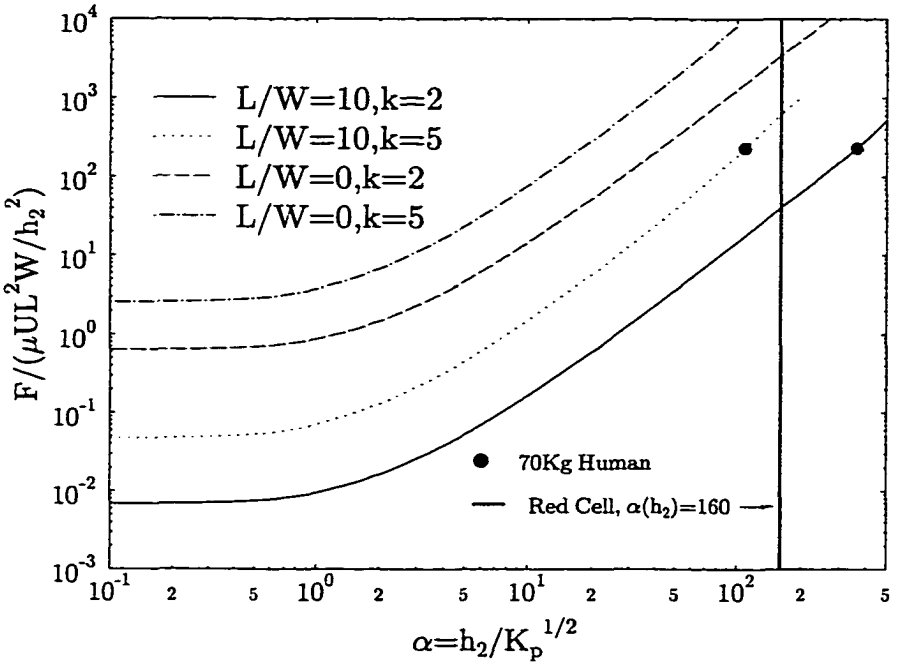

Figure 5.12: Increase in the dimensionless lift force as the value of α at the leading edge, $\alpha(h_2)$, increases. For a red cell, $L/W = 0$, $h_2 = 0.4\mu$m, $\Delta_1 = 7$nm and $\alpha(h_2) = 160$. The properties of the endothelial glycocalyx away from the leading edge are described by the curve for $a = 0.6$nm in Fig. 5.3. For a human skiing on a planar surface with $L/W = 10$, we require that the value of $\alpha(h_2)$ be chosen such that the lift force supports a 70 kg man when $L = 150$cm. The critical value of α depends on the compression ratio, $k = h_2/h_1$, of the surface. If $h_2 = 2$cm, $\alpha(h_2) \sim 400$ for $k = 2$ and $\alpha(h_2) \sim 100$ for $k = 5$.

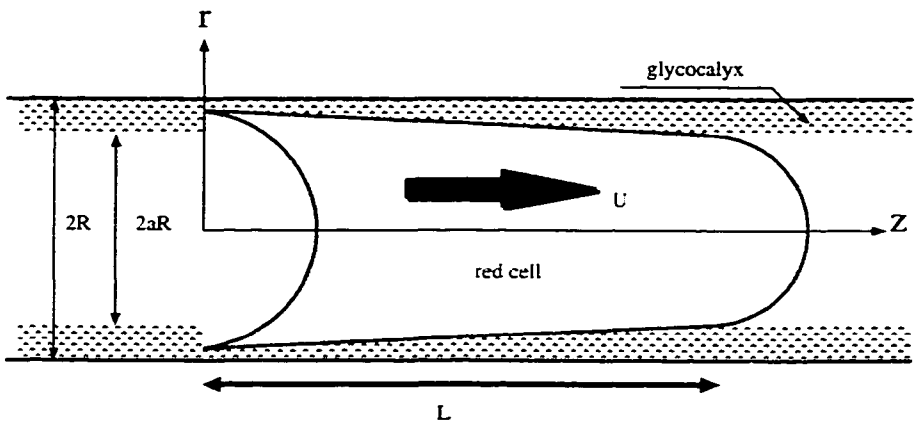

Figure 5.13: Axisymmetric motion of a deformed red cell in a capillary lined with endothelial surface glycocalyx. The model assumes that the red cell penetrates into the surface glycocalyx and two spherical caps are attached to its front and rear to ensure that the surface and volume are unchanged during deformation.

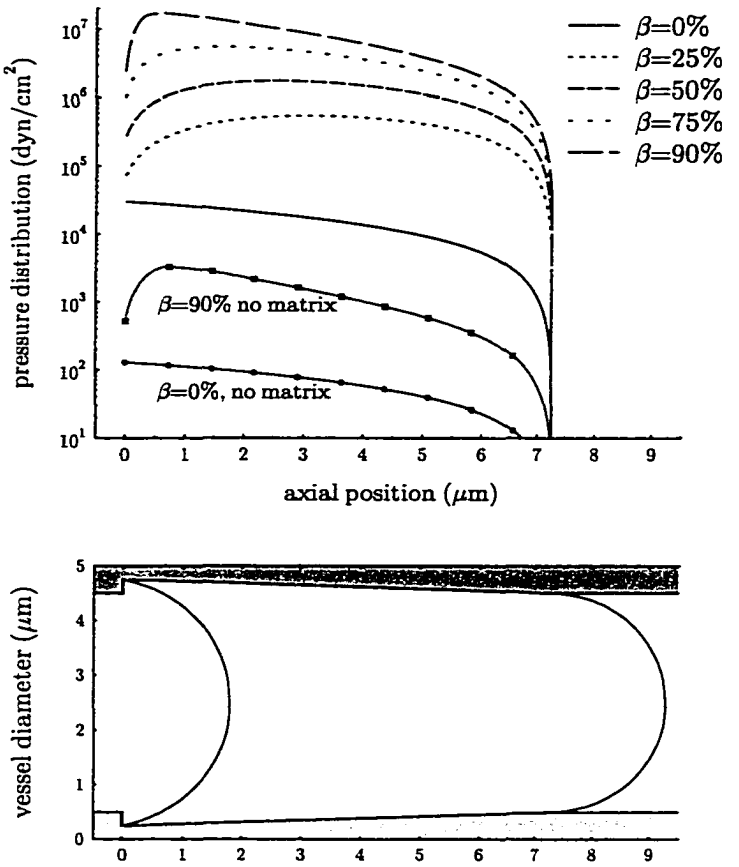

Figure 5.14: Dimensional pressure distribution over the length of a red cell moving at 0.1 cm/s in a 5 μm diameter vessel with a uniform 0.5 μm thick glycocalyx as a function of the penetration parameter $\beta = 1 - 1/k$. The viscosity of the plasma μ is assumed to be 0.01 dyn-s/cm^2. Five curves are presented from no penetration, to high penetration. Note the pressure drop increases by almost three orders of magnitude when the membrane invades 90 percent of the glycocalyx. The maximum pressure shifts to the trailing edge due to the large resistance of the compressed fibers in that region. For comparison, results for a smooth capillary tube ($\alpha = 0$) with $\beta = 0$, 0.9 and $h_2 = 0.5$ μm are shown in lower curves with symbols.

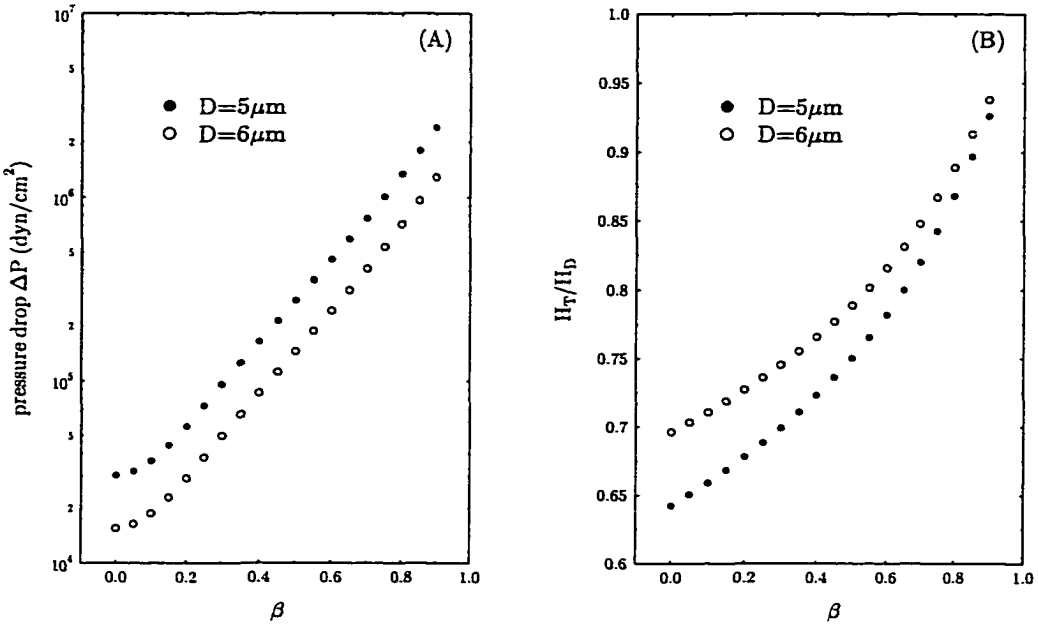

Figure 5.15: (A) Dimensional pressure drop over the cell length as a function of penetration parameter $\beta = 1 - 1/k$ for both 5 and 6 μm capillaries lined with a 0.5 μm thick glycocalyx. (B) The ratio of tube to discharge hematocrit H_T/H_D for same capillary geometry as in (A). Note that for the 6 μm capillary, the effective diameter of the cell is also larger. Both curves approaches unity as the penetration increases.

Chapter 6 Concluding Remarks

In the previous chapters, we have described biological flow problems ranging from problems in molecular mechanics to the motion of cells in the microcirculation. We have also developed a prototype model for skiing or snowboarding. The common thread in these problems is motion in a porous fiber layer that is highly deformable. The fluid or particle motion in this fibrous layer must overcome both the traditional viscous dissipation force and a Darcy resistance accounting for an averaged body force due to the exsistence of the fibers. An effective medium theory, i.e., the Brinkman equation, is used to describe these combined effects.

In chapter 2, solutions of the Brinkman equation for the arbitrary motion of a circular disk are obtained which examine for the first time the effect of particle orientation on the particle drag and torque. Four elementary motions are studied analytically: broadside translation, edgewise translation, rotation about the axis of symmetry and rotation about the diameter. These motions are closely related to the analogous unsteady oscillations of a disk in Stokes flow (Zhang & Stone 1998). However, our solution procedure differs in that the problems are formulated using a general solution of the Brinkman equation and are solved by reducing the dual integral equations arising from the mixed boundary conditions in the plane of the disk to a Fredholm integral equation of the second type. Asymptotic results for the drag and torque are derived for both small and large values of the permeability parameter α defined by $a/\sqrt{K_p}$, where a is the radius of the disk and K_p the Darcy permeability. In contrast to the Stokesian motion of a disk, where the drag differs by only a factor of 1.5 for broadside and edgewise translational motion, and is isotropic for rotation about any axis through its center, there is a large difference in the drag and torque with increasing α. In a Brinkman medium, the drag on the disk is proportional to α for edgewise motion and to α^2 for broadside motion, while the torque is proportional to α^2 for out-of-plane rotation and to α for in-plane rotation. For intermediate values of α, the

integral equations are solved numerically for the drag and torque exerted by the porous medium on the disk. These results are of importance in probing the microstructure of the porous medium and thus provide a way to test the validity of the effective medium approach.

In chapter 3, slow viscous flow through a circular orifice in a plane wall bounded by a fibrous medium is studied also using an effective medium approach. The boundary value problem is again reduced to a set of dual integral equations that satisfy the boundary conditions at the orifice plane and then transformed to a Fredholm integral equation of the second type, which is amenable to numerical solution. Asymptotic analytical results for the total flux through the orifice for a given pressure difference are obtained for both small and large values of the permeability parameter α defined by $a/\sqrt{K_p}$, where a is the orifice radius and K_p the Darcy permeability. For intermediate values of α, the integral equation is solved numerically for the flux and velocity profile at the opening. The present solution exhibits the transition in behavior from Sampson flow ($\alpha = 0$) to the Darcy flow limit as α increases. For $\alpha >> O(1)$, the velocity profile at the opening has a minimum at the orifice center, rises dramatically near the edge of the orifice and then experiences a boundary-layer-like correction of thickness $O(1/\alpha)$ to satisfy the no-slip boundary condition. The close relation between pressure driven flow through a circular orifice and broadside translation of the complementary geometry, namely a circular disk in Stokes flow, is also discussed. The effect of the finite thickness of the orifice is taken account using a simple model proposed by Dagan *et al.* (1982) for Stokes flow through a pore of finite length. The present results are used to estimate the hydraulic conductance of orifice like pores in fenestrated capillaries and fenestral pores in the internal elastic lamina of the arterial intima.

In chapter 4, a general numerical method using the boundary integral equation technique of Pozrikidis (1994) for Stokes flow in an axisymmetric domain is used to obtain the first solutions to the Brinkman equation for the motion of a particle in the presence of planar confining boundaries. The method is first applied to study the perpendicular and parallel motion of a sphere in a fiber-filled medium bounded by either a solid wall or a planar free surface which remains undeformed. By accurately evaluating the singular integrals arising

from the discretization of the resulting integral equation, one can efficiently and accurately treat flow problems with high α defined by $r_s/\sqrt{K_p}$ in which r_s is the radius of the sphere and K_p is the Darcy permeability. Convergence and accuracy of the new technique are tested by comparing results for the drag with the solutions of Kim & Russell (1985a) for the motion of two spheres perpendicular to their line of centers in a Brinkman medium. Numerical results for the drag and torque exerted on the particle moving either perpendicular or parallel to a confining planar boundary are presented for $\epsilon \geq 0.1$, in which ϵr_s is the gap between the particle and the boundary. When the gap width is much smaller than r_s, a local analysis using stretched variables for motion of the sphere indicates that the leading singular term for both the drag and torque is independent of α provided that $\alpha = O(1)$. These results are of interest in modeling the penetration of the endothelial surface glycocalyx by microvilli on rolling leukocytes and the motion of colloidal gold and latex particles when they are attached to membrane receptors and observed in nanovid (video enhanced) microscopy. The method is then applied to investigate the motion of a sphere translating in a channel. The drag and torque exerted on the sphere are obtained for various values of α, the channel height H and particle position b. These numerical results are used to describe the diffusion of a spherical solute molecule in a parallel walled channel filled with a periodic array of cylindrical fibers and to assess the accuracy of a simple multiplicative formula proposed in Weinbaum *et al.* (1992) for diffusion of a solute in the interendothelial cleft.

A new type of lubrication theory that is applicable to highly deformable porous layers is developed in chapter 5 again using an effective medium approach (Brinkman equation). This theory is valid in the limit where the structure is so compressible that the normal forces generated by elastic compression of the fibers comprising the solid phase are negligible compared to the pressure forces generated within the porous layer and the deformation of the solid phase is primarily due to boundary compression as opposed to the motion of the fluid phase. A generalized Reynolds equation is derived in which the spatial variation of the Darcy permeability parameter, $\alpha = H/\sqrt{K_p}$, due to the matrix compression is determined by new local hydrodynamic solutions for the flow through a simplified periodic fiber model

for the deformed matrix. Here H is the undeformed layer thickness and K_p the Darcy permeability. This simplified model assumes that the fibers compress linearly with the deformed gap height in the vertical direction, but the fiber spacing in the horizontal plane remains unchanged. This model is thus able to capture the essential non-linearity that results from large amplitude deformations of the matrix layer.

The new theory shows that there is an unexpected striking similarity between the gliding motion of a red cell moving over the endothelial glycocalyx that lines our microvessels and a human skier or snow boarder skiing on fresh powder. In both cases one observes an order of magnitude compression of the matrix layer when the motion is arrested and predicts values of α that are of order 100. In this large α limit one finds that the pressure and lift forces generated within the compressed matrix are four orders of magnitude greater than classical lubrication theory. In the case of red cell these huge repulsive forces may explain why red cells do not experience constant adhesive molecular interactions with the endothelial plasmalemma, whereas in the case of the skier the theory explains why a 70kg human can glide through fresh powder without sinking to the base as would occur if the motion is arrested. The principle difference between the tightly fitting red cell and the skier is the lateral leakage of the excess pressure at the edges of the skies which greatly diminishes the lift force. A simplified axisymmetric model is presented for the red cell to explain the striking popout phenomena in which a red cell that starts from rest will quickly lift off the surface and then glide near the edge of the glycocalyx and also for the unexpectedly large apparent viscosity measured by Pries *et al.* (1994) *in vivo*.

References

1. Adamson, R. H. & Clough, G. 1992 Plasma proteins modify the biol endothelial cell glycocalyx of frog mesenteric microvessels. *J. Physiol. (Lond.)* **445**, 473.

2. Alon, R., Chen, S., Puri, K. D., Finger, E. B. & Springer, T. A. 1997 The kinetics of L-selectin tethers and the mechanics of selectin-mediated rolling. *J. Cell Biol.* **138**, 1169.

3. Barnard, A. C. L., Lopesz, L. & Hellums, J. D. 1969 Basic theory of blood flow in capillaries. *Microvasc. Res.* **1**, 23.

4. Brady, J. F. 1994 *Hindered diffusion.* In *Extended Abstracts, AICHE Annual Meeting*, San Fransisco, CA p320.

5. Brenner, H. 1961 The slow motion of a sphere through a viscous fluid towards a plane surface. *Chem. Eng. Sci.* **16**, 242.

6. Brinkman, H. C. 1947 A calculation of the viscous force exerted by a flowing fluid in a dense swarm of particles. *Appl. Sci. Res.* A **1**, 27.

7. Bruehl, R. E., Springer, T. A. & Bainton, D. F. 1996 Quantitation of L-selectin distribution on human leukocyte microvilli by immunogold labeling and electron microscopy. *J Histochem. Cytochem.* **44**, 835.

8. Curry, F. E. 1986 Determinants of capillary permeability: a review of mechanisms based on single capillary studies in the frog. *Circ. Res.* **59**, 367.

9. Curry, F. E. & Michel, C. C. 1980 A fiber matrix model of capillary permeability. *Microvasc. Res.* **20**(1),96.

10. Dagan, Z., Weinbaum, S. & Pfeffer, R. 1982 An infinite-series solution for the creeping motion through an orifice of finite length. *J. Fluid Mech.* **115**, 505.

11. Damiano, E. R. 1998 The effect of the endothelial-cell glycocalyx on the motion of red blood cells through capillaries. *Microvascular Res.* **55**, 77.

12. Damiano, E. R., Duling, B. R., Ley, K. & Skalak, T. C. 1996 Axisymmetric pressure-driven flow of rigid pellets through a cylindrical tube lined with a deformable porous wall layer. *J. Fluid Mech.* **314**, 163.

13. Davis, A. M. J. 1991 Slow viscous flow due to motion of an annular disk: pressure driven extrusion through an annular hole in a wall. *J. Fluid Mech.* **231**, 51.

14. Davis, A. M. J. 1993 Some asymmetric Stokes flows that are structurally similar. *Phys. Fluids* A**5**, 2068.

15. Davis, A. M. J. & Ethier, C. R. 1993 Transport through materials bounded by porous surfaces. *Chemical Eng. Sci.*, **48**, 1655.

16. Dembo, M., Torney, D. C., Saxman, K. & Hammer, D. 1988 The reaction-limited kinetics of membrane-to-surface adhesion and detachment. *Proc. R. Soc. Lond.* (B Biol. Sci.) **234**, 55.

17. Durlofsky, L. & Brady, J. F. 1987 Analysis of the Brinkman equation as a model for flow in porous media. *Phys. Fluids* **30**, 3329.

18. Evans, E. & Sackmann, E. 1988 Translational and rotational drag coefficients for a disk moving in a liquid membrane associated with a rigid substrate. *J. Fluid Mech.* **194**, 553.

19. Feng, J., Ganatos, P & Weinbaum, S 1998a The general motion of a circular disk in a Brinkman medium. *Phy. Fluid*, **10**, 2137.

20. Feng, J., Ganatos, P & Weinbaum, S 1998b Motion of a Sphere Near Planar Confining Boundaries in a Brinkman Medium. *J. Fluid Mech.* **375**, 261.

21. Feng, J. & Weinbaum, S. 1999 A model for flow through a planar orifice in a fiber-filled medium with application to fenestral pores in biological tissues. Submitted to the *Chem. Eng. Sci.*

22. Fitz-Gerald, J. M. 1969 Mechanics of red-cell motion through very narrow capillaries. *Proc. R. Soc. Lond.* B **174**, 193.

23. Fu, B. M. Curry, F. E. & Weinbaum, S. 1994 A junction-orifice-entrance layer model for capillary permeability: application to frog mesenteric capillary. *ASME J. Biomech. Eng.* **116**, 502.

24. Ganatos, P., Weinbaum, S., Fischbarg, J. & Leebovich, L. 1980a A hydrodynamic theory for determining the membrane coefficients for the passage of spherical molecules through an intercellular cleft. *Adv. Bioeng., ASME* **3**, 193.

25. Ganatos, P., Pfeffer, R. & Weinbaum, S. 1980b A strong interaction theory for the creeping motion of a sphere between plane parallel boundaries. Part 2. Parallel motion. *J. Fluid Mech.* **99**, 755.

26. Ganatos, P., Weinbaum, S. & Pfeffer, R. 1980c A strong interaction theory for the creeping motion of a sphere between plane parallel boundaries. Part 1. Perpendicular motion. *J. Fluid Mech.* **99**, 739.

27. Ganatos, P., Weinbaum, S. & Pfeffer, R. 1982 Gravitational and zero-drag of a sphere of arbitrary size in an inclined channel at low Reynolds number. *J. Fluid Mech.* **124**, 27.

28. Gluckman, M. J. Pfeffer, R. & Weinbaum, S. 1971 A new technique for treating multi-particle slow viscous flow: axisymmetric flow past spheres and spheroids. *J. Fluid Mech.* **50**, 705.

29. Goldman, A. J., Cox, R. G. & Brenner, H. 1966 The slow motion of two identical arbitrarily oriented spheres through a viscous fluid. *Chem. Eng. Sci.* **21**, 1151.

30. Happel,J. & Brenner, H. 1983 *Low Reynolds Number Hydrodynamics*, Noordhoff.

31. Hart, T. K. & Pino, R. M. 1985 Variations in capillary permeability from apex and crypt in the villus of the ileo-jejunum. *Cell Tissue Res.* **241**(2), 305.

32. Hasimoto, H. 1958 On the flow of a viscous fluid past a thin screen at small Reynolds numbers. *J. Phy. Soc. Japan.* **13**, 633.

33. Hornung, H. 1996 *Homogenization and Porous Media*, Springer-Verlag.

34. Howells, I. D. 1974 Drag due to the motion of a Newtonian fluid through a sparse random array of small fixed rigid objects. *J. Fluid Mech.* **64**, 449.

35. Hou, J. S., Mow, V. C., Lai, W. M. & Holmes, M. H. 1991 An analysis of the squeeze-film lubrication mechanism for articular cartilage. *J Biomech.* **25**, 247.

36. Howells, I. D. 1998 Drag on fixed beds of fibers in slow flow. *J. Fluid Mech.* **355**, 163.

37. Hsu, R. & Ganatos, P. 1989 The motion of a rigid body in viscous fluid bounded by a plane wall. *J. Fluid Mech.* **207**, 29.

38. Hu, X. & Weinbaum, S. 1999 A new view of Starling's hypothesis at the microstructural level. *Microvascular Res.* In press.

39. Hughes, B. D., Pailthorpe, B. A. & White, L. R. 1981 The translational and rotational drag on a cylinder moving in a membrane. *J. Fluid Mech.* **110**, 349.

40. Huang, Y., Rumschitzki, D., Chien, S. & Weinbaum, S. 1994 A fiber matrix model for the growth of macromolecular leakage spots in the arterial intima. *J. Biomed. Eng.* **116**, 430.

41. Huang, Y., Rumschitzki, D., Chien, S. & Weinbaum, S. 1997 A fiber matrix model for the filtration through fenestral pores in a compressible arterial intima. *Am. J. Physiol.272 (Heart Circ. Physiol. 41)*, H2023.

42. Huang, Y., Jan, K. M., Rumschitzki, D. & Weinbaum, S. 1998 Structure changes in rat aortic intima due to transmural pressure. *J. Biomed. Eng.* **120**, 476.

43. Jackson, G. W. & James, D. F. 1986 The permeability of fibrous porous media. *Can. J. Chem. Eng.* **64**, 364.

44. Jeffrey, D. J. 1982 Low-Reynolds-number flow between converging spheres. *Mathematika* **29**, 58.

45. Johnson, E. M.,Berk, D. A., Jain, R. K. & Deen, W. M. 1996 Hindered diffusion in agarose gels: test of effective medium model. *Biophysics J.* **70**, 1017.

46. Kenyon, D. E. 1979 A mathematical model of water flux through aortic tissue. *Bull. Math. Biol.* **41**, 79.

47. Kim, S. & Karrila, S. J. 1991 *Microhydrodynamics: Principles and Selected Applications.* Butterworth-Heinemann.

48. Kim, S. & Russel W. B. 1985a The hydrodynamic interactions between two spheres in a Brinkman medium. *J. Fluid Mech.* **154**, 253.

49. Kim, S. & Russel W. B. 1985b Modeling of the porous media by renormalization of the Stokes equations. *J. Fluid Mech.* **154**, 269.

50. Kosar, T. F. & Phillips, R. J. 1995 Measurement of Protein Diffusion in Dextrans Solutions by Holographic Interferometry. *AIChE J.* **41**, 701.

51. Lai, W. M. & Mow, V. C. 1980 Drag-induced compression of articular cartilage during a permeation experiment. *Biorheology* **17**, 111.

52. Lawrence, C. J. & Weinbaum, S. 1986 The force on an axisymmetric body in linearized, time-dependent motion: a new memory term. *J. Fluid Mech.* **171**, 209.

53. Lawrence, C. J. & Weinbaum, S. 1988 The unsteady force on a body at low Reynolds number; the axisymmetric motion of a spheroid, *J. Fluid Mech.* **189**, 463.

54. Lee, G. M., Zhang, F., Ishihara, A, McNeil, C. L. & Jacobson, K. A. 1993 Unconfined lateral diffusion and and estimate of pericellular matrix viscosity revealed by measuring the mobility of gold-tagged lipids. *J. Cell Biol.* **120**, 25.

55. Leighton, D. & Acrivos, A. 1987 The shear-induced migration of particles in concentrated suspensions. *J. Fluid Mech.* **181**, 415.

56. Levick, Y. J. R. 1987 Flow through interstitium and other fiber matrices. *Quart. J. Experimental Physio.* **72**, 409.

57. Levick, Y. J. R. &d Smaje, L. H. 1987 An analysis of permeability of a fenestra. *Microvascular Res.* **33**, 233.

58. Levitt, D. J. 1975 General continuum analysis of transport through pores I. proof of Onsager's reciprocity postulate for uniform pore. *Biophys. J.* **15**, 533.

59. Lighthill, M. J. 1968 Pressure-forcing of tightly fitting pellets along fluid-filled tubes. *J. Fluid Mech.* **34**, 113.

60. Loewenberg, M. 1994 Axisymmetric unsteady Stokes flow past an oscillating finite-length cylinder. *J. Fluid Mech.* **265**, 265.

61. Luft, J. H. 1965 Fine structure of capillary and endocapillary layer as revealed by ruthenium red. *Proc. Fed. Amer. Soc. Exp. Biol.* **25**, 1773.

62. Lundgren, T. S. 1972 Slow flow through stationary random beds and suspensions of spheres. *J. Fluid Mech.* **51**, 273.

63. Michel, C. C. 1997 Starling: the formation of his hypothesis of microvascular fluid exchange and its significance after 100 years. *Exp. Physiol.* **82**, 1.

64. Mokady, A. J., Mestel, A. J. & Winlove, C. P. 1997 Flow through the glycocalyx. *J. Fluid Mech.* **383**, 353.

65. Muldowney, G. P. & Higdon, J. J. L. 1995 A spectral boundary element approach to three-dimensional Stokes flow. *J. Fluid Mech.* **298**, 167.

66. M. E. O'Neill & K. Stewartson 1967 On the slow motion of a sphere parallel to a nearby wall. *J. Fluid Mech.* **27**, 705.

67. Orszag, S. A. 1971 Accurate solution of the Orr-Sommerfeld stability equation. *J. Fluid Mech.* **50**, 689.

68. Phillips, R. J., Deen, W. M. & Brady, J. F. 1989 Hindered Transport of Spherical Macromolecules in Fibrous Membranes and Gels. *AIChE J.* **35**, 1761.

69. Phillips, R. J., Deen, W. M. & Brady, J. F. 1990 Hindered transport in fibrous membranes and gels: effect of solute size and fiber configuration. *J. Colloid Interface Sci.* **139**, 163.

70. Pozrikidis, C. 1988 A study of linearized oscillatory flow past particles by the boundary-integral method. *J. Fluid Mech.* **202**, 17.

71. Pozrikidis, C. 1992 *Boundary Integral and Singularity Method for Linearized Viscous Flow.* Cambridge University Press, Cambridge.

72. Pozrikidis, C. 1994 The motion of particles in the Hele-Shaw cell. *J. Fluid Mech.* **261**, 199.

73. Pries, A. R., Neuhaus, D. & Gaehtgens, P. 1992 Blood viscosity in tube flow: Dependence on diameter. *Am. J. Physiol.* **263**, H1770.

74. Pries, A. R., Secomb, T. W., Gessner, T., Sperandio, M. B., Gross, J. F. & Gaehtgens, P. 1994 Resistance to blood flow in microvessels in vivo. *Circ. Res.* **75**, 904.

75. Saffman, P. G. 1976 Brownian motion in thin sheet of viscous fluid. *J. Fluid Mech.* **73**, 593.

76. Saffman, P. G. & Delbruck, M. 1975 Brownian motion in biological membranes. *Nat. Acad. Sci.*, **72**, 3111.

77. Sako, Y. & Kusumi, A. 1994 Compartmentalized structure of the plasma membrane for receptor movements as revealed by a nanometer-level motion analysis. *J. Cell Biol.* **125**, 1251.

78. Sako, Y. & Kusumi, A. 1995 Barriers for lateral diffusion of transferrin receptors in the plasma membranes as characterized by receptor dragging by laser tweezers: fence versus tether. *J. Cell Biol.* **129**, 1559.

79. Sako, Y., Nagafuchi, A., Tsukita, S., Takeichi, M. & Kusumi, A. 1998 Cytoplasmic regulation of the movement of E-cadherin on the free cell surface as studied by optical tweezers and single particle tracking: corraling and techering by the membrane skeleton. *J. Cell Bio.* **140**, 1227.

80. Sangani, A. S. & Acrivos, A. 1982 Slow flow past periodic arrays of cylinders with application to heat transfer. *Int. J. Multiphase Flow* **8**. 193.

81. Schmid-Schoenbein, H. 1999 Self organized blood flow observed by in *in vivo* rheoscopy: High resolution flow visulization of red blood cells traveling from the arterioles to the vessels in living microvascular beds. *Plenary Lecture Euromech. Colloquium* 389, Gray, Austria, April 20-24.

82. Schlichting, H. 1979 *Boundary Layer Theory*, 6th Edition, McGraw-Hill.

83. Schulze, C. & Firth, J. A. 1992 The interendothelial junction in myocardiol capillaries: Evidence for the existence of regularly spaced, cleft spanning structures. *J. Cell Sci.* **101** 647.

84. Secomb, T. W. & Gross, J. F. 1983 Flow of red blood cells in narrow capillaries: role of membrane tension. *Int. J. Microcir. Clin. Exp.* **2**, 229.

85. Secomb, T. W., Skalak, R., Ozkaya, N. & Gross, J. F. 1986 Flow of axisymmetric red cell in narrow capillaries. *J. Fluid Mech.* **163**, 405-423.

86. Secomb, T. W., Hsu, R. & Pries, A. R. 1998 A model for red blood cell motion in glycocalyx-lined capillaries. *Am. J. Physiol.* **274** (Heart Circ. Physiol. 43: H1016).

87. Sneddon, I. N. *Mixed Boundary Value Problems in Potential Theory.* (John Wiley and Sons Inc. 1968).

88. Solomentsev, Y. E. & Anderson, J. L. 1996 Rotation of a sphere in Brinkman fluids. *Phys. Fluid* **8**, 1119.

89. J. A. Stratton, 1941 *Electromagnetic Theory*, McGraw-Hill.

90. Stone, H. A. & Ajdari, A. 1998 Hydrodynamics of particles embedded in a flat surfactant layer overlying a subphase of finite depth. *J. Fluid Mech.* **369**, 151.

91. Tam, C. K. W. 1969 The drag on a cloud of spherical particles in low Reynolds number flow. *J. Fluid Mech.* **38**, 537.

92. Tanzosh, J. P. & Stone, H. A. 1996 A general approach for analyzing the arbitrary motion of a circular disk in a Stokes flow. *Chem. Eng. Comm.* **148**, 333.

93. Tozeren, H. & Skalak, R. 1978 The steady flow of closely fitting incompressible elastic spheres in a tube. *J. Fluid Mech.* **87**, 1.

94. Tranter, C. J. 1951 On some dual integral equations.*Quart. J. Math.* **2**, 60.

95. Tsay, R. & Weinbaum, S. 1991 Viscous flow in a channel with periodic cross-bridging fibers: exact solutions and Brinkman approximation. *J. Fluid Mech.* **226**, 125.

96. Vink, H. & Duling, B. R. 1996 Identification of distinct luminal domains for macromolecules, erythrocytes and leukocytes within mammalian capillaries. *Circ. Res.* **71**, 581.

97. Wang, W. & Parker, K. H. 1995 The effect of deformable porous surface layers on the motion of a sphere in a narrow cylindrical tube. *J. Fluid Mech.* **283**, 287.

98. Wang, H. & Skalak, R. 1969 Viscous flow in a cylindrical tube containing a line of spherical particles. *J. Fluid Mech.* **38**, 75.

99. Wang, D. M. & Tarbell, J. M. 1995 Modeling interstitial flow in an artery wall allows estimation of wall shear stress on smooth muscle cells. *J. Biomech. Eng.* **117**, 358.

100. Weinbaum, S. 1998 Models to solve mysteries in biomechanics at the cellular level; a new view of fiber matrix layers. *Annals of Biomed. Eng.* **26**, 1.

101. Weinbaum, S., Ganatos, P. & Yan, Z. Y. 1990 Numerical multipole and boundary integral equation techniques in Stokes flow. *Annu. Rev. Fluid Mech.* **22**, 275.

102. Weinbaum, S., Tsay, R. & Curry, R. E. 1992 A three-dimensional junction-pore-matrix model for capillary permeability. *Microvascular Research* **44**, 85.

103. Williams, W. E. 1968 *Q. J. Mech. Appl. Math.* **21**, 133.

104. Yin, Y. *et al.* 1997 A model for the initiation and growth of extracellular lipid liposomes in arterial intima. *Am. J. Physiol.* **272** (Heart Circ. Physiol. 41: H1033)

105. Youngren, G. K. & Acrivos, A 1975 Stokes flow past a particle of arbitrary shape: a numerical method of solution. *J. Fluid Mech.* **69**, 377.

106. Zeng, Y. & Weinbaum, S. 1994 Stokes flow through periodic orifices in a channel. *J. Fluid Mech.* **263**, 207.

107. Zhang, F., Crise, B., Su, B., Hou, Y., Rose, J., Bothwell, A. & Jacobson, K. 1991 Lateral diffusion of membrane-spanning and glycosylphospha tidylinositol linked proteins: toward establishing rules governing the lateral mobility of membrane proteins. *J. Cell Biol.* **115**, 75.

108. Zhang, W. & Stone, H. A. 1998 Oscillatory motions of circular disks and near spheres in viscous flows. *J. Fluid Mech.* **367**, 329.